University of Alberta

MEMS-compatible Integrated Hollow Waveguides Fabricated by Buckling Self-assembly

by

Eric Richard Epp

A thesis submitted to the Faculty of Graduate Studies and Research
in partial fulfillment of the requirements for the degree of

Master of Science

in

Photonics and Plasmas

Electrical and Computer Engineering

Fall 2010
Edmonton, Alberta

Examining Committee

Dr. Ray DeCorby, Electrical and Computer Engineering

Dr. James McMullin, Electrical and Computer Engineering

Dr. Vien Van, Electrical and Computer Engineering

Dr. Al Meldrum, Physics

Everyone is interesting you just have to ask the right questions.

Travelling Companion

Vietnam

For Auntie Linda,

Your embrace of life will always be inspiring.

Abstract

This thesis describes the fabrication and characterization of integrated hollow Bragg waveguides fabricated by controlled thin film buckling. Hollow waveguides based on two different set of materials were studied. In the first case, thermal tuning of air-core dimensions was studied using waveguides, with chalcogenide glass and polymer claddings. Results showed that the change in air-core height as a function of small temperature variations was in good agreement with theory.

Planar, silicon based, hollow core waveguides with Si/SiO_2 Bragg reflector claddings are also described. Fabrication was accomplished by incorporating compressive stress in the sputtered Si and SiO_2 layers and then heating samples to induce buckling along predefined areas of low adhesion. Several low adhesion layers were studied, but a fluorocarbon layer was deposited by CVD gave the best results. Optical experiments demonstrated optical confinement in the air-core, with loss in the ~5 dB/cm range at the 1550 nm wavelength.

Acknowledgements

Finally, upon completion of this thesis I reminisce and become humbled by how many people have supported me through the process.

Thanks to Dr. DeCorby for his guidance and understanding throughout my degree. Your help preparing, and drafting this thesis has been invaluable.

Thanks to Nakeeran Ponnampalam for never declining the many requests for assistance.

Thanks to Florian Lenz and Trevor Allen for insight and training around the lab.

Thanks to Dr Meldrum and Dr. McMullin for the support, and providing thoughtful insight for the lab.

Thanks to the physics department, and specifically Don Mullin for his always prompt and enthusiastic assistance in the Condensed Matter Lab.

Thanks to the NanoFab staff for training me on numerous processes and equipment, and helping me out when I was in a jam.

Thanks to the summer students Ward Newmann, Brian Drobot and Shalon McFarlane for the excellent data you collected and making the lab seem less empty.

This degree was made possible by the funding provided by TRLabs and other agencies such as NSERC, and the University of Alberta.

And finally thank you to my family Victor, Judy and Gillian for giving me the freedom and support to do anything that I had a passion for. Your encouragement is what allowed me to finish.

Table of Contents

LIST OF TABLES

List of Figures

List of Symbols

θ	Angle
s	Second
dB	Decibels
ARROW	Anti-Resonant Reflecting Optical Waveguide
PECVD	Plasma Enhanced Chemical Vapor Deposition
LPCVD	Liquid Phase Chemical Vapor Deposition
M	Mode order
d_c	Core thickness
n	Index of refraction
λ	Wavelength
t_j	ARROW layer thickness
Si	Silicon
a-Si	Amorphous silicon
SiO_2	Silicon dioxide
SEM	Scanning electron microscope
PVD	Physical vapor deposition
rf	Radio frequency
DC	Direct current
Y	Young’s modulus
M	Moment
F	Force

σ	Stress
ν	Poissons ratio
b	Half buckle width
$\mathbf{E}$	Electric field
$\mathbf{k}$	Wave vector
ω_n	Discrete mode frequencies
a	Crystal spacing
c	Speed of light
PAI	Polyimide-imide
IG2	Chalcogenide glass
S_T	Taper slope
FWHM	Full Width Half Max
NA	Numerical Aperture
T	Temperature
κ	Extinction coefficient
sccm	Standard cubic centimeters

Chapter 1 Background and Motivation

1.1 Background

Recently there has been increasing use of photonics in the microelectronics, MEMS, and lab-on-chip industries. MEMS that incorporate photonics or optics are often referred to as micro-optical electrical mechanical systems (MOEMS). Furthermore, systems that incorporate both microfluidics and optical technology have recently spawned a new field of research termed optofluidics. This thesis is concerned with the study of integrated hollow (air-core) optical waveguides, which can in principle act as both a light conduit and a microfluidic channel giving them significant potential for applications in LOC analysis systems. Furthermore, air-core waveguides can be readily tuned using MEMS-based activation techniques such as electrostatic or electro-thermal effects.

The thesis builds on previous work in the DeCorby lab which led to the development of a new buckling self-assembly process for the fabrication of hollow Bragg waveguides. The goal of the present study was to establish and extend the MEMS-compatibility of these waveguides. This included a study on thermal tuning of the first generation waveguides, which were fabricated using a chalcogenide glass and a high performance polymer. Subsequently, the work was focused on the development of a second-generation hollow waveguide by a similar buckling self-assembly approach but using MEMS-compatible silicon-based materials.

1.2 Applications of Integrated Hollow Waveguides

Tests such as DNA sequencing, immuno and nucleic acid assays, along with on-site environmental, forensics and biohazard detection are all areas that can benefit from compact and reliable sensing devices. Currently, the majority of tests and their associated biochemical protocols often require days or weeks to perform and can reach hundreds of dollars per test [1]. Furthermore platforms for the tests are typically bulky, require large stores of reagents, and consume large amounts of power. Moreover, due to their complexity, tests often need to be repeated several times in order to achieve the required level of reliability. These factors demonstrate the need for developing low cost, highly automated platforms. Incorporating integrated hollow waveguides into functional sensing device is the ultimate goal of the research described here.

1.2.1 Optofluidic Waveguides

Optofluidics is a relatively new field, and has evolved significantly over the last decade [2]. A large body of micro- and nanofluidics research has allowed the miniaturization of fluidic control devices, such as valves and pumps, making possible the realization of complex microfluidic systems [3],[4]. Related to this, the last few years have seen the development of some of the first ‘optofluidics devices’ [5]. Most of these devices fall into two distinct categories: devices to analyze fluids by means of some type of optical detection system, or those that use fluids as a means of altering the state of an optical device. Applications of optofluidics are expected in many fields, including analytical chemistry,

biotechnology, chemical synthesis and environmental monitoring [2],[6]. Biosensing is an especially promising field for the application of optofluidics technologies, due to the potential to dramatically shrink devices that are currently in use. Optical elements can be incorporated into microfluidic devices, resulting in a portable device with increased sensitivity. The small fluid volumes in an optofluidic waveguide are even suitable for single molecule detection [7]. Fig. 1.1 shows an example of a device that utilizes multiple micromechanical valves and pumps, and which was designed to investigate E. coli bacteria [8].

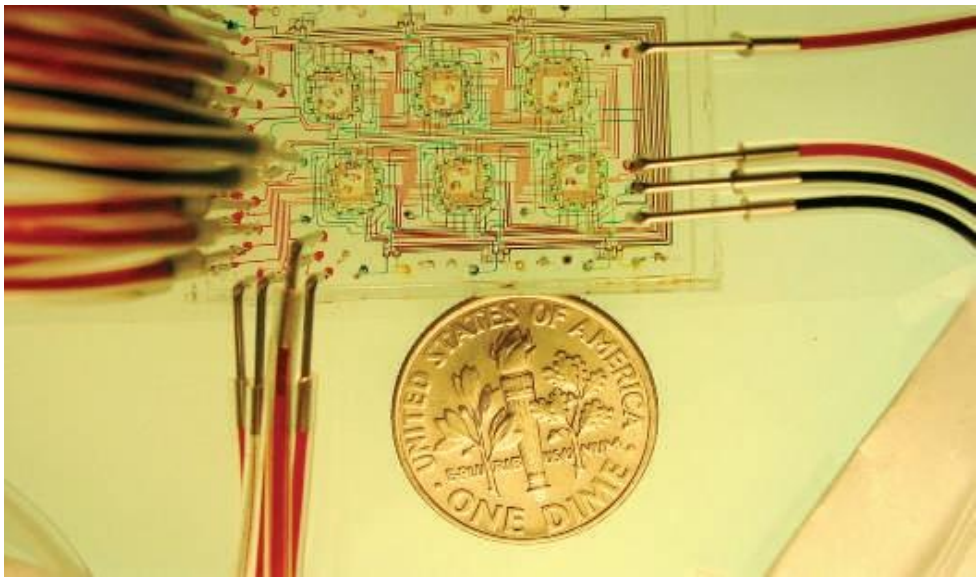

Figure 1.1 - A microfluidic chemostat that incorporates complicated flow dynamics and pneumatic valves to operate six devices in parallel, adapted from [8].

1.3 Alternative Types of Hollow Waveguides

1.3.1 Total Internal Reflection Waveguides

The most common waveguide in use today is the optical fibre, which uses index guiding to confine light to a high index core clad by a lower index material, (Fig.

1.3).The operation of the waveguides is governed by Total internal reflection and can be understood using the theory of ray optics.

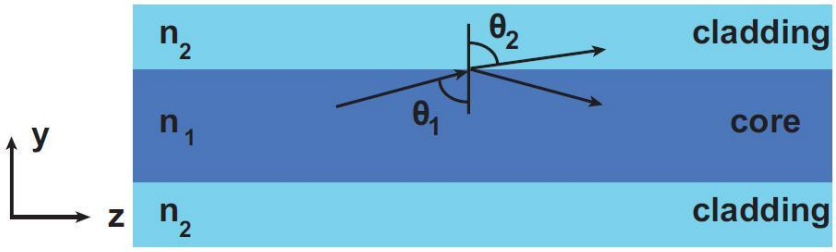

Figure 1.2 - Propagation of a light ray in an index guiding waveguide, adapted from [9].

As a light ray propagates in the +z direction along the core of the waveguide it will strike the cladding interface. The relationship between the angles of the reflected and transmitted rays is described by Snell's law of refraction:

$$n_1 \sin\theta_1 = n_2 \sin\theta_2, \qquad 1.1$$

where θ_1 and θ_2 are the angles and n_1 and n_2 are the refractive index of the core and cladding, respectively. Complete reflection of the ray is known as total internal reflection (TIR) and occurs when the incident angle θ_1 exceeds a value called the critical angle, θ_c, given by:

$$\theta_1 > \sin^{-1}\left(\frac{n_2}{n_1}\right) = \theta_c. \qquad 1.2$$

An incidence angle higher then θ_c results in sin θ_2 becoming imaginary. One of the limitations of using total internal reflection to guide light is the requirement that $n_1 > n_2$. This makes it difficult to use liquids like water, with a refractive index of 1.33 as a core medium, because very few materials have the

lower index required for the cladding material [9]. Moreover, hollow waveguides become impossible because no material has an index lower than that of air (n = 1).

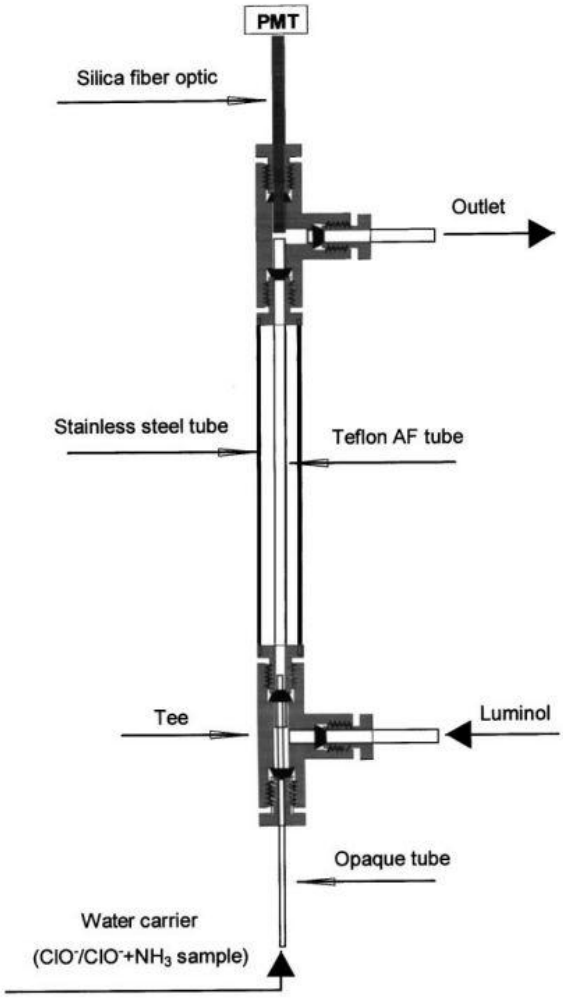

Figure 1.3 – The schematic of a chemiluminesce detector created with a Teflon AF filled liquid core waveguide [10].

Some approaches for index guiding in water cores do exist. Teflon AF is an amorphous fluorinated polymer with an index of 1.29 [11] and it has been used to create capillary tubing waveguides, where the core can be almost any transparent liquid. When filled with water, very high waveguide losses of ~3 dB/μm have

been reported [11]. Nevertheless, this approach has been used to fabricate liquid core waveguides for a variety of applications including Raman spectroscopy [11], and chemiluminescence [10], [12]. An example of a chemiluminescence detector is shown in Fig. 1.3; it incorporates both a conventional fiber along with a hollow core Teflon AF cladding fiber.

Planar designs that employ Teflon AF to enable index guiding in an aqueous core have also been realized [13], but challenges related to adhesion and the requirement for spin-coating increase the difficulty of fabrication [9].

1.3.2 Anti-Resonant Reflecting Optical Waveguide (ARROW)

ARROWs employ many of the same principles as the hollow Bragg waveguides that are the main subject of this thesis and which are discussed in Chapters 3, 4 and 5. As discussed above, conventional waveguides rely on total internal reflection at the boundary between a high index core material and a lower index cladding material [1]. On the other hand, ARROWs are based on constructively interfering reflections from two or more boundaries in a multilayer cladding structure. Each layer in the cladding can be viewed as a Fabry-Perot cavity, and the layer thickness is adjusted to ensure anti-resonance at the target wavelength [14]. The finite transmission of the cladding layers results in a leaky waveguide, but the loss can in principle be reduced by increasing the number of periods. Each additional layer decreases the loss by roughly three times [1]. The layer thickness must be relatively accurate to achieve low loss light propagation. The ARROW

concept was first described by Duguay *et al*., including the thickness condition for an anti-resonant cladding layer:

$$t_j = \frac{\lambda}{4n_j}(2M+1)\left[1-\frac{n_c^2}{n_j^2}+\frac{\lambda^2}{4n_j^2 d_c^2}\right]^{-1/2}. \qquad 1.3$$

Here λ is the wavelength, d_c is the thickness of the core, M is an integer representing the anti-resonance order and n_j and n_c are the indices of the jth layer and core respectively [1] . These symbols correspond to Fig. 1.4 which shows a cross section of an arrow waveguide.

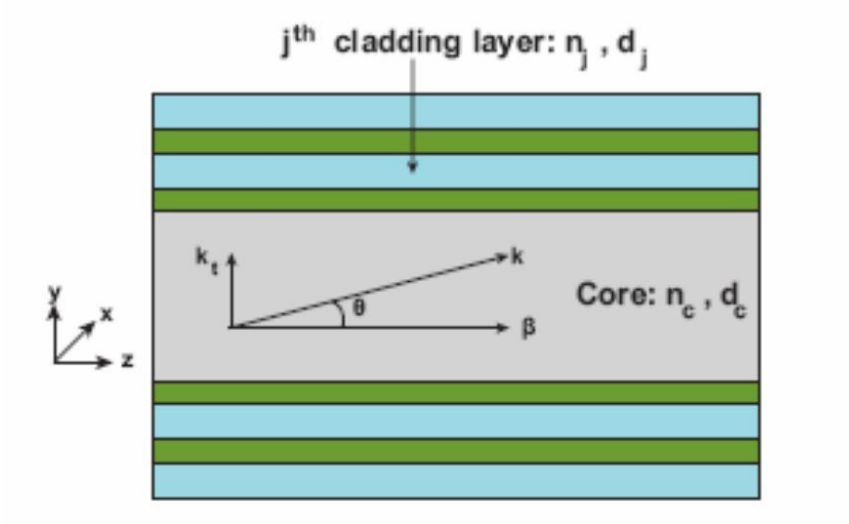

Figure 1.4 – A cross section of an ARROW with the nomenclature that is used to describe the fabrication of the waveguide, adapted from [1].

ARROWS can be viewed as a more general case of the Bragg waveguide described in Chapter 2. Bragg waveguides have periodic claddings and confine light within the photonic bandgap. ARROWs can deviate from periodicity, since the mode order M can take any integer value, and can be different for each cladding layer. Both ARROW and Bragg waveguides rely on constructive

interference in multilayer claddings, and in fact both guidance mechanisms can be present in a single waveguide [15]. If the guidance is due to bandgap reflection in a periodic cladding structure the waveguide is called a Bragg waveguide.

1.4 Conventional Approaches to Fabricating Integrated Hollow Waveguides

The current techniques for creating integrated hollow waveguides can be classified into three categories: wafer bonding [16], self-sealing[17], and sacrificial core [18]. In the past, these methods have all been used to create microfluidic channels [19]. The sacrificial core method is attractive because it allows for a high-fidelity definition of the core region by patterning the sacrificial layer [19]. Typically a type of CVD is used as the deposition method, because of its ability to form uniform and conformal layers on non-planar, pre-patterned surfaces. Schmidt *et al.* [19], used PECVD because of its low deposition temperature, but pointed out that the optical losses of their layers are relatively high.

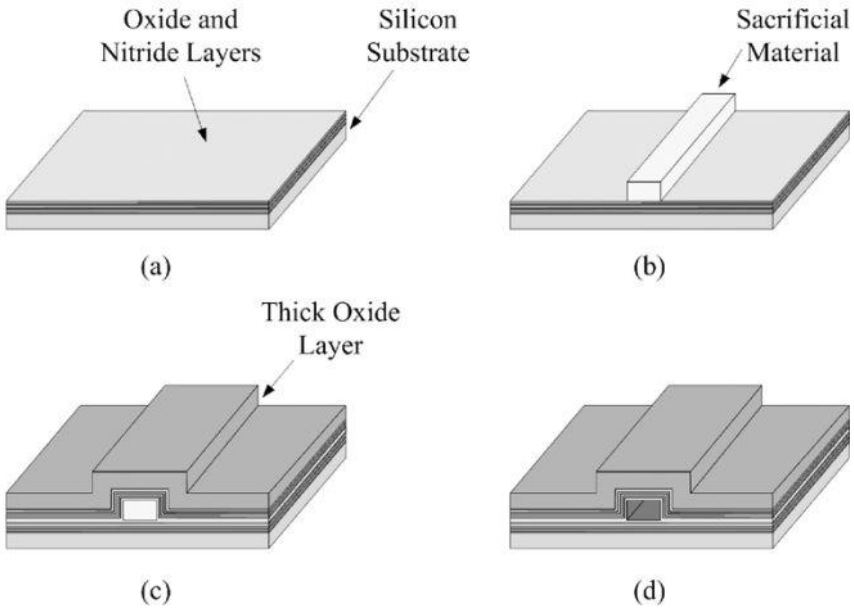

Figure 1.5 – A simplified diagram of the fabrication of a silicon-based ARROW [19]. Silicon nitride and oxide are used for the waveguide cladding and the sacrificial material (SU-8 polymer) is removed in a wet etch process.

They contrasted this with liquid phase chemical vapour depositions (LPCVD), which requires very high temperature but produces very dense, high stress films with low optical losses. They used the LPCVD method to produce ARROWs with a sacrificial core of SU8 polymer surrounded by cladding layers of SiN and SiO_2; the process is outlined in Fig. 1.5. The process basically involves depositing a bottom cladding of the two dielectric layers followed by spinning and patterning the SU8 sacrificial core. A top cladding is then deposited after which the SU8 can be selectively etched to produce a rectangular hollow square waveguide. Fig. 1.6 shows an SEM image of the finished product.

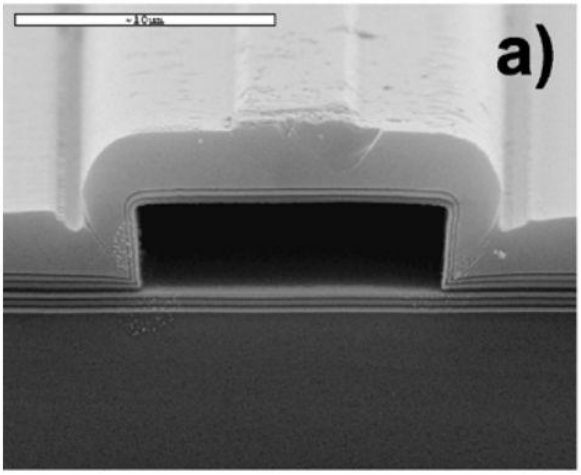

Figure 1.6 – SEM image an ARROW produced from a silicon-based sacrificial etch process [9].

Using wafer bonding, Bragg waveguides with hollow core diameters as small as 1.3 μm have been reported [20]. In another process, [21], ARROW waveguides were formed using two coated silicon wafers that were subsequently fused together using direct wafer bonding. The core is defined on one of the wafers using an anisotropic dry etching process. PECVD was used to create the anti-resonant coating on the two wafers before they were bonded together. A diagram of the wafer-bonded waveguide is shown in Fig. 1.7.

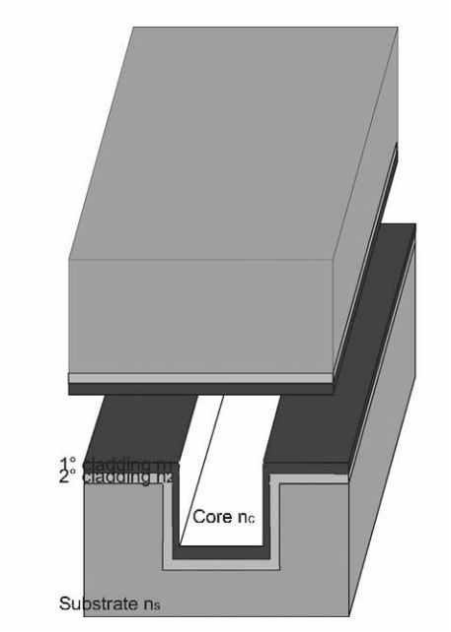

Figure 1.7 - A hollow core ARROW formed using wafer bonding adapted from [21].

Problems can arise relating to alignment of the two wafers, as the thickness of the cladding layers is on the order of 100 nm. Smaller core heights increase the difficulty as any air gaps can significantly alter the propagation of the light through the core [20].

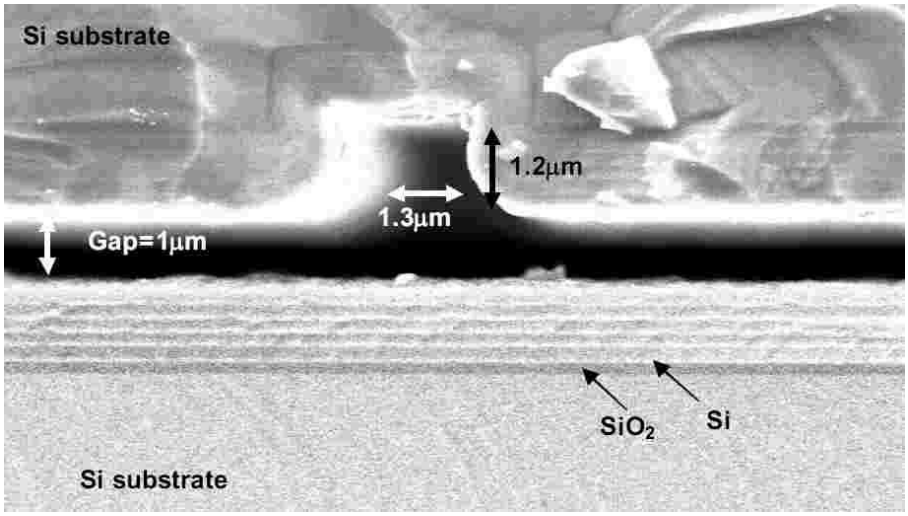

Figure 1.8 - An SEM image of a wafer bonded ARROW with a 1 μm air gap [20].

In the case of a Bragg waveguide with a 1.3 μm core diameter, a 1 μm air gap was found (see Fig. 1.8) and attributed to the roughness of the PECVD layers. The self-sealing process involves etching the path of the waveguide into a silicon wafer and then sealing the trench with silicon. Small gas inlets are placed periodically along the trench to allow the deposition of thin films inside the sealed waveguide. One design, depicted in Fig. 1.9, is a dielectric hollow waveguide with claddings comprised of alternating layers of silicon and silicon dioxide. This created a Bragg waveguide with high bending efficiency at a wavelength of 1.5 μm [22].

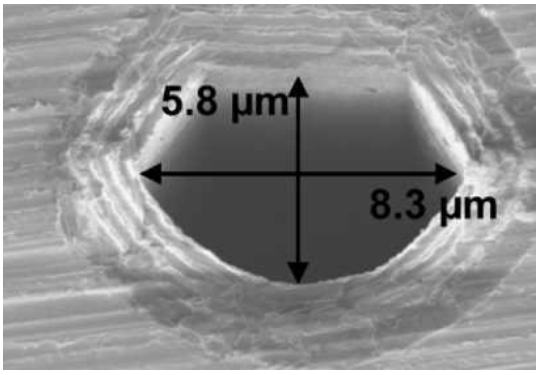

Figure 1.9 - A cross sectional SEM image of a self-sealed Bragg waveguide, [22]. The structure is comprised of alternating silicon and silicon dioxide layers.

1.5 Outline of Thesis

This main focus of this thesis is the development of a set of processes for fabricating silicon-based self-assembled hollow Bragg waveguides. Chapter 1 outlined some possible applications for this type of photonic device including applications in lab-on-chip systems, optofluidics, and microspectrometry.

Furthermore, conventional fabrication methods for hollow integrated waveguides are reviewed.

In Chapter 2, relevant background theory related to the deposition of thin films is provided. This begins with a discussion of standard techniques, especially evaporation and sputtering. The main sources of stress in thin films, including both intrinsic and extrinsic sources, are then reviewed. Emphasis is placed on the control of stress in sputtered thin films, since sputtering is the main technique employed in subsequent Chapters. Chapter 2 also contains an overview of omnidirectional Bragg reflectors, and ends with a brief description of the concept of a Bragg reflection waveguide.

Chapter 3 is a description of the experimental work conducted using previously developed hollow waveguides.. The waveguides are comprised of chalcogenide glass and polymer but were fabricated using a buckling self-assembly process which was the impetus for the work described in Chapter 4. Chapter 3 describes thermal tuning experiments using the first generation hollow waveguides.

Chapter 4 details the bulk of the research that was done towards completion of this thesis. It describes the development of a silicon-based waveguide process that was a natural extension of the work done with the polymer and glass waveguides. The fabrication process for the Bragg omnidirectional reflectors, using sputtering and electron beam deposition, which are used as the upper and lower cladding of the waveguides, is explained along with results from the optical data.

Chapter 5 gives an overview of the final product that was produced from the methods described in Chapter 4. Details regarding the optical characterization of the waveguides are presented.

1.6 Works Cited

[1] D. Conkey, "On Chip Atomic Spectroscopy," M.S.c, Brigham Young, 2007.

[2] H. Schmidt and A. Hawkins, "Optofluidic waveguides: I. Concepts and implementations," *Microfluidics and Nanofluidics*, vol. 4, Jan. 2008, pp. 3-16.

[3] T.M. Squires and S.R. Quake, "Microfluidics: Fluid physics at the nanoliter scale," *Reviews of Modern Physics*, vol. 77, Oct. 2005, p. 977.

[4] G.M. Whitesides, "The origins and the future of microfluidics," *Nature*, vol. 442, Jul. 2006, pp. 368-373.

[5] A. Ehlert and S. Buettgenbach, "Automatic sensor system for groundwater monitoring network," *Proc. SPIE*, vol. 3857, 1999, pp. 61-69.

[6] X. Heng, D. Erickson, L.R. Baugh, Z. Yaqoob, P.W. Sternberg, D. Psaltis, and C. Yang, "Optofluidic microscopy?a method for implementing a high resolution optical microscope on a chip," *Lab on a Chip*, vol. 6, 2006, p. 1274.

[7] H. Craighead, "Future lab-on-a-chip technologies for interrogating individual molecules," *Nature*, vol. 442, Jul. 2006, pp. 387-393.

[8] F.K. Balagadde, L. You, C.L. Hansen, F.H. Arnold, and S.R. Quake, "Long-Term Monitoring of Bacteria Undergoing Programmed Population Control in a Microchemostat," *Science*, vol. 309, Jul. 2005, pp. 137-140.

[9] J. Barber, "Fabricaiton of Hollow Optical Waveguides on Planar Substrates," Brigham Young University, 2006.

[10] P.K. Dasgupta, Z. Genfa, J. Li, C.B. Boring, S. Jambunathan, and R. Al-Horr, "Luminescence Detection with a Liquid Core Waveguide," *Analytical Chemistry*, vol. 71, Apr. 1999, pp. 1400-1407.

[11] R. Altkorn, I. Koev, R.P. Van Duyne, and M. Litorja, "Low-loss liquid-core optical fiber for low-refractive-index liquids: fabrication, characterization, and application in Raman spectroscopy," *Applied Optics*, vol. 36, Dec. 1997, pp. 8992-8998.

[12] J. Li and P.K. Dasgupta, "Chemiluminescence detection with a liquid core waveguide: Determination of ammonium with electrogenerated hypochlorite based on the luminol-hypochlorite reaction," *Analytica Chimica Acta*, vol. 398, Oct. 1999, pp. 33-39.

[13] A. Datta, In-Yong Eom, A. Dhar, P. Kuban, R. Manor, I. Ahmad, S. Gangopadhyay, T. Dallas, M. Holtz, H. Temkin, and P. Dasgupta, "Microfabrication and characterization of teflon af-coated liquid core waveguide channels in silicon," *IEEE Sensors Journal*, vol. 3, 2003, pp.

788-795.
[14] M.A. Duguay, Y. Kokubun, T.L. Koch, and L. Pfeiffer, “Antiresonant reflecting optical waveguides in SiO2-Si multilayer structures,” *Applied Physics Letters*, vol. 49, 1986, p. 13.
[15] N.M. Litchinitser, A.K. Abeeluck, C. Headley, and B.J. Eggleton, “Antiresonant reflecting photonic crystal optical waveguides,” *Optics Letters*, vol. 27, 2002, pp. 1592-1594.
[16] R. Bernini, S. Campopiano, and L. Zeni, “Silicon micromachined hollow optical waveguides for sensing applications,” *Selected Topics in Quantum Electronics, IEEE Journal of*, vol. 8, 2002, pp. 106-110.
[17] G.R. Hadley, J.G. Fleming, and S. Lin, “Bragg fiber design for linear polarization,” *Optics Letters*, vol. 29, Apr. 2004, pp. 809-811.
[18] D. Bhusari, H. Reed, M. Wedlake, A. Padovani, S. Allen, and P. Kohl, “Fabrication of air-channel structures for microfluidic, microelectromechanical, and microelectronic applications,” *Microelectromechanical Systems, Journal of*, vol. 10, 2001, pp. 400-408.
[19] H. Schmidt, Dongliang Yin, J. Barber, and A. Hawkins, “Hollow-core waveguides and 2-D waveguide arrays for integrated optics of gases and liquids,” *Selected Topics in Quantum Electronics, IEEE Journal of*, vol. 11, 2005, pp. 519-527.
[20] S. Lo, M. Wang, and C. Chen, “Semiconductor hollow optical waveguides formed by omni-directional reflectors,” *Optics Express*, vol. 12, Dec. 2004, pp. 6589-6593.
[21] R. Bernini, S. Campopiano, L. Zeni, and P.M. Sarro, “ARROW optical waveguides based sensors,” *Sensors and Actuators B: Chemical*, vol. 100, Jun. 2004, pp. 143-146.
[22] T.C. Shen, Y.S. Kim, J.A. Bur, and S. Lin, “Optical Characterization of Bending Efficiency in On-Chip Hollow-Core Bragg Waveguides at 1500 nm,” *Journal of Lightwave Technology*, vol. 28, Jun. 2010, pp. 1714-1719.

Chapter 2 Controlled Thin Film Buckling

2.1 Introduction

This chapter discusses some of the background theory that is pertinent to subsequent chapters of the thesis. The different methods used to deposit thin films are outlined, along with a brief theoretical description of related principles. Furthermore, the origins and control of stress in thin films is discussed, including extrinsic and intrinsic sources. Important equations relating to the mechanics of thin film buckling are considered and the concept of controlled buckling through the use of patterned areas of low adhesion is introduced. Finally an introduction to planar omnidirectional reflectors and their use in Bragg reflection waveguides is provided.

2.2 Film Deposition Methods

Many factors influence the mechanical properties of thin films. While the bulk characteristics are a good indicator of a film's suitability for a particular application, the deposition method can significantly affect the material properties. Physical vapour deposition (PVD) is a technique for depositing thin films in which a physical process, such as evaporation, sublimation, or ionic impingement on a target, makes possible the transfer of atoms from a target to the substrate [1]. The two most popular techniques in use are sputtering and evaporation.

In sputtering, the chamber is first evacuated to a low base pressure, ~10^{-7} Torr, in order to remove oxygen and other atmospheric gases. The chamber is then supplied with an inert gas, typically Ar, and stabilized at a pressure of a few mTorr. An imposed electric field, created by applying a voltage to the target, accelerates the ions of the sputtering gas and causes a plasma to form. The ions strike the target and the momentum transfer causes the neutral atoms of the target to become dislodged. These atoms transfer through the plasma and condense on the substrate resulting in film growth. Multiple variations of the sputtering technique exist [1]: DC sputtering, radio frequency sputtering, magnetron sputtering (which involves application of magnetic field in superposition with the electric field between the substrate and target) and bias sputtering (where the substrate is biased with a DC or rf voltage to vary the flux of the charged species). A significant advantage of using a sputtering system is the ability to control the stress level in deposited films. In particular, magnetron sputtering allows deposition at lower pressures resulting in greater free atomic path lengths. This allows much greater control over thin film growth and properties (See Sec. 2.3.1). An important example with regards to this thesis was reported by D. Hoffman: he was able to deposit films in a large range of stresses, from tensile to strongly compressive, simply by varying deposition conditions such as deposition rate and pressure [2].

Evaporation uses thermal energy to heat up a source material, from which atoms are evaporated and then condense on the substrate. Several methods exist for heating the source material. The simplest involves using the resistance of a

crucible, or strip of refractory metal, in which the evaporation metal is in thermal contact [1]. Disadvantages of this technique include contamination by heaters and crucibles, and relatively low input power levels [3]. This implies difficulties in the deposition of pure or high melting point materials. These disadvantages are mostly eliminated by using electron-beam (e-beam) heating. In this method, a beam of electrons is directed at the source material using a strong magnetic field. The electrons are emitted from heated filaments that are not in the line of sight of either the evaporant or the substrate, which reduces film contamination [3]. The deposition material is kept in a crucible or depression of a water-cooled copper hearth. A schematic showing the basic components of the e-beam deposition system is provided in Fig. 2.1.

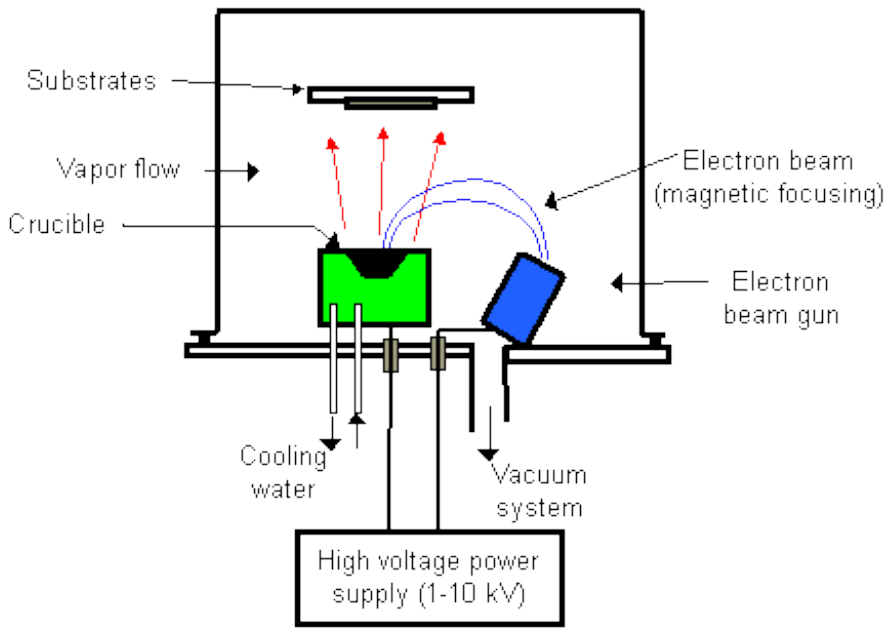

Figure 2.1 - Schematic of an e-beam power supply that is used in multilayer depositions, adapted from Ref. [4].

The e-beam can be automated to scan the crucible, resulting in a greater degree of control over the deposition rate and temperature. The purity of the film can be assured is relatively good because only a small amount of the source material is heated, while the rest essentially forms a crucible around the melt.

2.3 Thin Film Stress

The effect of stress on thin films was recognized and documented as far back as the nineteenth century. In 1865, with the purpose of fabricating a true "flat" mirror for a Newtonian telescope, the Earl of Rosse coated glass with silver and then electroplated the surface with copper [5]. He noted that, "however firmly and closely the silver film had adhered to the glass", as soon as the copper was deposited on the silver, the entire film detached from the glass leaving the surface in a convex shape. In 1909 Stoney made a similar discovery, when he found that copper electrodeposited on silver films in searchlight reflectors "peeled off" when the copper layer was thicker than 10 μm [6].

From this observation, Stoney went on to conclude that a substrate with a metal film deposited on it will have a compressive or tensile force applied to it, consequently bending the substrate. To quantify the relationship, Stoney electroplated 102 mm long steel rulers with 5.6 to 46.2 μm of nickel. He considered the film thickness, amount of curvature, and the elastic modulus of the ruler in order to estimate the tensile stress of the nickel film, and estimated a tensile stress in 152 to 296 MPa range [1]. Despite advances in experimental methods used to determine the curvature of a substrate, the underlying principles

discovered by Stoney, and encapsulated by what we now call Stoney's formula, are to this day the main theoretical tools we apply to the study of thin film stress.

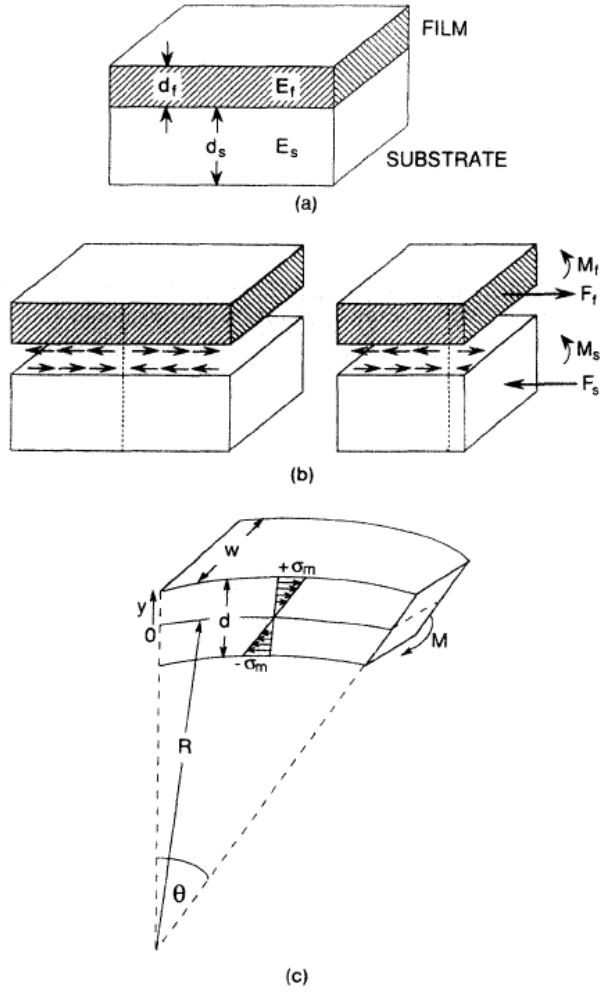

Figure 2.2 - Stress forces and moments in a film/substrate combination [3]: (a) combined structure; (b) free body diagrams with interfacial forces and end moments; (c) elastic bending under applied moment.

Stoney's equation can be derived by studying a simple diagram such as Fig. 2.2, which shows a substrate, with thickness d_s and Young's modulus of Y_s, covered by a film of thickness d_f and Young's modulus Y_f. Forces at the substrate/film interface can arise from a variety of causes. This can be represented by an equal

and opposite force and moment acting on both the film (F_f, M_f) and substrate (F_s, M_s), as shown in Fig. 2.1b. The force F_f acts uniformly along the cross-sectional area (d_f•w), resulting in the film stress. In order to satisfy mechanical equilibrium, the net force and bending moment on the film/substrate cross section must be zero, allowing the force and moment to be equated:

$$\frac{(d_f+d_s)F_f}{2} = M_f + M_s \ . \qquad 2.1$$

Fig. 2.1c displays an isolated beam deformed by moment *M*. The stress on the beam varies linearly from maximum compression ($-\sigma_m$) to maximum tension ($+\sigma_m$). Utilizing Hooke's law as a function of the beam radius of curvature *R*, and angle θ subtended yields [1]:

$$\sigma_m = \frac{Y\{\left(R+\frac{d}{2}\right)\theta - R\theta\}}{R\theta} = \pm\frac{Yd}{2R}. \qquad 2.2$$

Assuming a linear stress distribution, the bending moment across the beam section,

$$M = 2\int_0^{d/2} \sigma_m w(\frac{y}{d/2})\, ydy = Yd^3w/12R. \qquad 2.3$$

Equation 2.3 can be extended to find the bending moment in the film or substrate simply by taking the respective thickness and Young's modulus values, and leading to:

$$M_f = \frac{Y_f d_f^3 w}{12R} \quad M_s = \frac{Y_s d_s^3 w}{12R}. \qquad 2.4$$

Allowing for biaxial-stress distributions in the films requires the term *Y* to be replaced by *Y/(1-ν),* where ν is Poisson's ratio of the material. Substituting in these terms gives:

$$\frac{(d_f+d_s)F_f}{2} = \frac{Y_f d_f^3 w}{12R(1-\nu_f)} + \frac{Y_s d_s^3 w}{12R(1-\nu_s)}. \qquad 2.5$$

For most films d_s is much larger then d_f, so the film stress σ_f can be approximated by:

$$\sigma_f = \frac{Y_s d_s^2 w}{6R(1-\nu_s)d_f}, \qquad 2.6$$

which is Stoney's equation.

The origin of substrate curvature can be explained by first considering a substrate/film combination bonded together and without any resultant stress. If the bond between the substrate and film was removed, the dimensions of both would stay constant due to the lack of stress. If the film was reattached to the substrate, the substrate curvature and therefore stress would be zero; however, if the lateral dimensions of the film are altered prior to reattachment to the substrate, stresses and strains must develop. This is because in order for the film to be reattached to the substrate, it would need to be stretched or compressed to its original dimensions. Once reattached, the relaxation of the forces would result in substrate curvature [7].

Many different factors can contribute to a difference in 'free' dimensions between the substrate and film. Stresses are often described as intrinsic or extrinsic, although these are broad and overlapping categories. Intrinsic stresses

arise following growth on substrates or previous layers. The substrate temperature during deposition, growth chamber conditions, and combination of materials involved all play a significant role in determining the amount of intrinsic stress. Some common mechanisms, reviewed by Doerner *et al.* [8], included:

- surface and/or interface stress,
- cluster coalescence to reduce surface area,
- vacancy annihilation,
- grain boundary relaxation
- shrinkage of grain boundary voids
- incorporation of impurities
- phase transformations and precipitation,
- moisture adsorption or desorption.

Extrinsic stresses typically arise after deposition and can be caused by many different physical effects including:

- temperature change with unequal thermal expansion coefficients,
- piezoelectric or electrostrictive response to an electric field,
- electrostatic or magnetic forces,
- electromigration,
- chemical reactions,
- stress induced phase transformation
- plastic or creep deformation

Thermal strain arises when there is a mismatch between the thermal expansion coefficients of the substrate and the film. Because a large portion of depositions occur at increased temperature thermal, strain is common and often a significant source of stress. The corresponding thermal elastic strain of the film can be quantified by,

$$\varepsilon = -(\sigma_f - \sigma_s)(T - T_0) \quad , \qquad 2.7$$

where σ_f and σ_s are the linear expansion coefficients of the film and substrate, respectively, T is the current temperature, and T_0 is the deposition temperature.

2.3.1 Controlling Stress in Sputtered Thin Films

Buckling is largely dependent on the amount of compressive stress present in the thin film; therefore, control over the stress in the multilayer Bragg reflector was a critical component of this project. When deposited by sputtering, most materials can exhibit either tensile or compressive stress depending on the deposition parameters. Although the maximum level of stress and the locations of the transition between tensile and compressive stress varies, some general trends are evident in most materials. For example, we found that sputtering tungsten at a typical deposition pressure of 7 mTorr produced a film that was 2 GPa tensile while changing the deposition pressure to 1 mTorr resulted in a -2 GPa compressive film. This is consistent with work reported by Thornton and Hoffman, who did extensive work on stress of films deposited by cylindrical

sputtering systems [2]. They found that the actual transition between tensile and compressive stress is an abrupt function of certain deposition parameters. For example, they reported the behaviour of chromium sputtered at 1 nm/s as the deposition pressure was varied (Fig. 2.3).

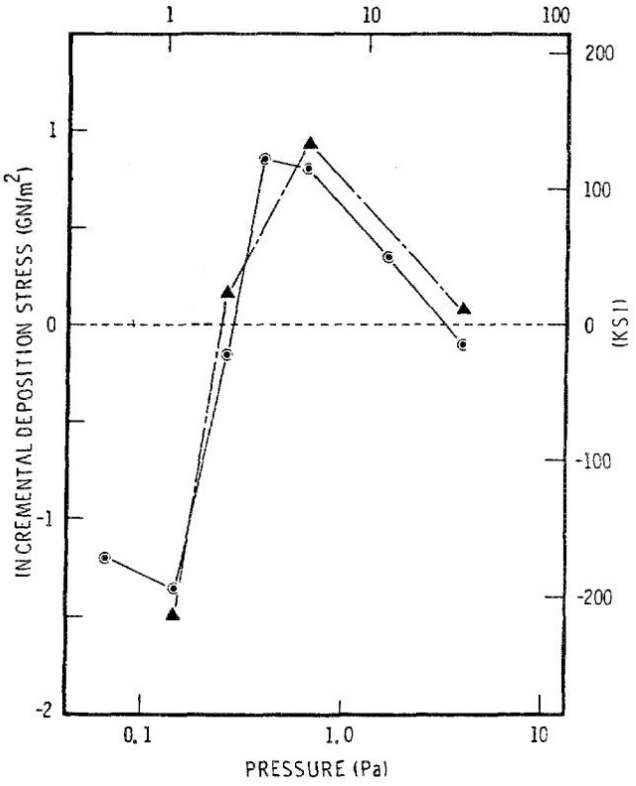

Figure 2.3 - Stress in sputtered chromium deposited with different deposition pressures. Adapted from [2].

Stress was found to change abruptly from compressive to tensile as the pressure is increased in the .1 to 1 Pa range. Furthermore, their results showed that most sputtered materials exhibited a compressive to tensile stress transition of this type (Fig 2.4). Interestingly an analogous transition could be found by varying other

parameters such as working gas pressure, deposition rate, and even the angle of deposition [2].

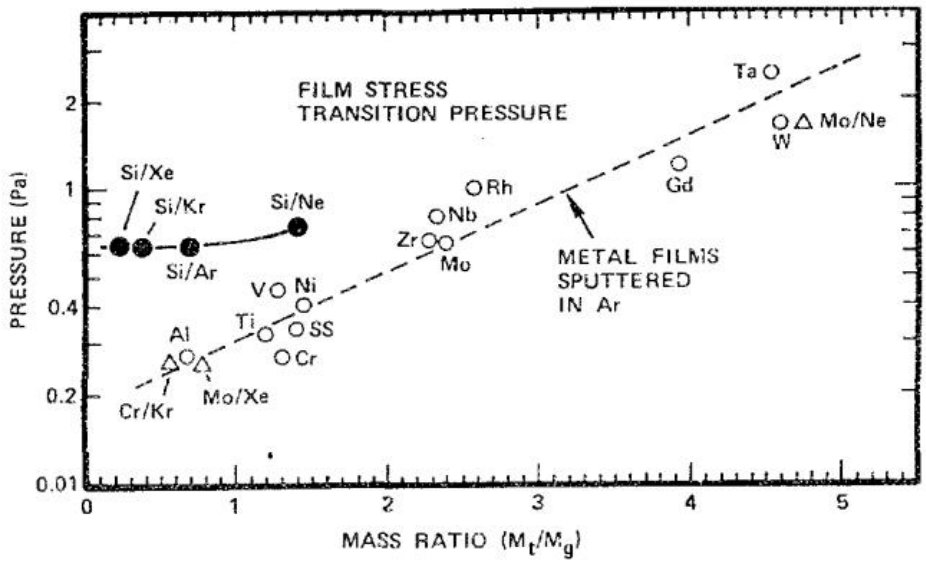

Figure 2.4 - The deposition pressure where various materials change from compressive to tensile stress. The working gas is argon unless otherwise specified. Dielectric films are denoted by solid circles. The data was adapted from [2].

The ratio T/T_m, where T is the deposition pressure and T_m is the melting point of the deposition material, was determined to be especially important to the intrinsic stress. The effects of both surface and bulk diffusion increase as T/T_m gets larger. Materials with a high melting point and low T/T_m (such as tungsten) typically exhibit higher levels of intrinsic stress for a given set of deposition conditions. On the other hand the pressure dependence of stress for a given material is thought to be a result of the increasing rate of collisions of sputtered atoms for increasing pressure.

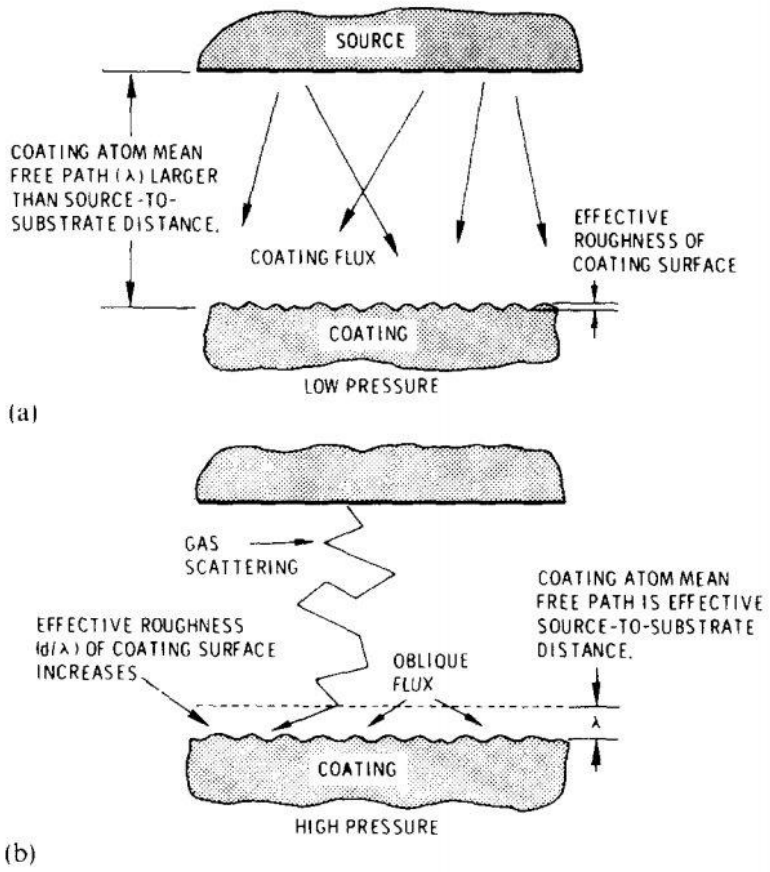

Figure 2.5 - Schematic depicting the influence of working pressure on the surface roughness of a sputtered thin film. (a) The low pressure allows the coating atoms to arrive at the substrate with a collision. (b) Multiple collisions with gas atoms result in a more oblique flux of coating atoms.

These collisions increase the number of atoms that arrive at the substrate with an oblique incidence angle, leading to shadowing and a rougher more porous thin film. This is illustrated in Fig. 2.5: as the mean free path (λ) of the sputtered atoms is increased with lower pressure, the distance from the last collision to the substrate becomes larger and, on average, the incidence angle at the substrate is decreased. Thus, the coating roughness (d) is a function of λ; specifically large λ correlates with lower roughness.

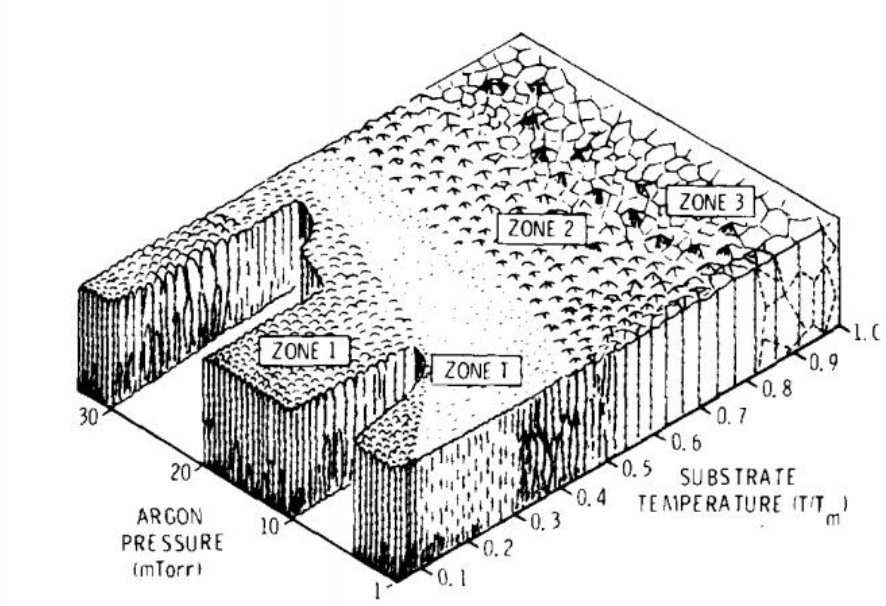

Figure 2.6 - The structure zone model proposed by Thornton depicting sputtered film properties as a function of the working gas pressure and substrate temperature [9].

Thornton proposed a graphical representation of the thin film microstructure dependence on T/T_m and working gas pressure, Fig. 2.6.

Zone T (transition) films are dense and fibrous and form a highly reflective surface. Typically, they form on smooth surfaces with a coating flux that arrives normal to the surface. Large intrinsic stresses can arise in zone *T* [9]. Zone 1 coatings consist of tapered crystals separated by voided boundaries. This structure results from an uneven or rough substrate which promotes shadowing. Extreme zone 1 films cannot support large stresses because of their porosity [9]. Zone 2 films have columnar grains separated by distinct intercrystalline boundaries. Intrinsic stresses are limited in this zone due to recovery, wherein the energy stored in the film acts as a thermodynamic driving force and relaxes the stress by vacancy, interstitial, and dislocation movement [10]. Zone 3 is in a range where

bulk diffusion dominates the film and the intrinsic stress becomes limited accordingly. Effects of these process variables with relation to stress are summarized in Fig. 2.7. From this discussion it is clear that, for a given material and sputtering system, pressure is the main variable that can be exploited to control stress.

Compressive	Variable	Tensile
Negative	Substrate Bias	Positive
Low	Gas pressure	High
Low	Gas atomic mass	High
High	Target atomic mass	Low

Table 2.1- Effects of multiple sputter process variables on the stress of the deposited thin films, adapted from [2].

2.4 Buckling Delamination of Thin Films

2.4.1 Spontaneous Formation of Delamination Buckles

As the amount of stress increases for a given film/substrate combination the probability of failure for the system increases. If the stress is compressive and sufficiently high, a variety of relief mechanisms exist including: hillock formation [11], peeling due to adhesion failure [12], creep and plastic flow [13], and buckling of the film from the substrate [14]. A film that is subjected to an equi-biaxial mismatch stress is particularly susceptible to delamination buckling [1], where the adhesion between the film and substrate fails and a portion of the film buckles away from the substrate forming a blister. Spreading of the blister can occur because the interface of the film and substrate is loaded with bending and

shear stress. Depending on conditions, the buckling can result in multiple patterns or modes including circular blisters, the 'telephone cord buckle', and long straight-sided buckles (often referred to as Euler buckles). Fig 2.7 shows examples of straight sided buckles and telephone-cord like buckles formed using the process described in Chapter 5. These types of failures incorporate both buckling and interfacial crack propagation in order to release the compressive stress.

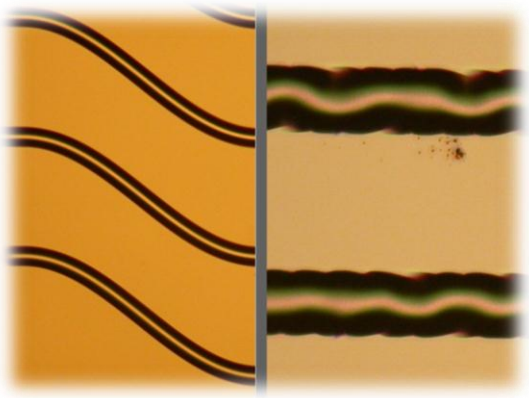

Figure 2.7 - Two different types of buckles produced with the silicon-based buckling process from Chapter 5. (left) Straight-sided buckles Euler buckles on a patterned substrate. (right) Telephone-cord buckles.

2.4.2 Mechanics of Buckling

The straight-sided, infinitely long buckle is the simplest case to analyze [1], and is summarized in the following. Consider a film under an equi-biaxial mismatch stress which is assumed to be compressive, $\sigma_f < 0$, as schematically shown in Fig. 2.8. The film is bonded to a much thicker substrate and has an elastic strain energy given by:

$$\frac{\sigma_f(1-\nu_f)}{Y_f}, \qquad 2.8$$

where Y_f is Young's modulus and ν_f is Poisson's ratio. If a section of the interface becomes delaminated for any reason, it is possible for the film to laterally deflect away from the substrate.

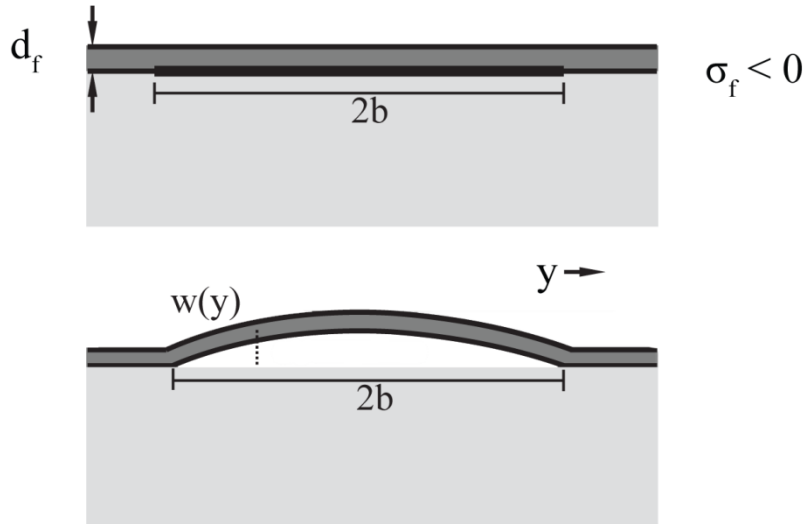

Figure 2.8 - Cross-sectional illustration of a debonded region for a film under compressive stress. w(y) represents the height of buckle as a function of lateral position across the buckle.

Energetics of the system will determine if the film does actually deflect. Deflection allows elongation of the midplane of the film which decreases the strain energy. This effect can be somewhat mitigated by the bending deformation that accompanies the lateral deflection. If the resulting change in energy is negative, the film undergoes 'spontaneous lateral deflection over the debonded region,'[1]; in other words the film buckles. If the bending deformation introduces a net positive change in the energy of the film, the buckling will not occur.

The analysis does not take into account the energy changes to the film outside of the buckling area; furthermore, energy changes in the substrate are not considered. This is due to the assumption that the buckled portion of the film is

rigidly clamped along the boundary of the delamination. The reason for this restriction is that the delaminated area is typically found to be much more responsive to changes in forces then the still-bonded portion of the substrate. This approximation is valid as long as the Young's modulus of the substrate is not less than one fifth that of the film [15]. Despite this restriction, the buckled section of the film still exerts forces and moments on the rest of the substrate. After buckling these forces are determined by the configuration of the film.

Once buckling occurs, the stress distribution on the film and substrate is significantly altered. Before delamination, the force transferred between the substrate and film is zero; after buckling, a force must be induced on the interface in order to maintain equilibrium. Also the abrupt transition between the relaxed state of the buckle and the compressively stressed bonded region leads to a concentration of stress across the edge region. This concentration can lead to a change in size and shape of the buckled region, due to ongoing delamination. The type of buckle that governs initially is the Euler mode. Detailed analysis of the buckling and post-buckling behaviour of thin films is available in the literature and several important equations have been derived relating buckle behaviour to stress and other substrate conditions [14],[15],[17],[18]. Hutchinson *et al.* describe the critical compressive biaxial stress, σ_c, at the onset of buckling as

$$\sigma_c = \frac{\pi^2}{12}\frac{Y}{\left(1-\upsilon_f^2\right)}\left(\frac{d_f}{b}\right)^2, \qquad 2.9$$

where d_f is the film thickness, 2b is the buckle width, Y and ν_f are the Young's modulus and Poisson's ratio of the film, respectively. The amplitude of the buckle is described by

$$w(y) = \frac{\xi d_f}{2}\left(1 + \cos\left(\frac{\pi y}{b}\right)\right), \qquad 2.10$$

where ξ is dimensionless and relates to the residual stress, σ_o, by

$$\xi \equiv \frac{w(0)}{d_f} = \sqrt{\frac{4}{3}\left(\frac{\sigma_o}{\sigma_c} - 1\right)}. \qquad 2.11$$

This allows quantitative determination of the critical stress, σ_c, required for the film to buckle with given interface crack width of 2b. Rearranging equation 2.11 and plotting $\xi(\sigma_o/\sigma_c)$ results in a graph of the peak deflection as a function of the residual stress (see Fig. 2.9).

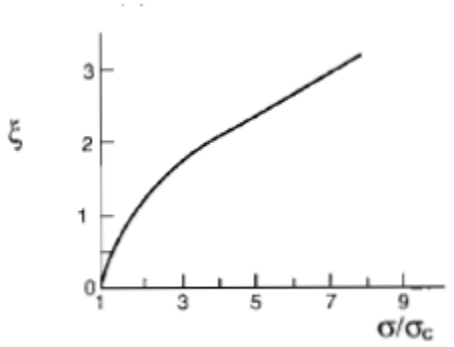

Figure 2.9 - Peak deflection of a one dimensional blister adapted from [17].

2.4.3 Controlled Buckling of Thin Films

Delamination of a thin film is typically viewed as a negative side effect of compressive stress. In fact, it is the most common failure mechanism seen in

compressively thin compressed films. For example, the fabrication of thermal barrier coatings used in gas turbine engines [19] requires understanding of buckling because of the delamination of the zirconia films that are used in the process. However, as the phenomenon becomes better understood, practical applications are becoming increasingly apparent. Some researchers [14],[20],[21] have demonstrated the potential to use delamination buckles as channels for microfluidic and waveguide applications. These types of applications require a large degree of control over the location and morphology of the buckles. In pioneering work, Moon *et al*. [14] used a thin layer of aluminum (3 nm) as the low adhesion layer for subsequently-deposited diamond-like carbon films. With patterns of varying width, they were able to demonstrate and quantify three modes of columnar buckling in the same film. Their results showed that the Euler mode occurs for the least amount of stress followed by the varicose mode and finally the telephone cord mode. The conditions for each mode to occur were determined as a function of the critical compressive stress, Equation. 2.9. The Euler mode formed when the compressive stress on the film, σ_o, exceeds the critical stress but is below 6.5 times the critical stress, $\sigma_o/\sigma_c < 6.5$. When the amount of stress in the film exceeds approximately 6.5 times the critical stress but is less than 7.5 times the critical stress ($6.5 < \sigma_o/\sigma_c > 7.5$) the delaminated film can form what is called a 'varicose buckle'. When the stress is more than 7.5 times the critical stress ($\sigma_o/\sigma_c > 7.5$) the telephone cord buckle will form. Note that the critical stress depends inversely on the buckle width; therefore, wider buckles form at lower stress levels. The cause of the different type of buckles can be related to the energy

release that occurs during the delamination. The Euler buckling reduces initial biaxial compression in only the transversal direction of the buckle. This leaves an appreciable longitudinal compression,

$$\sigma_L = -(1-\upsilon)\sigma_o \,, \qquad 2.12$$

which can induce the secondary buckling (i.e. the varicose or telephone cord buckle) if the stress is high enough [22]. Poisson's ratio plays a role in determining the symmetry of the buckle. Elastic energy theory predicts that the relative energetic cost of shear versus compression increases as υ decreases [22],[23]. Therefore, lower values of υ will result in a symmetric secondary buckling (i.e. the varicose mode), which requires less shear.

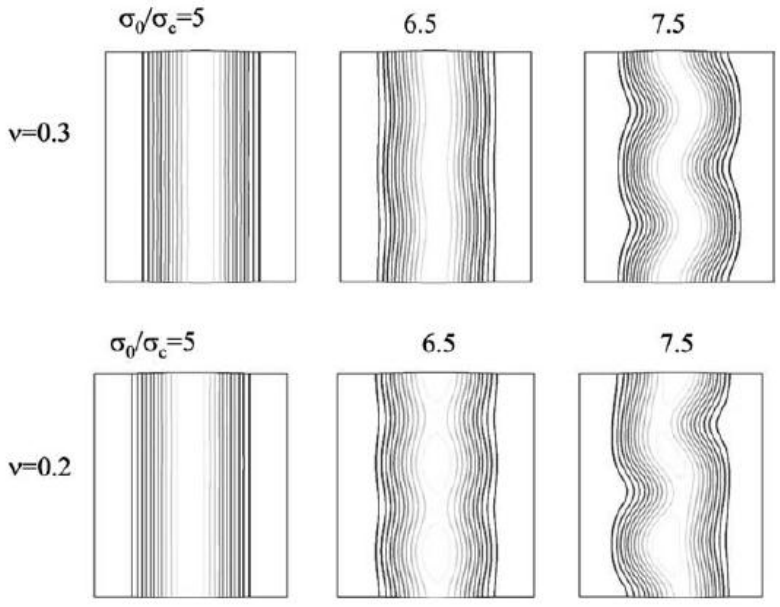

Figure 2.10 - Contour plots of the three main buckling modes at three values of films stress and two values of Poisson's ratio. The film stress gives the lowest values at which that mode will occur [14].

The value of υ corresponding to a shift from symmetric to antisymmetric secondary values is 2.555. The middle images in Fig. 2.10 demonstrate the shift from symmetric to antisymmetric varicose mode buckling. This can be determined by solving the FvK equations and remarkably is a universal value [22]. The ratios for the modes along with depictions of each type of buckle are summed up in Fig. 2.10. Examples for all three types of buckles at different Poisson values were determined by Moon *et al.* and are also shown in Fig. 2.11.

2.5 Bragg Reflection Waveguides with Omnidirectional Claddings

As detailed in Chapter 3-5, the thesis work is focused on the fabrication and characterization of hollow waveguides with omnidirectional Bragg claddings. In the following section a brief overview of omnidirectional Bragg reflectors and Bragg reflection waveguides is provided.

2.5.1 Omnidirectional Bragg Reflectors

A Bragg reflector is a quasi-periodic structure incorporating a number of alternating layers of two different optical materials. The thickness of each layer is typically one quarter the wavelength in that layer, so that the light reflected at each interface is subject to constructive interference. Typically formed using dielectric materials, they offer several advantages over metal reflectors, including: lower absorption, potential for higher reflectance, and superior mechanical robustness [24]. The width and location of the stop band is tunable simply by modifying the stack design [25]. Initially, it was thought that Bragg mirrors could

provide high reflectance over a certain range of incident angles only [24]. Historically, dielectric mirrors with improved angular performance incorporated films with high indices of refraction or large special dispersion properties, or employed multiple contiguous, stacks of films [26],[27]. It has now been shown experimentally and theoretically that simple Bragg mirrors can provide a band of omnidirectional reflectance for all polarizations of incident light, provided that the index contrast is sufficiently high and provided that the index of the incident medium is sufficiently low relative to that of the dielectric materials [28]. Omnidirectional Bragg mirrors are sometimes called one-dimensional photonic crystals. The formation of an omnidirectional bandgap is dependent on a number of factors relating to the thickness and choice of materials, as explained well by Winn *et al*. in Ref. [25]. Alternating layers of thickness d_1 and d_2 and indices of refraction n_1 and n_2, respectively, corresponds to a periodic one-dimensional photonic crystal. Considering the *y* coordinate to be perpendicular to the surface results in homogeneity in the *x* and *z* directions. Incident light is either *s* polarized (**E** perpendicular to the plane of incidence) or *p* polarized (**E** parallel to the plane of incidence) (see Fig. 2.11). The electromagnetic modes are represented by a wave vector, **k**, with the conditions: $0 \leq k_y \leq \pi/a$, $k_z = 0$, $k_x \geq 0$ and $n_2 > n_1$. The band structure for the crystal is constructed by determining the allowed mode frequencies ω_n for each choice of **k,** while the continuous functions, $\omega_n(\mathbf{k})$ for each *n*, are the photonic bands. Fig. 2.11 shows the projected band structure of a quarter-wave stack with $n_1 = 1$ and $n_2 = 2$.

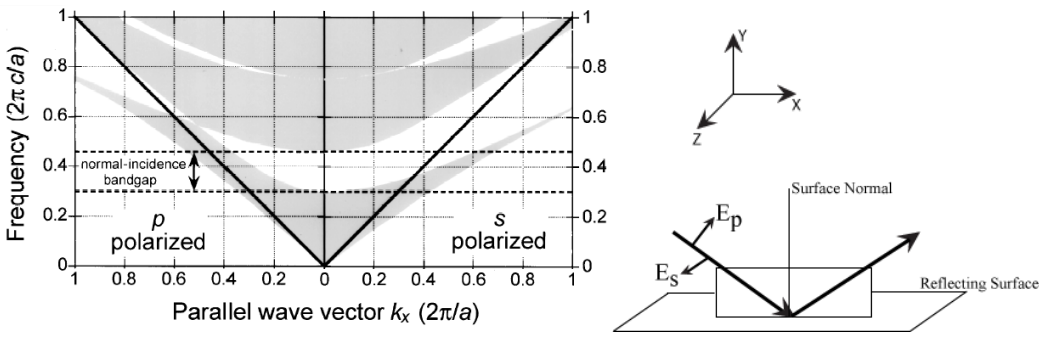

Figure 2.11 – (Left) The propagation modes for a quarter wave stack with $n_1 = 1$ and $n_2 = 2$. The allowed electromagnetic modes are defined by the grey shaded regions. Adapted from [25]. (Right) A diagram detailing the orientation of the propagating modes discussed in the diagram.

The plot was created by using a numerical method to solve Maxwell's equations in a periodic medium, [29]. The gray regions indicate electromagnetic modes for k_y and for generality the frequency is listed as a function of $a = d_1 + d_2$. The plot clearly shows that a complete bandgap does not exist. While this may seem to indicate that omnidirectional reflection would be impossible, other factors must be considered. The propagating states in the crystal are only accessible if they are able to couple to a propagating state that exists in the ambient medium. The electromagnetic modes in the ambient medium are defined by

$$\omega = c(k_x^2 + k_y^2)^{1/2}. \qquad 2.12$$

The solid light lines in Fig. 2.11, $\omega = ck_x$, define the limits of the projected bands in the ambient medium. If these bands do not overlap with the allowed modes of the crystal, then coupling between the two mediums is no longer possible. Therefore in order for an omnidirectional bandgap to exist, there must be a frequency zone for which "the projected bands of the crystal have no states with $\omega > ck_x$", [25]. This is clearly not the case in Fig. 2.11, because the lowest p

bands cross above the line $\omega = ck_x$. This point is defined as the Brewster angle, Equation 2.13, and is determined by the index ratio of the (n_2/n_1) of the crystal.

$$\theta_b = tan^{-1}(n_2/n_1) \qquad 2.13$$

Note, however, that by changing the materials of the photonic crystal, it is possible to alter the location of the Brewster angle and allow the formation of an omnidirectional bandgap.

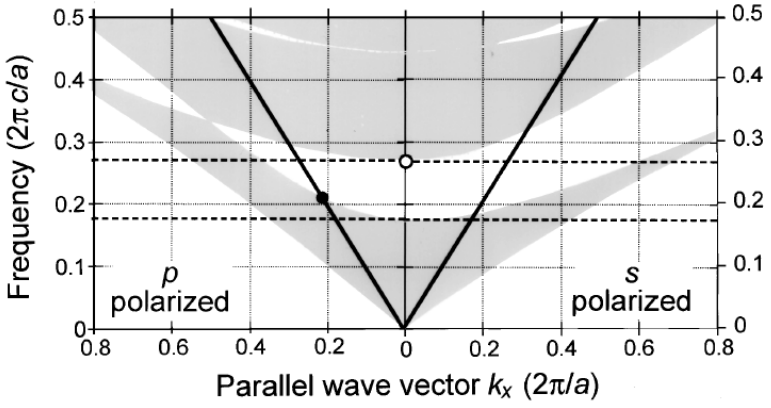

Figure 2.12 - The propagation modes for a quarter wave stack with n_1 = 1.7 and n_2 = 3.4. The omnidirectional bandgap is defined by the two dots while the normal incidence bandgap is marked by the two dotted lines. [25]

Fig. 2.12 shows the band structure of a photonic crystal with n_1 = 1.7 and n_2 = 3.4. It is evident that there is now a full bandgap, since the first and second p bands do not cross anywhere inside of the light lines for the ambient medium. The size of the omnidirectional bandgap is defined by the frequency range between the first two crystal structure bands that extends across the entire ambient medium propagation zone.

2.5.2 Bragg Reflection Waveguides

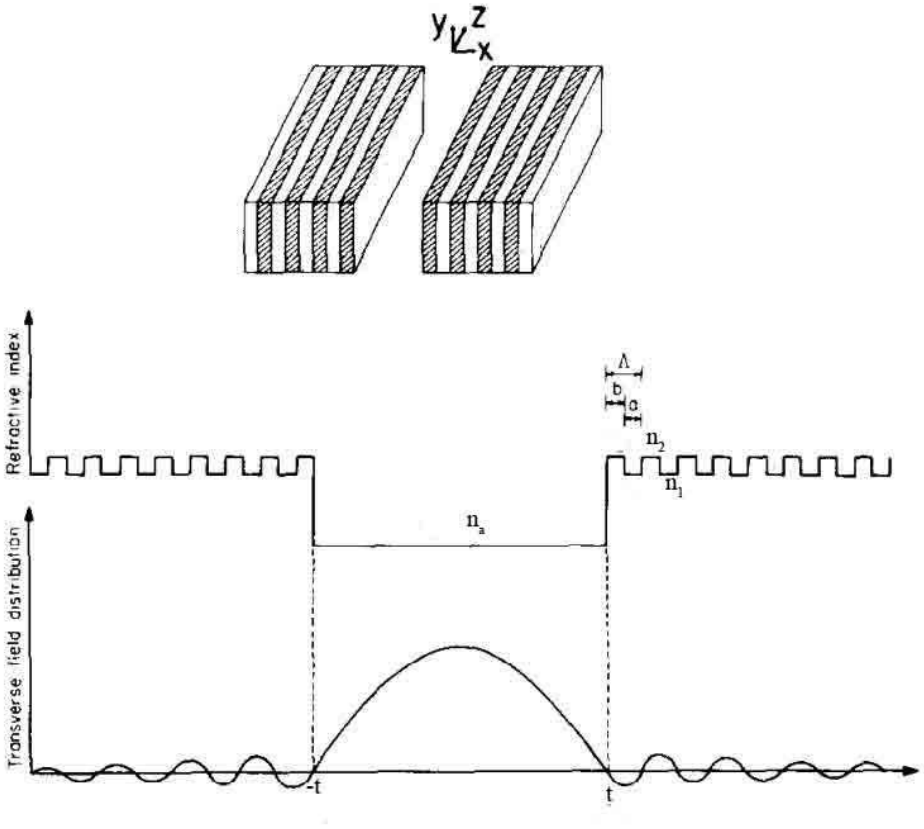

Figure 2.13 - The top figure shows a schematic view of a slab Bragg waveguide. The lower plot shows the transverse field distribution of a Bragg reflection waveguide at a wavelength of 1.15 μm and with $n_a = 1.0$ $n_1 = 2.89$ $n_2 = 3.38$ $\Lambda = .1$ μm $a = b = .5$ Λ $t = .76$ μm [30]

The theoretical basis for Bragg waveguides was developed by Yeh *et al.* in 1976 [30]. They analyzed the wave equation in stratified periodic media and theoretically demonstrated the possibility to obtain lossless confined propagation, even in a low index core layer. The situation is outlined in Fig. 2.13, which depicts a lower index medium such as air surrounded by one dimensional, periodic Bragg cladding mirrors.

One of the key insights of Yeh's paper was that the fundamental mode of the waveguide showed an evanescent decay envelope into the periodic cladding. This occurs when there is complete reflection of the incident wave as it strikes the interface between the guiding medium and the periodic layers. This condition is possible for light wavelengths that lie in the "forbidden gap" of the cladding mirrors. This is identical to the bandgap of the planar reflectors discussed in the previous section. Another important conclusion is that the decay is relatively rapid; therefore, practical structures with a few periods can act as a suitable approximation of the periodic medium.

2.6 Works Cited

[1] L.B. Freund, *Thin Film Materials: Stress, Defect Formation, and Surface Evolution*, Cambridge, [England] ; New York: Cambridge University Press, 2003.

[2] D.W. Hoffman, "Perspective on stresses in magnetron-sputtered thin films," *The 40th National Symposium of the American Vacuum Society*, Orlando, Florida (USA): AVS, 1994, pp. 953-961.

[3] M. Ohring, *Materials Science of Thin Films [electronic Resource]: Deposition and Structure*, San Diego, CA: Academic Press, 2002.

[4] J. Alavarez, "Electron Beam Heating Evaporation," *http://www.icmm.csic.es/fis/english/evaporacion_electrones.html#esquema*.

[5] Rosse, "Bimetallic Mirrors Made by Electro-Deposition," *Nature*, vol. 78, 1908, pp. 366-366.

[6] G. Stoney, "The Tension of Metallic Films Deposited by Electrolysis," *Proc. Roy. Soc.*, vol. A32, 1909, p. 172.

[7] W.D. Nix, "Mechanical properties of thin films," *Metallurgical and Materials Transactions A*, vol. 20, Nov. 1989.

[8] M.F. Doerner and W.D. Nix, "Stresses and deformation processes in thin films on substrates," *Critical Reviews in Solid State and Materials Sciences*, vol. 14, 1988, p. 225.

[9] J.A. Thornton and D. Hoffman, "Stress-related effects in thin films," *Thin Solid Films*, vol. 171, Apr. 1989, pp. 5-31.

[10] P.G. Shewmon, *Transformations in Metals*, Indo American Books, 2007.

[11] S. Sharma and J. Spitz, "Hillock formation, hole growth and agglomeration in thin silver films," *Thin Solid Films*, vol. 65, Feb. 1980, pp. 339-350.
[12] K. Kuwahara, H. Fujiyama, and A. Nishimura, "Adhesion Failure of PVD Films Caused by Repeated Bending of Substrates," *Japanese Journal of Applied Physics*, vol. 20, 1981, pp. L643-L645.
[13] A. Needleman and J. Rice, "Plastic creep flow effects in the diffusive cavitation of grain boundaries," *Acta Metallurgica*, vol. 28, Oct. 1980, pp. 1315-1332.
[14] M.-. Moon, K.-. Lee, K.H. Oh, and J.W. Hutchinson, "Buckle delamination on patterned substrates," *Acta Materialia*, vol. 52, Jun. 2004, pp. 3151-3159.
[15] B. Coterell and Z. Chen, "Buckling and cracking of thin films on compliant substrates under compression," *International Journal of Fracture*, vol. 104, 2000, pp. 169-179.
[16] H. YU and J.W. Hutchinson, "Influence of substrate compliance on buckling delamination of thin films," *International journal of fracture*, vol. 113, 2002, pp. 39-55.
[17] J. W. Hutchinson and Z. SUO, "Mixed mode cracking in layered materials," *Advances in applied mechanics*, vol. 29, 1992, pp. 63-191.
[18] H. Jensen, "Energy release rates and stability of straight-sided, thin-film delaminations," *Acta Metallurgica et Materialia*, vol. 41, Feb. 1993, pp. 601-607.
[19] N.P. Padture, M. Gell, and E.H. Jordan, "Thermal Barrier Coatings for Gas-Turbine Engine Applications," *Science*, vol. 296, Apr. 2002, pp. 280-284.
[20] J.P. McDonald, V.R. Mistry, K.E. Ray, and S.M. Yalisove, "Femtosecond pulsed laser direct write production of nano- and microfluidic channels," *Applied Physics Letters*, vol. 88, 2006, p. 183113.
[21] R.G. DeCorby, N. Ponnampalam, H.T. Nguyen, M.M. Pai, and T.J. Clement, "Guided self-assembly of integrated hollow Bragg waveguides," *Optics Express*, vol. 15, Apr. 2007, pp. 3902-3915.
[22] B. Audoly, "Stability of Straight Delamination Blisters," *Physical Review Letters*, vol. 83, Nov. 1999, p. 4124.
[23] L.D. Landau, L.P. Pitaevskii, E. Lifshitz, and A.M. Kosevich, *Theory of Elasticity, Third Edition: Volume 7*, Butterworth-Heinemann, 1986.
[24] B. Gallas, S. Fisson, E. Charron, A. Brunet-Bruneau, G. Vuye, and J. Rivory, "Making an Omnidirectional Reflector," *Applied Optics*, vol. 40, Oct. 2001, pp. 5056-5063.
[25] J.N. Winn, Y. Fink, S. Fan, and J.D. Joannopoulos, "Omnidirectional reflection from a one-dimensional photonic crystal," *Optics Letters*, vol. 23, Oct. 1998, pp. 1573-1575.
[26] M.H. MacDougal, H. Zhao, P.D. Dapkus, M. Ziari, and W.H. Steier, "Wide-bandwidth distributed Bragg reflectors using oxide/GaAs multilayers," *Electronics Letters*, vol. 30, Jul. 1994, pp. 1147-1149.
[27] K.V. Popov, J.A. Dobrowolski, A.V. Tikhonravov, and B.T. Sullivan, "Broadband high-reflection multilayer coatings at oblique angles of

incidence," *Applied Optics*, vol. 36, Apr. 1997, pp. 2139-2151.
[28] Y. Fink, J.N. Winn, S. Fan, C. Chen, J. Michel, J.D. Joannopoulos, and E.L. Thomas, "A Dielectric Omnidirectional Reflector," *Science*, vol. 282, Nov. 1998, pp. 1679-1682.
[29] R.D. Meade, A.M. Rappe, K.D. Brommer, J.D. Joannopoulos, and O.L. Alerhand, "Accurate theoretical analysis of photonic band-gap materials," *Physical Review B*, vol. 48, 1993, p. 8434.
[30] P. Yeh and A. Yariv, "Bragg reflection waveguides," *Optics Communications*, vol. 19, Dec. 1976, pp. 427-430.

Chapter 3 Thermal Tuning of Hollow Waveguides

3.1 Introduction

As discussed in Chapter 1, one desirable attribute of integrated hollow waveguides is their potential for tunability. Electrostatic and electro-thermal actuation techniques, which are widely employed in MEMS devices, can in principle be used to adjust the air-core dimensions (i.e. mirror spacing) of a hollow waveguide. Small changes in air-core dimensions can result in large changes in the loss and propagation constant of guided modes. This chapter describes the thermal tuning of air-core Bragg waveguides. The waveguides used for these experiments are based on a previously developed process that is illustrated in Fig. 3.1 [1], and which was a precursor and basis for the silicon based waveguides discussed in Chapter 4. The upper cladding mirror of these waveguides is a flexible membrane comprising high thermal expansion materials (chalcogenide glass and polymer), enabling large tuning of the air-core dimensions for small changes in temperature. We applied this mechanism to the thermal tuning of modal cutoff conditions in waveguides with a tapered core profile. Due to the omnidirectional nature of the cladding mirrors, such tapers can be viewed as waveguide-coupled, tunable Fabry-Perot filters.

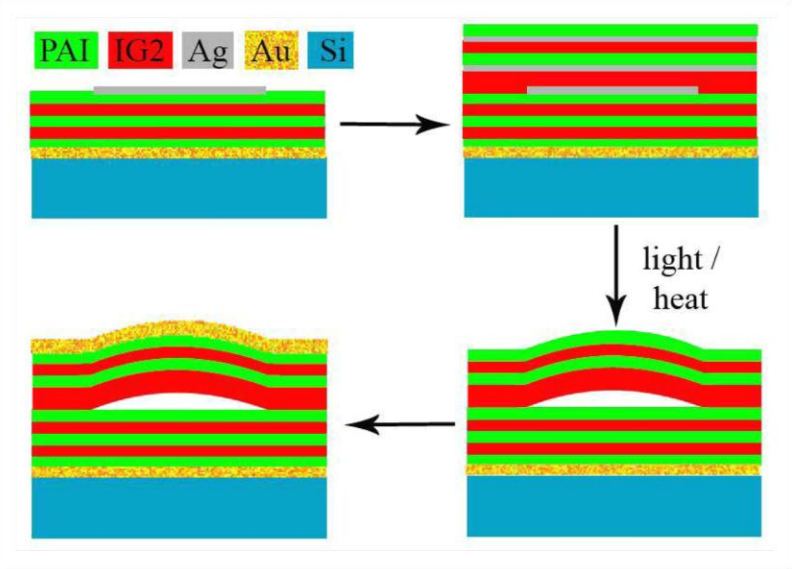

Figure 3.1 - Sequence of steps for producing buckled hollow waveguides and cavities with hybrid metal-dielectric Bragg mirrors.1) A thin Ag layer was patterned on the top (polymer) surface of the bottom hybrid mirror, using a liftoff process. 2) A continuous Ag film was deposited following each IG2 layer in the upper mirror in order to increase the overall compressive stress.3) Light and heat are applied after deposition of the multilayers, to drive the dissolution of Ag into adjacent IG2 films.4)A thin Au layer is deposited on top of the buckled upper mirror to complete the fabrication process.

3.2 Background

Air-core integrated waveguides have been studied as optical interconnects and for applications in sensing [2-4]. They also provide the unique possibility of giant device tuning through micro-mechanical actuation of one of the cladding mirrors [5]. In principle, actuation schemes can be adapted from the extensive literature on tuning of Fabry-Perot filters (with two Bragg mirrors separated by an air cavity) using micro-electro-mechanical systems (MEMS) [6-12]. However, previous experimental work on the tuning of hollow waveguides has mostly relied on external piezoelectric actuators for alignment of separately fabricated upper and lower cladding mirrors [5],[13] . Furthermore, the work has mainly employed

slab waveguides while channel waveguides are preferable or even necessary for many applications [14]. Thus, a desirable goal is the monolithic fabrication of air-core channel waveguides, combined with an integrated actuation mechanism (electrostatic, electro-thermal, etc.).

Air-core filters and waveguides have traditionally been fabricated by surface or bulk micromachining processes, such as sacrificial etching or wafer bonding. Our group recently described [1] an alternative method based on controlled buckling delamination within a multilayer stack. This method produces self-assembled air cavities and channels sandwiched by Bragg reflectors, where the upper cladding mirror is a flexible membrane. Of related interest, tethered [6],[7] clamped [8], and buckled [9] membranes have been widely studied in the context of micro-electro-optical-mechanical systems (MOEMs). Here, we demonstrate tuning of the buckle waveguides through thermal deflection of the upper mirror. This deflection modifies the dimensions of the hollow core, thereby modifying the loss, dispersion and other properties of the guide. As a specific example, we describe thermal tuning of the modal cutoff conditions in a tapered waveguide [15]. These tapered guides are essentially side-coupled Fabry-Perot cavities [16], and in the present context can be viewed as a new geometry for the implementation of tunable optical filters.

3.3 Thermo-Mechanical Analysis

The self-assembly fabrication process used to produce the air-core structures is discussed in detail elsewhere [1]. The cladding mirrors are gold-terminated Bragg

reflectors, in turn comprising low index polyamide-imide (PAI) layers and high index $Ge_{33}As_{12}Se_{55}$ (IG2 chalcogenide glass) layers. The upper and lower mirrors possess an overlapping band of omnidirectional reflection in the 1450-1650 nm range [15]. The buckled regions are defined by creating areas of low adhesion, through patterning of an embedded Ag layer and use of the photodoping phenomenon [1]. Buckle formation is driven by a controlled amount of net compressive stress in the upper cladding mirror, such that straight-sided (Euler) delamination buckles are formed within a desired range of feature sizes.

Within the limits of elastic deformation, the peak height of a straight-sided delamination buckle (the Euler buckle) is given by [17]:

$$\delta = h\sqrt{\frac{4}{3}\left(\frac{\sigma_0}{\sigma_C}-1\right)} = h\sqrt{\frac{4}{3}\left(\left(\frac{b}{b_{\min}}\right)^2-1\right)} \approx \frac{2hb}{\sqrt{3}b_{\min}}, \qquad 3.1$$

where h and σ_0 are the thickness and intrinsic stress, respectively, of the buckled film or multilayer, b is the half-width of the buckle (see Fig. 3.2), b_{min} is the minimum half-width for the onset of buckling (given h and σ_0), and σ_C is the critical compressive stress for the onset of buckling (given h and b):

$$\sigma_C = \frac{\pi^2}{12}\frac{Y}{\left(1-\nu^2\right)}\frac{h^2}{b^2}, \qquad 3.2$$

Here, Y and ν are the Young's modulus and Poisson's ratio of the film (or effective medium values for a buckled multilayer). Note that the approximation in Eq. 3.1 is restricted to the range $b>>b_{min}$.

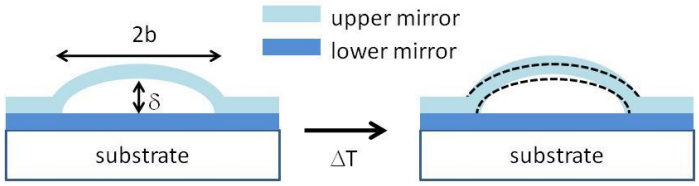

Figure 3.2 - Shown is a schematic illustration of the change in height of a buckled hollow waveguide (end facet view) driven by an increase in temperature. A positive temperature change increases the compressive stress in the upper mirror, since it comprises materials with higher thermal expansion coefficient than the underlying silicon substrate. The added compressive stress results in a slight change in shape and increased peak height for the buckle.

Consider a pre-existing delamination buckle subject to a change in temperature. Due to thermal expansion mismatch between the film and substrate, the change in temperature modifies the biaxial compressive stress of the buckled feature according to [18]:

$$\Delta\sigma = \frac{Y}{(1-\nu)}\Delta\alpha\,\Delta T \ , \qquad 3.3$$

where $\Delta\alpha$ is the difference in coefficient of thermal expansion (CTE) between the film and substrate and ΔT is the change in temperature. Furthermore, the change in stress modifies the peak buckle height. We can approximate this from 3.1 as follows:

$$(\delta+\Delta\delta)^2 = \frac{4h^2}{3}\left[\frac{(\sigma_0+\Delta\sigma)}{\sigma_C}-1\right] , \qquad 3.4$$

which reduces to:

$$\Delta\delta \approx \frac{2h^2}{3\delta}\frac{\Delta\sigma}{\sigma_C} \ , \qquad 3.5$$

Combining equations 3.2, 3.3, and 3.5, an expression for the change in height with temperature is obtained:

$$\frac{\Delta\delta}{\Delta T} = \frac{8}{\pi^2}\frac{\left(1-\nu^2\right)}{\left(1-\nu\right)}\frac{b^2}{\delta}\Delta\alpha \quad , \qquad 3.6$$

Note that since δ is approximately proportional to b (provided $b>>b_{min}$, see Eq. 3.1), it follows that the change in buckle height with temperature is approximately proportional to the starting buckle height.

To analyze buckling of a thin-film stack, an effective medium approach can be used [17] [17]. For the present case, the buckled upper mirror comprises ~61 % PAI polymer, ~37 % IG2 glass, and ~2 % Au. Using the known mechanical properties of these materials [19], the effective medium parameters are as follows: Young's modulus E~11 GPa, Poisson's coefficient ν~0.3, and CTE mismatch with silicon subsrate $\Delta\alpha$~20x10^{-6} K^{-1}. Given these values, the predictions of Eq. 3.6 are in good agreement with experimental results as shown below.

3.4 Experimental Results and Analysis

In initial experiments, samples were placed on a thermo-electric temperature controller and an optical profilometer (Zygo) was used to measure the height change. Fig. 3.3 shows a typical result for a straight-sided buckle waveguide with base width 2b ~60 μm and peak height δ~3.4 μm. Using these dimensions and the effective medium parameters cited above, Eq. 3.6 predicts ($\Delta\delta/\Delta T$) ~5.6 nm/K. As shown in Fig. 3.3(b), this estimate is in good agreement with the experimental data.

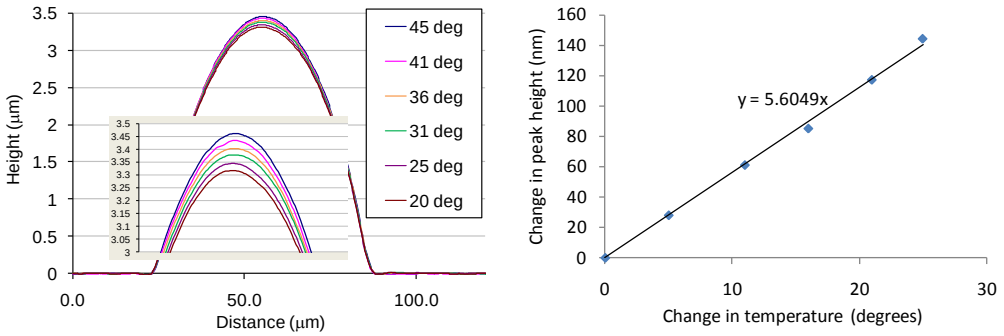

(a) (b)

Figure 3.3 - (a) Optical profilometer scans for a buckled waveguide with 60 μm base width, at a series of fixed temperatures. The inset plot shows the top of the curves in greater detail. (b) Plot of the measured change in peak height versus change in temperature. The straight line is a linear fit to the data.

Such changes in core height can produce significant changes in the properties of a leaky guided mode. To illustrate, we describe the tuning of the mode cutoff position in waveguides with a tapered core profile. In these tapered guides [15], out-of-plane coupling at mode cutoff arises due to the omnidirectional nature of the cladding mirrors. As shown schematically in Fig. 3.4(a), these guides can thus be viewed as side-coupled Fabry-Perot cavities [16]. From a slab waveguide model $\delta_m \sim \delta_{m-1} + \lambda_0/2$, where δ_m is the cutoff height for mode order $m=0,1,2\ldots$, and λ_0 is the free-space wavelength. For an increase in temperature, the increase in core height causes the cutoff point for each mode to shift towards the smaller end of the taper.

The microscope images in Fig. 3.4(b) show the out-coupling positions of 5 vertical mode orders at a wavelength of 1550 nm, for a waveguide with width ($2b$) tapered from 80 to 10 μm over a distance of 5 mm (i.e. $\Delta b/\Delta z$ is ~7 μm/mm). For a purely elastic deformation and for $b >> b_{min}$,, Eq. 3.1 predicts that the peak buckle

height will also exhibit a linear profile. The approximately equal spacing of the cutoff positions for the m=2 to 5 modes confirms an approximately constant slope (i.e. since the difference in core height between adjacent orders at cutoff is ~$\lambda_0/2$). However, within our process the buckle formation is influenced by both elastic and plastic deformation [15]. The larger spacing between the m=2 and m=1 spots indicates a lower slope at the small end of the taper. Also note that, due to the particular mirror design used [15], the fundamental (m=0) vertical mode order does not exhibit cutoff.

Using a slab model for the waveguides, the shift in out-coupling point with temperature can be estimated as follows:

$$\frac{\Delta z}{\Delta T} \approx \frac{\Delta z}{\Delta \delta}\frac{\Delta \delta}{\Delta T} = \frac{1}{S_T}\frac{\Delta \delta}{\Delta T} \quad , \tag{3.7}$$

where S_T is the taper slope. From profilometer measurements and the spacing of cutoff points, we estimated S_T~1.1-1.3 μm/mm for the main portion of the taper (i.e. for the m=2 to m=5 mode orders, as discussed above) and S_T~0.8 μm/mm near the narrow end of the taper (i.e. for the m=1 mode order).

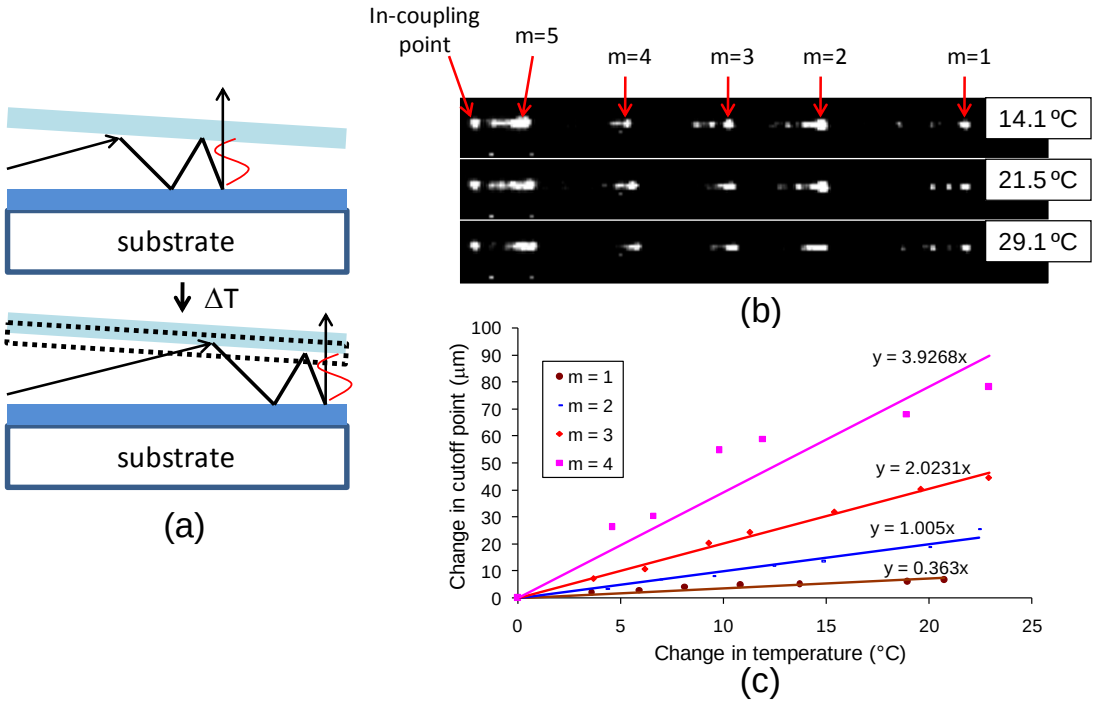

Figure 3.4 - (a) Cross-sectional schematic of a tapered air-core waveguide with omnidirectional claddings, near a mode cutoff point. The black arrows depict the ray-optics model of vertical radiation at cutoff, and the red curve represents the vertical field profile (m=1 case shown) at the cutoff point. An increase in core height due to increase in temperature causes a positional shift of the cutoff point. (b) Images captured by an infrared camera via a microscope, showing the shift in the m=1 to 5 cutoff positions with temperature, for a wavelength of 1550 nm. (c) The experimental shift in out-coupling position plotted versus change in temperature, for mode orders 1 to 4. The straight lines are linear fits to the data.

Assuming a fixed slope, and since $\Delta\delta \sim \delta$ as discussed in Section 2, Equations 3.6 and 3.7 predict that the shift in out-coupling position scales with the mode order. This is corroborated by the data plotted in Fig. 3.4(c). For m=4 (3), δ~2.7 (2.0) μm, $2b$~48 (32) μm and S_T~1.2 (1.3) μm/mm were estimated, so that Equations 3.6 and 3.7 produce $\Delta z/\Delta T$ ~3.8 (2.1) μm/K, in good agreement with experimental observations. However, the theory was found to slightly overestimate the positional shift for the lower mode orders, possibly due to the neglect of plastic deformation in the derivation of Eq. 3.6.

These tapers could be used as a new type of tunable Fabry-Perot filter, by extracting the vertically radiated light from a fixed position and varying the temperature. The wavelength shift can be approximated as follows:

$$\frac{\Delta\lambda_0}{\Delta T} \approx \frac{\Delta\lambda_0}{\Delta z}\frac{\Delta z}{\Delta T} = \frac{1}{D_T}\frac{\Delta z}{\Delta T} \ , \qquad 3.8$$

where $D_T = \Delta z/\Delta\lambda_0$ is the spatial dispersion provided by the taper. Neglecting the wavelength-dependent penetration depth of the cladding mirrors, $D_T \sim (m+1)/(2S_T)$. Since both D_T and $\Delta z/\Delta T$ scale approximately with mode order (m+1), the wavelength shift per unit temperature change is expected to be approximately the same for all vertical mode orders. The upper limit on tuning range is set either by the free spectral range (*FSR*) between mode orders or by the omnidirectional bandwidth of the cladding mirrors. For the low mode orders employed here, $FSR \sim \lambda_m/(m+2)$, where λ_m is the resonant wavelength. Thus, both the *FSR* and omnidirectional cladding bandwidth are on the order of several hundred nm. Practical limitations on tuning range include the maximum temperature variation that can be induced and the thermal stability range of the cladding materials, which is >300 °C for the present case [19] .

Spectral line-width is another important parameter for an optical filter. As discussed in detail elsewhere [20], the line-width for the cutoff-based out-coupling mechanism depends on several factors, including the spatial dispersion of the taper, the presence of multiple lateral modes within each vertical mode family, and modal back-reflection and standing-wave formation near the cutoff

point. However, it is possible to minimize the multimode and standing wave effects by use of appropriate input and output coupling optics [20]. In that case, line-width can be estimated using a vertical Fabry-Perot model to describe the out-coupling mechanism:

$$\Delta\lambda_{FWHM} \approx \frac{z_P}{D_T} + \frac{\lambda_0}{(m+1)\pi\left(\frac{\sqrt{R}}{1-R}\right)}, \qquad 3.9$$

where z_P is the length of taper from which light is collected and R is the normal-incidence reflectance of the cladding mirrors (assumed equal).

To test these predictions, light from a tunable laser (Santec) was input to a tapered hollow waveguide via a polarization controller and a tapered (lensed) optical fiber (Oz Optics, nominal spot size ~3 μm), enabling preferential coupling of the fundamental lateral modes. The results below are for TE polarization, since the TM modes exhibit somewhat higher loss [14]. However, it is important to note that the cutoff-based coupling mechanism is nearly independent of polarization since TE and TM modes become degenerate at cutoff [15],[20]. This implies the potential for a polarization-independent tunable filter, provided the polarization-dependent loss (PDL) of the waveguides is minimized.

The out-coupled light was collected by a cleaved single-mode fiber (Corning SMF-28, NA~0.13) placed in close proximity to the tapered waveguide surface, and delivered to a calibrated photodetector. The pick-up fiber was kept at a fixed position, and wavelength scans were obtained for a series of fixed temperatures. This collection setup implies that z_P~9 μm, i.e. the effective collection length is

approximately the core diameter of the pickup fiber. As explained in detail elsewhere [20], the use of a low NA pickup fiber reduces the impact of satellite peaks on the short wavelength side of the main spectral feature. Fig. 3.5(a) shows typical results for the m=2 mode, with the output spectrum exhibiting a temperature-dependent pass-band. From measurements with a tunable laser [15], we estimated $(1/D_T)$~450 nm/mm for the m=2 mode near 1550 nm. Thus, with z_P~9 μm and R~0.997 [15][15], Eq. 3.9 predicts $\Delta\lambda_{FWHM}$~4.5 nm, in good agreement with the results of Fig. 3.5(a). Note that higher mode orders produce narrower pass-bands, as described in detail elsewhere [20]. Using the same value for taper dispersion and the experimentally determined out-coupling shift for the m=2 mode ($\Delta z/\Delta T$~1 μm/K, see Fig. 3.4(c)), Eq. 3.8 predicts $\Delta\lambda_0/\Delta T$~0.45 nm/K, in good agreement with the results of Fig.3.5(b). Both the line-width and the insertion loss (see below) were found to be approximately independent of temperature.

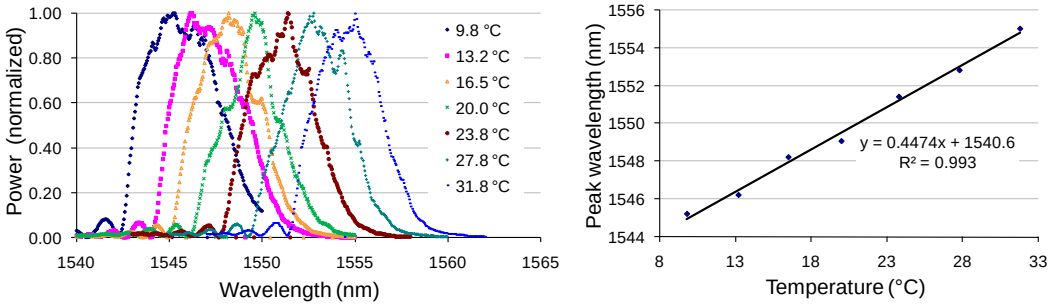

(a) (b)

Figure 3.5 - (a) Spectral scans obtained at a fixed out-coupling point corresponding to the m=2 mode, for a series of fixed temperatures. (b) Plot of peak out-coupling wavelength versus temperature, revealing a wavelength shift of ~0.45 nm/°C.

The demonstrated tuning range (~10 nm) was limited by the experimental setup, which employed an external thermo-electric stage for temperature variation. Integration of thermal actuators is expected to enable a much wider tuning range. Interesting comparisons can be made with tunable filters based on hollow waveguides with a Bragg reflector defined on one of the cladding mirrors [12-14]. A tuning range of ~150 nm was recently reported [14], but requiring a core thickness variation (controlled by external piezoelectric actuators) in the 5 to 10 μm range. A much smaller tuning range (2.6 nm) was reported for a similar device driven by an integrated thermal actuator [12]. Since MEMS actuators typically have restricted range of motion, a reasonable figure of merit for tunable hollow waveguide filters is the wavelength shift per unit change in core height ($\Delta\lambda_0/\Delta\delta$). Using a hard mirror approximation for the Fabry-Perot, $\Delta\lambda_0/\Delta\delta$ =2/(m+1), or 667 nm/μm for the m=2 case. From the results above, the actual value is somewhat lower (~450 nm/μm), but still more than an order of magnitude higher than for the device reported in reference [14] (~30 nm/μm).

Finally, note that the measured insertion loss was approximately 30 dB, and is mainly caused by the use of a fairly opaque (~50 nm thick) outer Au layer on the cladding mirrors [1]. With the use of all-dielectric mirrors, optimized taper geometry, and improved coupling optics, it should be possible to reduce this loss by more than 2 orders of magnitude [20].

3.5 Works Cited

[1] N. Ponnampalam and R.G. Decorby, "Self-assembled hollow waveguides with hybrid metal-dielectric Bragg claddings," *Optics Express*, vol. 15,

2007, p. 12595.
[2] E.J. Lunt, P. Measor, B.S. Phillips, S. Kohn, H. Schmidt, and A.R. Hawkins, "Improving solid to hollow core transmission for integrated ARROW waveguides," *Optics Express*, vol. 16, Dec. 2008, pp. 20981-20986.
[3] Y. Zhou, V. Karagodsky, B. Pesala, F.G. Sedgwick, and C.J. Chang-Hasnain, "A novel ultra-low loss hollow-core waveguide using subwavelength high-contrast gratings," *Optics Express*, vol. 17, Feb. 2009, pp. 1508-1517.
[4] H. Chiu, F. Hsiao, C. Chan, and C. Chen, "Compact and low-loss bent hollow waveguides with distributed Bragg reflector," *Optics Express*, vol. 16, 2008, pp. 15069-15073.
[5] F. Koyama, T. Miura, and Y. Sakurai, "Tunable hollow optical waveguides and their applications for photonic integrated circuits," *Electronics and Communications in Japan (Part II: Electronics)*, vol. 89, 2006, pp. 9-19.
[6] A. Tran, Y. Lo, Z. Zhu, D. Haronian, and E. Mozdy, "Surface micromachined Fabry-Perot tunable filter," *IEEE Photonics Technology Letters*, vol. 8, 1996, pp. 393-395.
[7] P. Tayebati, P. Wang, M. Azimi, L. Maflah, and D. Vakhshoori, "Microelectromechanical tunable filter with stable half symmetric cavity," *Electronics Letters*, vol. 34, Oct. 1998, pp. 1967-1968.
[8] Y. Yi, P. Bermel, K. Wada, X. Duan, J.D. Joannopoulos, and L.C. Kimerling, "Tunable multichannel optical filter based on silicon photonic band gap materials actuation," *Applied Physics Letters*, vol. 81, 2002, p. 4112.
[9] H. Halbritter, M. Aziz, F. Riemenschneider, and P. Meissner, "Electrothermally tunable two-chip optical filter with very low-cost and simple concept," *Electronics Letters*, vol. 38, 2002, p. 1201.
[10] S. Irmer, J. Daleiden, V. Rangelov, C. Prott, F. Romer, M. Strassner, A. Tarraf, and H. Hillmer, "Ultralow biased widely continuously tunable fabry-perot filter," *IEEE Photonics Technology Letters*, vol. 15, 2003, pp. 434-436.
[11] C.F. Mateus, M.C. Huang, and C.J. Chang-Hasnain, "Micromechanical tunable optical filters: general design rules for wavelengths from near-IR up to 10 [mu]m," *Sensors and Actuators A: Physical*, vol. 119, Mar. 2005, pp. 57-62.
[12] Y. Sakurai, H. Yamakawa, Y. Yokota, A. Matsutani, T. Sakaguchi, and F. Koyama, "Hollow waveguide distributed Bragg reflector for widely tunable optical devices," *Optical Fiber Communication Conference, 2006 and the 2006 National Fiber Optic Engineers Conference. OFC 2006*, 2006, pp. 3 pp.-.
[13] Y. Sakurai and F. Koyama, "Tunable hollow waveguide distributed Bragg reflectors with variable air core," *Optics Express*, vol. 12, Jun. 2004, pp. 2851-2856.
[14] M. Kumar, T. Sakaguchi, and F. Koyama, "Wide tunability and ultralarge birefringence with 3D hollow waveguide Bragg reflector," *Optics Letters*, vol. 34, Apr. 2009, pp. 1252-1254.
[15] N. Ponnampalam and R.G. DeCorby, "Out-of-plane coupling at mode cutoff

in tapered hollow waveguides with omnidirectional reflector claddings," *Optics Express*, vol. 16, Mar. 2008, pp. 2894-2908.
[16] M.L. Povinelli, M. Ibanescu, S.G. Johnson, and J.D. Joannopoulos, "Slow-light enhancement of radiation pressure in an omnidirectional-reflector waveguide," *Applied Physics Letters*, vol. 85, 2004, p. 1466.
[17] M.-. Moon, K.-. Lee, K.H. Oh, and J.W. Hutchinson, "Buckle delamination on patterned substrates," *Acta Materialia*, vol. 52, Jun. 2004, pp. 3151-3159.
[18] S.R. Choi, J.W. Hutchinson, and A.G. Evans, "Delamination of multilayer thermal barrier coatings," *Mechanics of Materials*, vol. 31, Jul. 1999, pp. 431-447.
[19] R.G. DeCorby, N. Ponnampalam, H. Nguyen, and T. Clement, "Robust and Flexible Free-Standing All-Dielectric Omnidirectional Reflectors," *Advanced Materials*, vol. 19, 2007, pp. 193-196.
[20] R. DeCorby, N. Ponnampalam, E. Epp, T. Allen, and J. McMullin, "Chip-scale spectrometry based on tapered hollow Bragg waveguides," *Optics Express*, vol. 17, 2009, pp. 16632-16645.

Chapter 4 Development of Experimental Processes

4.1 Introduction

The concept that light can be guided along a low index channel surrounded by Bragg cladding mirrors was the guiding principle in the development of the waveguides discussed in this chapter. Here, the experimental process used to produce the waveguides is described, in contrast to the theoretical principles that were introduced in Chapter 2. Amongst alternative materials, Bragg reflection waveguides utilizing silicon and its oxide are desired for many reasons. Aside from its importance and heavy usage in the semi-conductor industry, the optical properties of silicon are very well suited for the creation of a dielectric Bragg reflector at wavelengths beyond 1000 nm. For omnidirectional reflectors designed for air incidence it has been shown [1] that the optimal refractive index for the low index layers (in terms of minimizing the required index of the high index layers for a given omnidirectional bandwidth) is approximately 1.5. Fortuitously, the index of SiO_2 is very similar to this in the visible and near infrared region. Many different materials have been used for the high index layer including metal-oxides such as TiO_2 [2], polycrystalline silicon [3], and amorphous silicon (a-Si). The Si/SiO_2 combination has been the most popular choice of materials used for integrated hollow waveguides fabricated using traditional methods such as sacrificial etching and wafer bonding [4],[5]. In the present work, a four period

omnidirectional Bragg reflector is sputter deposited using an a-Si/SiO_2 combination, and these mirrors form the upper and lower cladding of a hollow waveguide. The air core is formed by taking advantage of the intrinsic stress, created during the deposition of the Bragg mirror, to induce buckling along a low adhesion patterned fluorocarbon layer. The experimental process is presented schematically in Fig. 4.1, and the present chapter will detail its development.

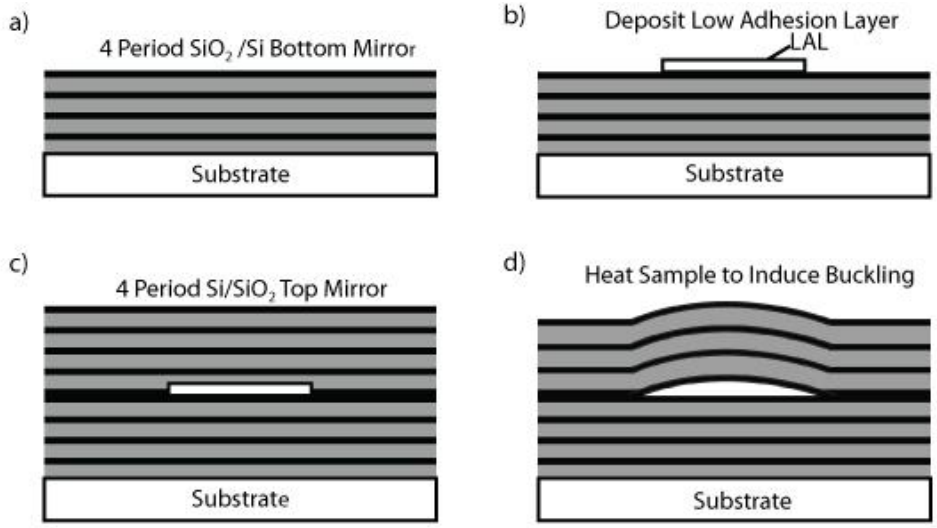

Figure 4.1 - An overview of the process flow used to create the hollow Bragg waveguides.

4.2 Development of Si/SiO_2 Bragg Mirrors

The requirements for the Bragg reflector to be used in the project revolved around both their optical properties and the ability to control the stress of the layers. Given that the initial target wavelength of the waveguides was 1550 nm, the optical properties of the materials (such as absorption and index of refraction) were investigated in that range. Tunability of the stress was critical for the controlled formation of straight-sided delamination buckles. The low index layer

chosen for this project was SiO_2 while a-Si was chosen for the high index layer. This decision to use a-Si was made for several reasons including:

- Its high index at 1550 nm (~3.5) allows for a large omnidirectional bandgap.
- It can be deposited at a relatively low temperature(~150°C), using electron beam deposition or sputtering.
- An a-Si/SiO_2 multilayer can be deposited without breaking vacuum by using multiple sources and reactive sputtering, which results in fewer defects and a cleaner sample.
- a-Si has low loss in the 1550 nm wavelength range of interest.

As detailed in the following sub-sections, both sputtering and e-beam evaporation techniques were studied for the deposition of a-Si/SiO_2 multilayers. The sputtered multilayers were found to have superior properties (lower optical loss and higher compressive stress) for the buckling self-assembly process and were used in the subsequent fabrication of hollow waveguides as detailed in Chapter 5.

4.2.1 Pulsed Magnetron Sputtering Setup

In initial work, a sputtering system was chosen as a deposition technique because it is widely reported to enable a large degree of control over the resultant stress [6]. The system used is a commercial magnetron sputtering chamber (Kurt J. Lesker), housed in a class 10,000 clean room at the University of Alberta's Nanofabrication facility. The system has capability for reactive sputtering with oxygen and several other gases. In order to accommodate multilayer films, three

targets can be loaded simultaneously into three different sputter guns arranged symmetrically near the center of the chamber. Each target has a separate power supply and shutter, allowing for deposition of any combination of the three materials at the same time. The chamber is connected to two pumps. The mechanical roughing pump works from atmosphere to approximately 300 mTorr at which point a cryo pump is connected. The cryo pump evacuates the system to the 10^{-6} Torr range in approximately one hour, the exact time depending on the chamber conditions. Pressure is monitored using a combination of three gauges: ion, baratron and convectron.

The sputtering system uses both DC magnetron and pulsed magnetron power supplies. DC power supplies were the first type developed for sputtering and are the most basic. As depicted in Fig. 4.2, the target (deposition material) acts as a cathode and is negatively biased by the power supply (Advanced Energy MDX 500). The substrate acts as anode and, in the setup described, is simply grounded. However, in some sputtering systems a bias is applied to the substrate. To increase the deposition rate, and raise the operating pressure, the three sputtering guns use magnetic fields to confine the plasma. The combination of bar magnets encircling the back of the target with a strong central magnet causes the electrons to move in a "racetrack" or circular pattern [7]. This creates a plasma that is concentrated around the racetrack and, consequently, the target erodes in that fashion. This confined plasma results in more efficient sputtering by reducing the gas phase collisions of the sputtered atoms [8].

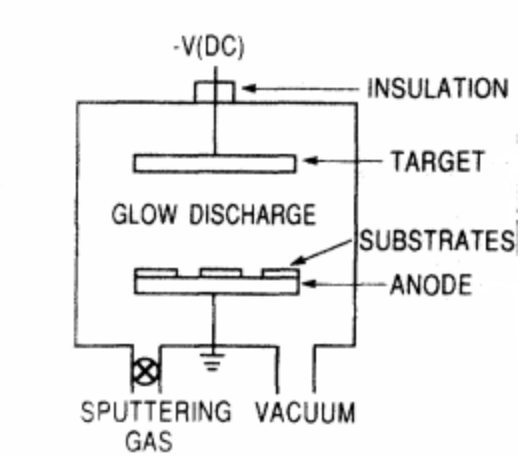

Figure 4.2 – The basic components of a DC powered sputtering chamber, adapted from [8].

A pulsed magnetron power supply increases the sputtering options by allowing highly insulating layers to be deposited at a consistent rate and quality [7]. Pulsed power supplies are often preferred over DC supplies, as explained in the following.. Often, targets can become “poisoned” [8], in the sense that the surface composition is more insulating than the bulk material. This is typically caused by reactive gases that result in formation of an oxide on the target, which in turn is prone to increased charging [8]. This surface layer reduces secondary electron emission from ion bombardment and eventually results in a positive surface charge. With sufficient charge build up, local dielectric breakdown of the insulating film causes arcing between the target surface and the metals of the sputtering gun [8]. This arcing can erode the target, causing cratering and ejection of liquid droplets which affect the quality of the film [8]. This problem can be addressed by incorporating a pulsed power supply [7], which allows the positive surface charge to be discharged. The user designates a time period on each cycle

during which the target is not biased. A standard pulsed power supply is shown schematically in Fig. 4.3.

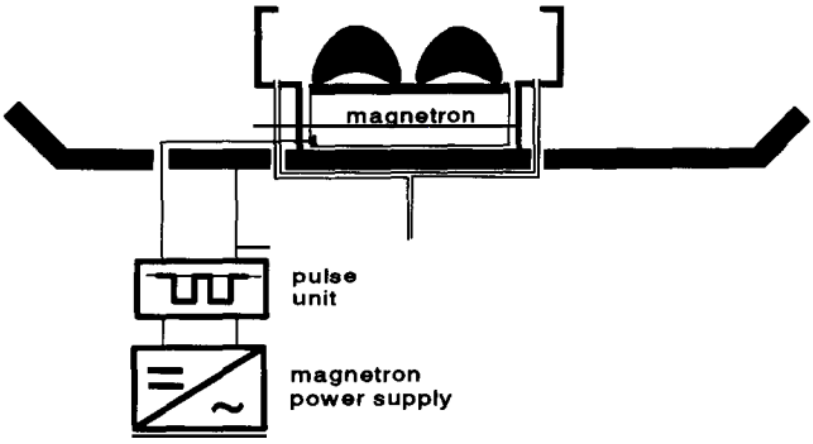

Figure 4.3 - A schematic of a typical pulsed magnetron power supply. The pulse unit introduces an off interval to allow the target to discharge once every cycle. The figure is adapted from [7].

The system used in this project allowed square or sinusoidal voltage pulses, with rates up to several hundred kHz. The magnitude and duration of the pulses can be adjusted using the control unit (Advanced Energy DC Pinnacle Plus) which is displayed in Fig. 4.4. A tungsten element is attached to the substrate holder to enable heating which can cause the properties of the deposited film to vary significantly as described in Chapter 2 (see Sec. 2.3).

Figure 4.4 –The three power supplies connected to the sputtering system. The top two are DC magnetron sources while the bottom is a pulsed magnetron setup.

4.2.2 Sputter Deposition of a Bragg Mirror

The process used to create the a-Si/SiO_2 Bragg mirrors started with a bare, single-side polished (100) silicon wafer. To remove contamination, wafers were dipped for twenty minutes into a freshly prepared piranha solution (3:1 mixture of sulphuric acid and hydrogen peroxide, respectively). The Wafers were then rinsed with deionized (DI) water and spin dried prior to being loaded into the sputtering chamber. Of the three sputter guns in the system, the first two are identical (Gun1, Gun2). The third gun has a slightly altered configuration; the magnets are stronger and the dark space shield and mounting hardware is slightly different, which is evident in the layout shown in Fig. 4.5.

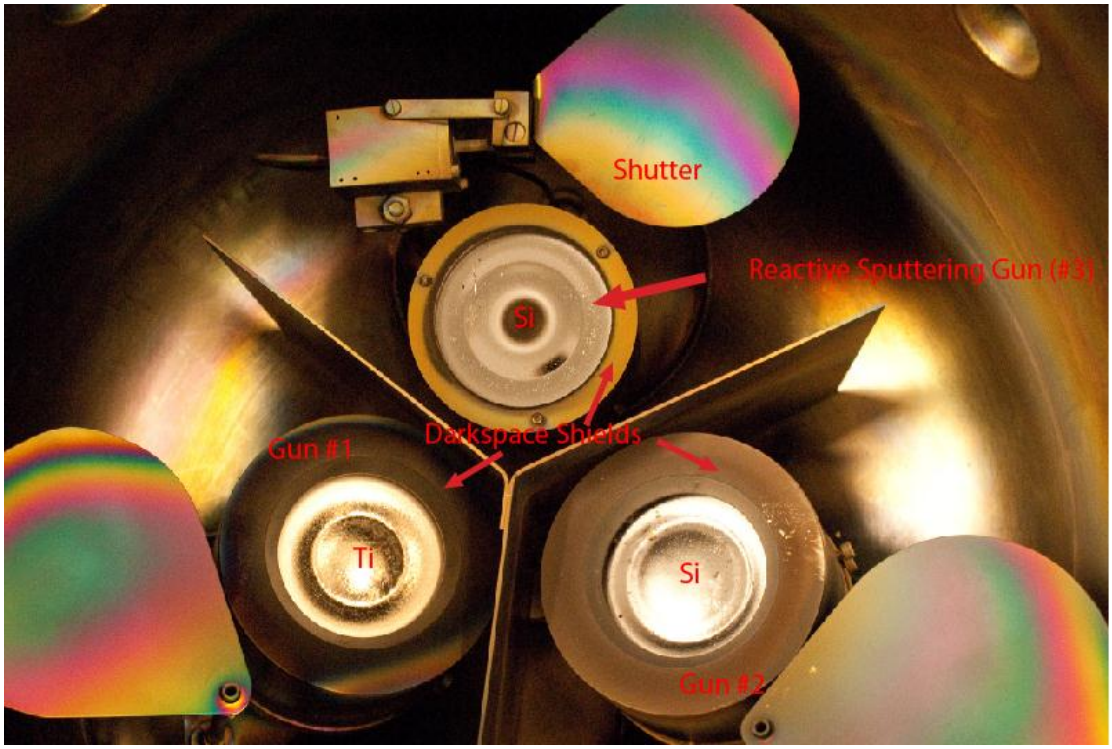

Figure 4.5 – A view inside the sputtering chamber showing the orientation of the sputter guns and dark space shields.

The procedure for depositing the Bragg multilayer used all three guns. Two of the guns were mounted with identical, 3 inch diameter silicon targets, for deposition of the SiO_2 and silicon layers respectively. The use of separate targets helps minimize contamination of the a-Si layers by oxygen, and also reduces the deposition time. If a single target were used, it would be necessary to "burn in" the target prior to the deposition of each a-Si layer due to the oxide layer that forms during deposition of the SiO_2 layers. The last gun is loaded with a 3 inch titanium target, which is used as a getter of residual oxygen during deposition of the a-Si layers. The gun is operated at low power (50 W) and the shutter is never opened. This target captures residual oxygen in the system, as the oxygen gas

reacts with the sputtered titanium to form an oxide [9] on that gun's shutter and surrounding hardware. In order to streamline the process and minimize the possibility of failed deposition runs, n-type silicon targets were used. The use of n-type targets allows testing with an ohm-meter, to ensure an open circuit between the target and chamber. In initial work with undoped silicon targets, problems had arisen because of conduction between the dark space shield and the target. This can cause arcing and often the plasma would simply not light. An added difficulty was that this shorting problem would not be evident until after the system was pumped down. Testing with the ohm-meter virtually eliminates this problem, because the target can be checked to insure it is insulated from the rest of the chamber before the system is closed.

After all the targets and substrates are loaded, the system is pumped down using the mechanical roughing pump to ~300 mTorr. The cryo pump (Kurt J. Lesker) is connected and the system is further evacuated. When the desired base pressure is reached, the tungsten-element substrate heater is ramped up at 10 °C/min until the desired substrate temperature (typically 150 °C) is reached. The heating causes outgassing, and the chamber pressure rises to ~4 $x10^{-6}$ Torr. Before commencing with the deposition, the system is left to stabilize until the pressure recedes back down to ~2 x 10^{-6} Torr, a process which takes approximately 15 minutes. The working gas of the system (argon) is then injected at a flow rate of 50 sccm while concurrently reducing the aperture of the cryo pump valve until the chamber pressure reaches 7 mTorr. For the bottom cladding of the waveguide described in Chapter 5, SiO_2 is the initial layer. The pulsed power supply is

hooked to gun 3 and the plasma is struck with the shutter closed. The shutter is kept closed for five minutes to facilitate a plasma clean on the surface layers of the target. During this period the pressure is lowered to 3.5 mTorr since this was found to increase the following: The negative bias on the target, the deposition rate, and the amount of compressive stress in the multilayers. Although compressive stress is not critical in the bottom cladding Bragg reflector of the waveguide, the same deposition parameters were used for both the bottom and top cladding mirrors, in order to maximize the symmetry of the waveguide.

The deposition rate of the films was found to vary somewhat depending on the chamber conditions. This is a difficulty often associated with multiuser systems that exist in shared nanofabrication facilities. The main cause of variation is thought to be the deposition of different materials by other users. This alters the electric field in the plasma and thus the deposition rates. Typical deposition conditions and flow rates are summarized in Table 4.1.

Target	Power (W)	Bias (V)	Pressure (mTorr)	O_2 (sccm)	Dep. Rate (nm/min)	Index
a-Si	200	~365	3.5	0	9.22	3.41
SiO_2	200	~530	3.5	2.5	17.25	1.46
Ti	50	~52	variable	0		
Pulse Freq. = 150 kHz		T = .5 µs	Ar Flow = 50 sccm			
Base Pressure = ~ 1 * E 10-6 Torr			Pump Down = ~1 hour			

Table 4.1 - The deposition conditions of the sputtering system used for the upper and lower Bragg reflectors.

To increase deposition consistency, the dark space shields can be cleaned using metal scouring pads to remove residual dielectric material before each deposition. Once the deposition is complete, all gas flows and the power to the substrate heater are shut off, and the system is vented until atmospheric pressure is reached. The system is left for approximately 15 minutes until the sample is sufficiently cool for manual removal. The entire deposition run for a four period Bragg reflector takes around five hours, and can be slightly longer in some cases depending on the chamber conditions.

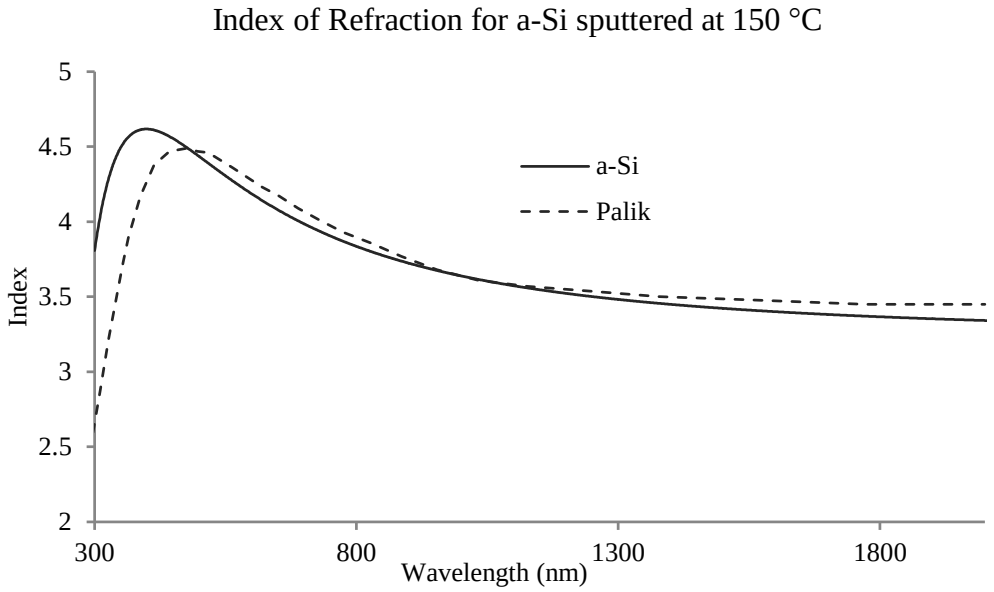

Figure 4.6 - Index of refraction for sputtered a-Si extracted from single film reflection measurements using an ellipsometer; this is compared against the values given for a-Si by Palik *et al*. in ref [10].

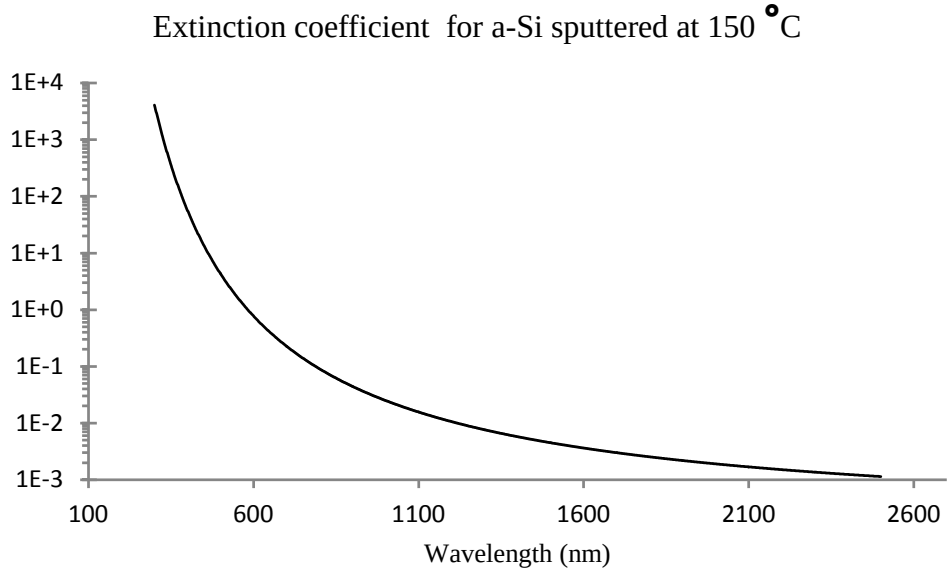

Figure 4.7 - The extracted value of the extinction coefficient for sputtered a-Si at 150 °C. It was determined using VASE data from a 1 period sample of a-Si and SiO_2.

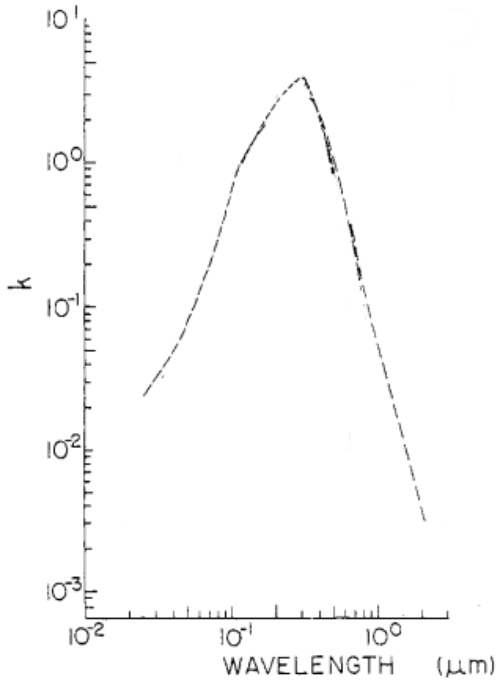

Figure 4.8 - Extinction coefficient of a-Si from Ref. [10].

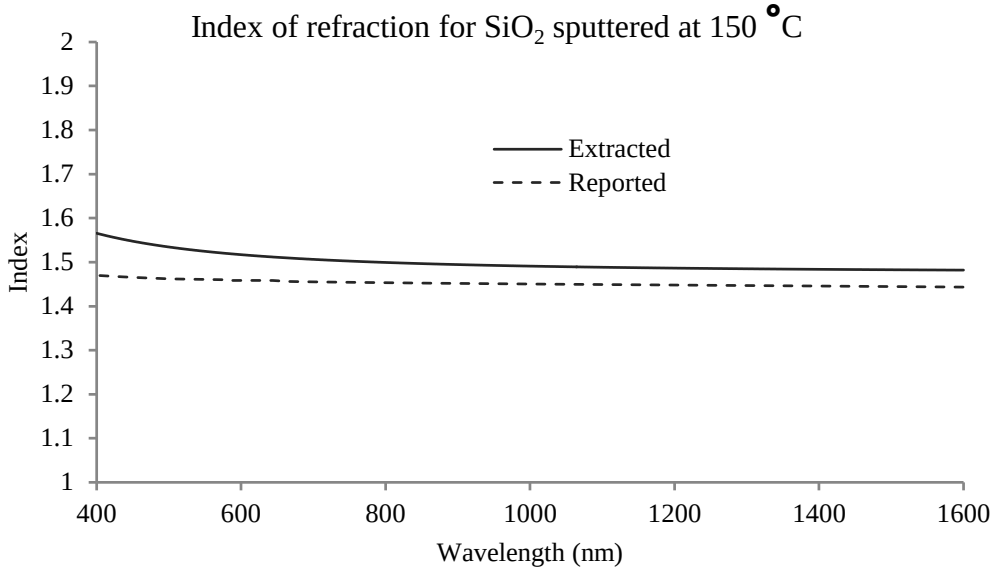

Figure 4.9 - The index of refraction for sputtered SiO_2 extracted from a multilayer plot. This is compared against the reported values for the same material in Ref. [10].

Both Bragg mirrors and single layers were characterized using a using a spectrophotometer (Perkin-Elmer NIR-UV) and a variable angle spectroscopic ellipsometer (VASE) instrument. The index for the sputtered a-Si (see Fig. 4.6) was extracted from fitting VASE[i] data from a 1 period film of SiO_2 and a-Si, and this was compared to the index of a-Si reported in Ref. [10]. The agreement between the extracted and reported values is quite reasonable. The extracted extinction coefficient for a-Si is shown in Fig. 4.7, and the previously reported values [10] are displayed in Fig. 4.8. The extracted index for SiO_2 from a single film is displayed in Fig. 4.9 and confirms that the index is in reasonable agreement with the reported values displayed on the same graph. The extinction coefficient for SiO_2 in this wavelength range was essentially zero which is consistent with Ref. [10]. Fig. 4.10 shows the reflectance spectra at an incident

angle of twenty degrees from a VASE scan, along with the modeled plot of a four-period sample of SiO_2/a-Si. Fig. 4.11 shows a spectrophotometer scan of the same sample at a five degree incidence angle. The modeled layer thicknesses were 257.7 nm for the SiO_2 layer and 113 nm for the a-Si layer, which compares well to the target thicknesses of 265 nm and 107 nm, respectively. Attenuation in the fibre built into the ellipsometer prevents reflectance measurements past 1500 nm.

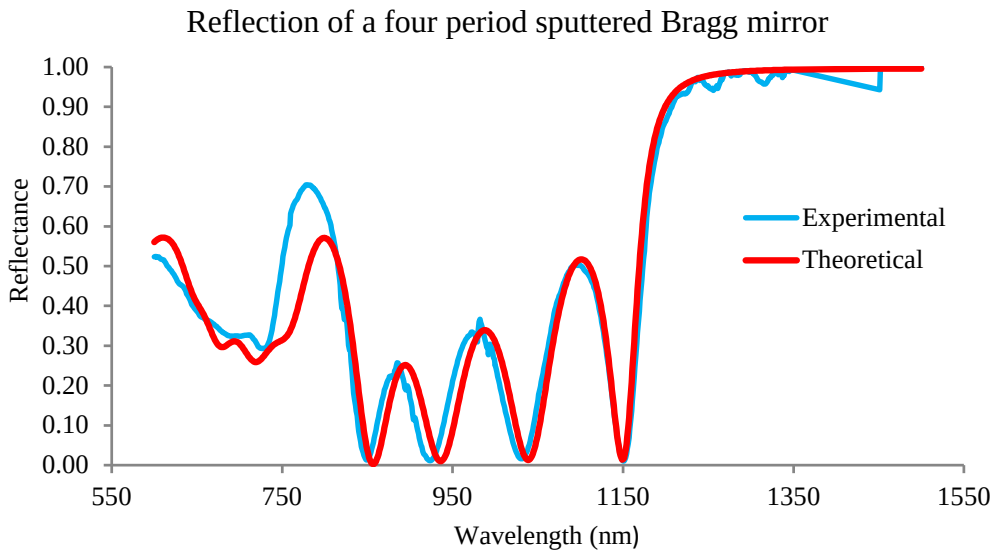

Figure 4.10 - Reflection scan of a four period a-Si/SiO2 Bragg reflector designed for use as the upper and lower cladding of the hollow waveguides.

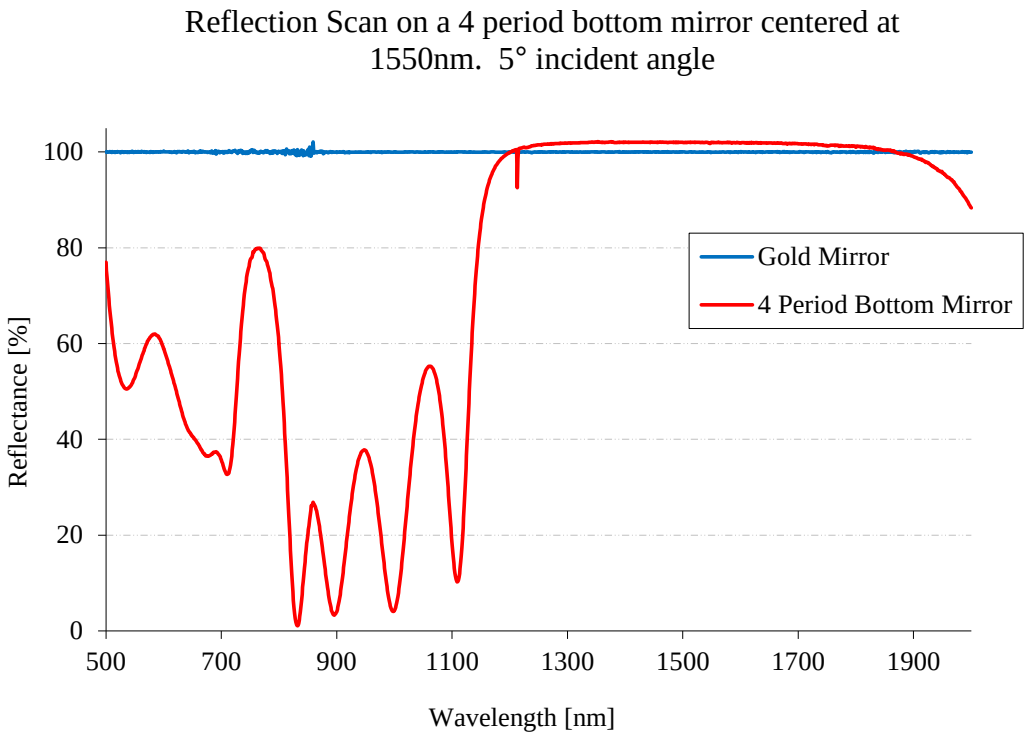

Figure 4.11 – Spectrophotometer scan of a four period Bragg reflector contrasted to the reflectance of a gold mirror at a five degree incidence angle.

The results of the spectrophotometer scan (Fig. 4.11) show a bandgap that is ~800 nm wide, consistent with the ellipsometer scans. A gold mirror was used as a calibration reference. The sharp reflection peaks and close agreement between theory and experiment indicate well defined interfaces between the high and low index layers. The width of the stopband is comparable to results from other groups [11] [12].

In Ref. [12] the stopband is larger possibly due to the higher index of Si (~3.5). TEM images (Fig. 4.12) were obtained to inspect the quality of the interfaces between the a-Si and SiO_2, and to confirm thickness estimates. The image shown in Fig. 4.12 is not from the same sample that was optically

characterized above but they were d with the same conditions other than the actual sputter times.

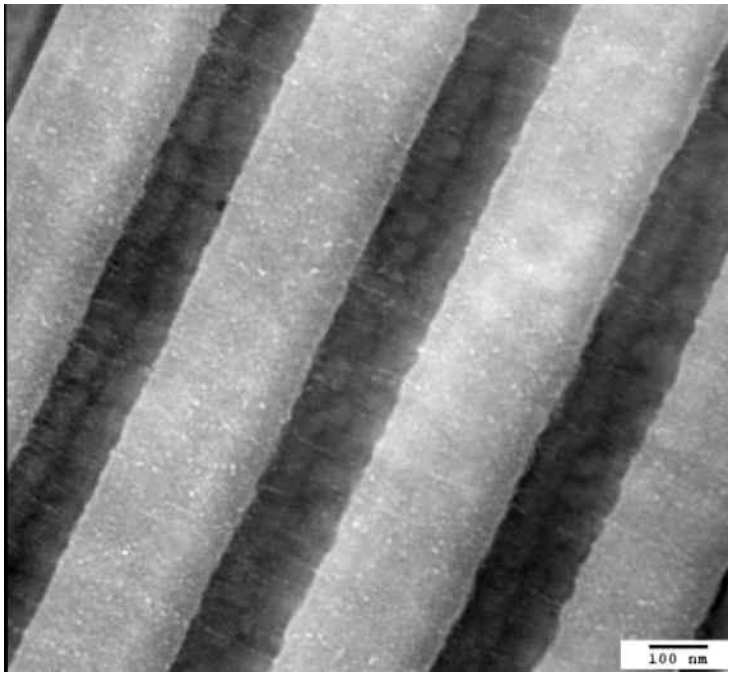

Figure 4.12 - A TEM image showing the sputtered multilayers. The Si layers are the darker color.

4.2.3 Electron Beam Setup

Electron beam (e-beam) evaporation has become one of the most popular vacuum deposition methods for thin films [8]. Historically, the first evaporation methods incorporated resistive heating and had several disadvantages including contamination by crucibles, heaters and supporting hardware. Furthermore the low input power levels made it difficult to deposit high-melting-point materials at reasonable rates [8]. E-beam evaporation has basically eliminated these disadvantages and is able to deposit films with relatively uniform thickness and composition. In order to determine the most appropriate method to create the

Bragg cladding mirrors, both electron beam evaporation and sputtering methods were attempted and the results were compared and contrasted against each other.

Figure 4.13 - Image of the e-beam control system. The Ion gauge controller is on the top while the two crystal monitors are immediately below. The e-beam control unit is the bottom screen, and the voltage and current is controlled by the middle unit.

Housed in the condensed matter lab of the Department of Physics at the University of Alberta, the machine is a six pocket electron beam evaporation system. The chamber is connected to a mechanical roughing pump to bring it from atmospheric pressure to ~500 mTorr, at which point a diffusion pump is connected to enable pumping to the low 10^{-7} Torr range in ~90 minutes. Back diffusion of heated oil from the diffusion pump is prevented with two cold traps; one uses chilled water, and the other is cooled with liquid nitrogen. An image of the power supply, ion gauge controller, crystal monitors, and e-beam controller is

displayed in Fig. 4.13. The general operation of an e-beam system is discussed in Sect. 2.2.

4.2.4 Electron Beam Deposition of Bragg Mirrors

The six pocket hearth is water cooled, which allows for multiple deposition sources or for deposition of thicker films. The e-beam can be directed to a stationary position or scanned across the crucible in multiple computer controlled patterns to change the properties of the melt. In the case of the four period Bragg reflectors used in this project, one graphite crucible filled with poly-crystalline silicon and two copper crucibles filled with SiO_2 were used. The base pressure of the depositions was in the mid 10^{-7} Torr range. Once this pressure was reached, a heater was activated to bring the substrate temperature to ~285 °C. The primary reason for heating the substrate was to increase the compressive stress level of the multilayer, according to behaviour reported for other e-beam films [13]. When deposited at room temperature, we found the stress of the four period multilayers was approximately zero. Heating the substrate during deposition resulted in a net compressive stress of ~150 MPa. The primary driver of the stress was the SiO_2 layer, which is compressively stressed at ~350 MPa. Even when deposited at 285 °C, the a-Si layer was ~220 MPa tensile. This was an improvement, however, over the ~270 MPa tensile. value for a-Si at a deposition temperature of 200 °C.

Once the substrate temperature is stable, the deposition commences and alternates between the SiO_2 and Si sources. One crucible of SiO_2 is used for two layers of the 1550 nm Bragg reflector before switching to the other SiO_2 crucible

for the last two layers. The deposition conditions are listed in Table 4.2. The deposition rates can be raised by increasing the current but this was found to introduce an unacceptable number of defects into the films and an increased chance of crucible damage.

	Rate (Å/s)	Pressure (μTorr)	Current (A)	Thickness (nm)
a-Si	3	1	0.1	107
SiO_2	5	1	0.06	258
Base Pressure = 1.1 * E-6 Torr				Temp = 285 °C

Table 4.2 - Deposition conditions for four period Bragg mirrors deposited in the e-beam system.

Several details had to be taken into account during the depositions. The silicon forms a local melt quickly, but all the silicon material must be molten before a substantial deposition rate is realized; this results in significant heating of the crucible and care must be taken, as the emission current is increased, in order to avoid cracking of the graphite liner. Evaporation of the SiO_2 was comparatively straightforward with the e-beam forming a local melt inside the crucible. This allows the emission current to be ramped up and down relatively quickly. Film thickness was monitored using two quartz crystal oscillators. Electromechanical transducers allow the monitors to detect changes in film mass on the order of $\sim 10^{-8}$ g which, along with the film density, enables a calculation of the expected film thickness[14]. The operation of the device is based on monitoring the changes in the fundamental frequency (f) which is related linearly to the change in thickness (δd) by

$$\delta f = -\frac{f^2 \delta d}{C}, \qquad 4.2$$

where $C = v_q/2$ and is a frequency constant that depends on the quartz crystal.

Film thicknesses were confirmed using both an Alphastep profilometer and from optical spectrophotometer data. TEM images (See Fig. 4.14) showed, sharp interfaces, and thicknesses that were in reasonable agreement with the Alphastep measurements.

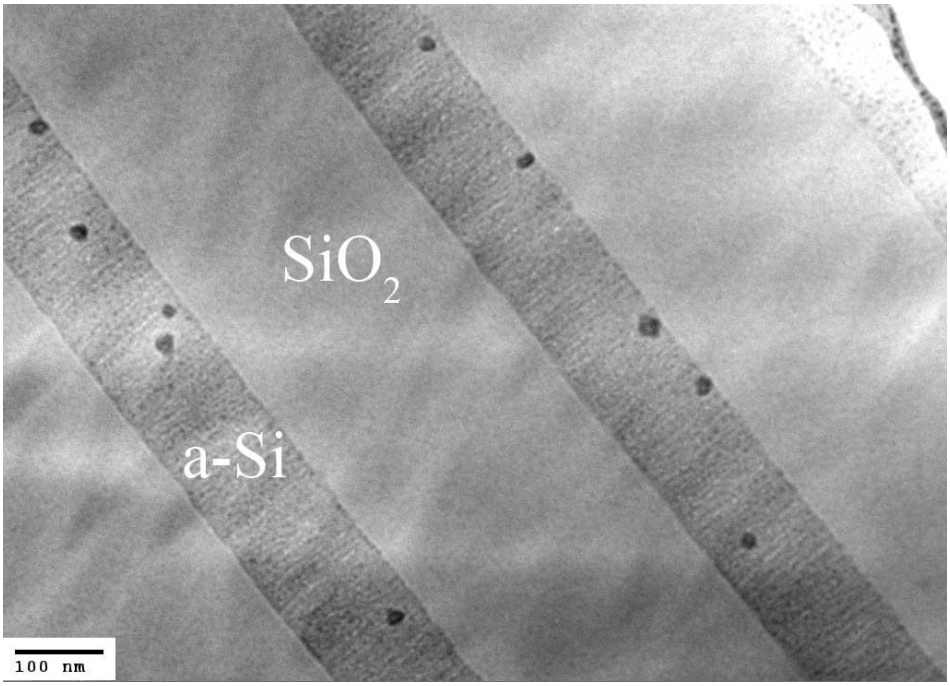

Figure 4.14 – A TEM image showing several layers of the Bragg reflector deposited by e-beam deposition.[ii]

Both monitors are placed near the substrate location and typically give similar although slightly different values. The deposition times are typically determined by taking an average from both of the monitors. The entire deposition process

takes a full day, but during the pump-down stages the monitoring of the system requires only refilling of the liquid nitrogen container once per hour.

Optical characterization of the thin films was completed using the same spectrophotometer and VASE ellipsometer methods as used for the sputtered films. The profilometer also confirmed the total thickness of the multilayers. The reflection of a four-period mirror with a quarter wave stack at 1550 nm is shown in Fig 4.15. In this case, modelling and fitting was done using a matrix transfer method in MatLab and resulted in estimates for layer thicknesses of 265 nm for SiO_2 and 110 nm for a-Si. Targeted thickness was 267 nm for SiO_2 and 111 nm for a-Si. The crystal monitors, which allow *in situ* thickness monitoring, are significant advantage of the e-beam systems. The optical constants used for modelling were those reported in Figs. 4.6,4.8,4.9 from Ref. [10].

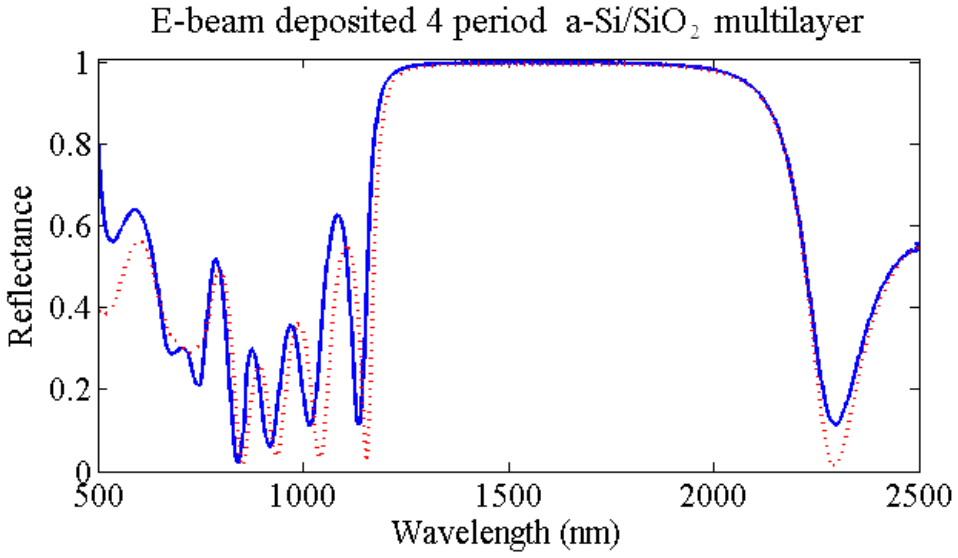

Figure 4.15 - A reflectance scan of a 4-period e-beam deposition. The modeled data was produced using the matrix transfer method in Mat Lab[iii].

4.3 Development of Patterned Low Adhesion Layers

Developing a suitable low adhesion layer (LAL) was one of the critical steps in the realization of a silicon based Bragg waveguide. As discussed in Chapter 2 patterned LALs employed to produce buckles were first demonstrated by Moon *et al.* [15]. That particular process involved depositing a thin layer of aluminum (~3 nm) which was patterned using lift-off prior to pulsed laser deposition of a diamond like carbon layer. The DeCorby group's previous experience developing a robust process for the waveguides discussed in Chapter 3 provided a solid foundation to begin work on the silicon-based waveguides. Towards this end, the following factors were taken into account for the LAL:

- The material must possess suitable optical properties(sufficiently low loss, etc) in the wavelength range of interest;
- The LAL film must be uniform and free of pinholes when deposited as a thin layer (~15 nm);
- The LAL should exhibit low to moderate adhesion to a-Si;
- The LAL should be suitable for patterning by lithography, lift-off, or etching.

The final requirement (suitability for patterning) increases the difficulty in determining a suitable LAL, because the primary materials that were investigated

were chosen for their potentially low adhesion to silicon. On the other hand, the material must be able to survive a lift-off process, or some other lithographic technique. Finding the right balance between adhesion and pattern quality was one of the tougher tasks in this project.

Fig. 4.16 shows buckled strips along patterned areas that were nucleated from a larger area by using nanoindentation. This image was published by Moon *et al.* to demonstrate controlled buckling in a thin film. The buckles propagate from the indent in the large area and finally into the smaller strips. Moon *et al.* demonstrated that the buckle formation could be restricted to patterned areas and that the type of buckles could be controlled by varying the pattern width or the amount compressive of stress in the layers. While Moon *et al.* investigated the three types of buckles discussed in Chapter 2, the goal of the present project was to find a process that could consistently form straight-sided Euler buckles in the low adhesion patterned areas of interest (typically strips with width in the 40 to 80 μm range).

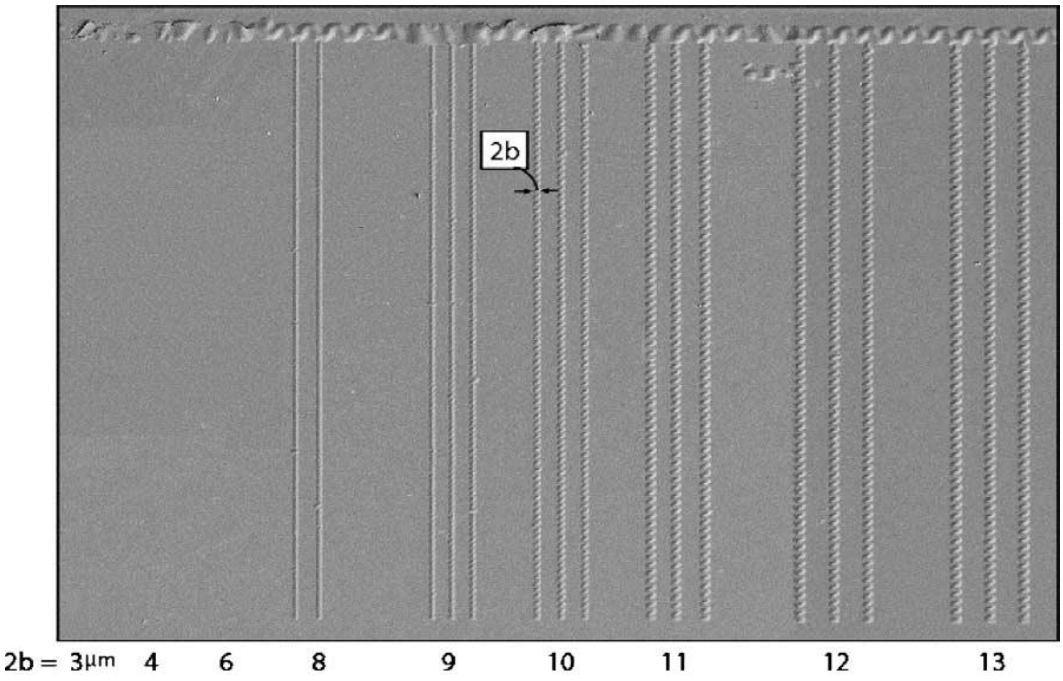

Figure 4.16 –Different types of buckles formed using patterned areas of low adhesion. Note that buckles labeled 8 are straight-sided but as the pattern gets larger they become more telephone cord like [15].

The large volume of literature available regarding the adhesion of various materials to silicon made finding a suitable LAL more manageable [16]. LAL's for MEMs devices, in particular coatings that reduce friction of moving parts, have been the subject of in-depth research [17]. Many techniques have been deployed to reduce the adhesion of silicon films and many take advantage of an ultrathin coating film or use chemical modification to alter the surface [17]. Hard inorganic films such as Diamond-like carbon, titanium nitride, titanium carbide, and silicon carbide exhibit low adhesion and have been used for this purpose [18]. Another technique for modifying the surface adhesion involves applying monolayer-thick films referred to as self-assembled monolayers (SAMs) [19]. The

disadvantage of those layers is that their monolayer thickness implies an increase in the possibility of defects and problems with achieving uniformity throughout the wafer. Metals were also considered, because many are known to exhibit poor adhesion to a-Si and because of the relative ease that they can be deposited and patterned. However, the optical loss of metals decreased their attractiveness. Copper in particular displays some interesting properties for use as a low adhesion layer. Copper has been shown to have poor adhesion to silicon [20] and shows a high propensity for diffusion into both silicon and silicon dioxide layers [21]. While this would be seen as a disadvantage for many processes, in our case it was thought that it could result in a void between the upper and lower cladding mirrors, which might act as a nucleation spot for buckling. Some success was observed using Cu as a LAL (see Sec. 4.4), but the anticipated increase in the optical propagation loss the waveguides favoured other LAL materials.

The LALs that produced the highest quality results were fluorocarbon layers deposited using the passivation process of an inductively coupled plasma reactive ion etch (ICP-RIE) machine. Exploration of this material was prompted by the number of fluorocarbon materials, such as Teflon, that have been studied as a low adhesion surfaces and which are used extensively as non-stick coatings [22]. In one case, fluorocarbon films have been used as a non-stiction coating on a valve seat to reduce the opening pressure of microvalves that were fabricated from a Si/SiO_2 and polyimide film interface [23].

Although critical to essentially all thin film processes, adhesion is one of the least understood properties. Several different methods are used to quantify

adhesion, but there is no universally accepted technique. Since the primary goal of this project was not to measure adhesion, but rather to develop a new type of waveguide, the literature was vetted to determine appropriate materials. Two properties relating to the adhesion of thin films are often referenced; the surface energy, and the work of adhesion. The energy at the surface of a material, called surface energy, is in excess of the bulk energy and is related to several surface properties including adhesion [24-27]. The work of adhesion, which is the energy required to separate two different surfaces, is often used to determine the adhesion strength. Multiple methods exist to measure the work of adhesion, [28],[29], but they can be time consuming and labour intensive. In order to increase the chances of finding a suitable LAL without doing adhesion tests, silicon wafers were deposited with four-period Bragg reflectors and then were cleaved into quarter wafers. Subsequently, different LALs were deposited and patterned on each piece. The pieces were then loaded into the sputtering machine for simultaneous deposition of upper cladding onto the four quarters. This reduced processing time and minimized the variables in the development cycle. Several different techniques were attempted to induce buckling after deposition of the upper mirror, as further discussed in Sect. 4.4.

4.3.1 Fluorocarbon Deposition and Patterning

After deposition of a Bragg reflector designed to act as the bottom cladding, the next step is to deposit a patterned low adhesion fluorocarbon layer. Prior to this, the wafers were cleaned using a piranha solution. As discussed earlier, this

removes organic substances and other contaminants from the surface of the Bragg reflector. Incidentally, this is one of the advantages of using silicon based materials, as many other materials would be attacked by this cleaning step. A Yes hexamethyldisilazane (HMDS) oven is used to deposit a layer of HMDS on the substrate to promote adhesion of the photoresist. The thickness of this film is on the order of a few nm. A substrate spinner is used next to apply the resist (HPR-504). After a 10 s, 500 RPM spread period, the rotation accelerates to 4000 RPM for 40 s. The substrate is immediately transferred to a hotplate that cures the resist for 90 s at 120 °C. A hydrogenation step follows, wherein the wafer is left in the hydrogen atmosphere for fifteen minutes. Exposure of the resist is done with UV light on an ABM mask aligner with a CCD alignment system and using an average exposure power of 14.2 mW/cm^2 at 365 nm. The mask is cleaned in "cold" (~30 °C) piranha to remove any dust or photoresist residue. Developing is done in a solution of Microposit 354 developer for approximately 45 s. The end time is not a set period but is determined by noting the color of the exposed areas as the solution is agitated with a gentle rocking motion. Once the bare silicon is visible throughout the pattern the substrate is immediately removed and submerged in DI water while being rinsed with a spray gun at the same time. The developed substrate is then inspected for pattern quality and accuracy. There are a few specific shapes and patterns that are examined to ensure the waveguide locations are accurately defined. Crosses on the mask, used as dividers between waveguide sets, are very sensitive to development time and will show notches in the corners if overdeveloped. If it's needed, a piranha clean can be done on the

substrate to remove all photoresist and then the patterning can be repeated. With the photoresist pattern in place, the next step is to deposit the fluorocarbon on the substrate. The Minilock-Orion (ICP-RIE) Surface Technologies machine is used for both isotropic and anisotropic dry etching of silicon, silicon oxide, and silicon nitride. An inductively coupled plasma RF generator produces a high-density plasma which allows for lower process pressures. A feed gas of C_4F_8 is fed into the chamber and forms ions and free radicals such as CF_2, CF_3, CF, and C_xF_y and which diffuse to the substrate and polymerize to form a $(C_xF_y)_z$ film. The flow rate of the feed gas was 60 sccm and it was deposited at a base pressure of 1 mTorr and an RF power of 300 W. The actual ratio of the different fluorocarbons in the film is not believed to be particularly important, because their adhesion is relatively invariant, as shown in Fig. 4.17.

Chemical moiety	Binding energy (eV)
$CF_2 - \underline{C}H_2 - CF_2$	287.45
$CH_2 - \underline{C}F_2 - CF_2$ | CF_3	289.67
$CF_2 - \underline{C}F_2 - CH_2$	291.61
$CH_2 - \underline{C}H_2 - CF_2$ | CF_3	293.61

Figure 4.17 - The binding energy of different fluorocarbon films deposited by ICP-RIE, adapted from [24].

After deposition of this layer patterning is completed by lift-off. Removal of the photoresist is done by sonication for twenty minutes in an acetone bath. The substrate is then submerged in isopropanol alcohol (IPA) and bathed in a DI water

dump rinse machine. The liquid is blown off of the wafer using compressed nitrogen. The end result is a thin patterned fluorocarbon film with low, pinhole density [30], low coefficient of friction, and low surface energy.

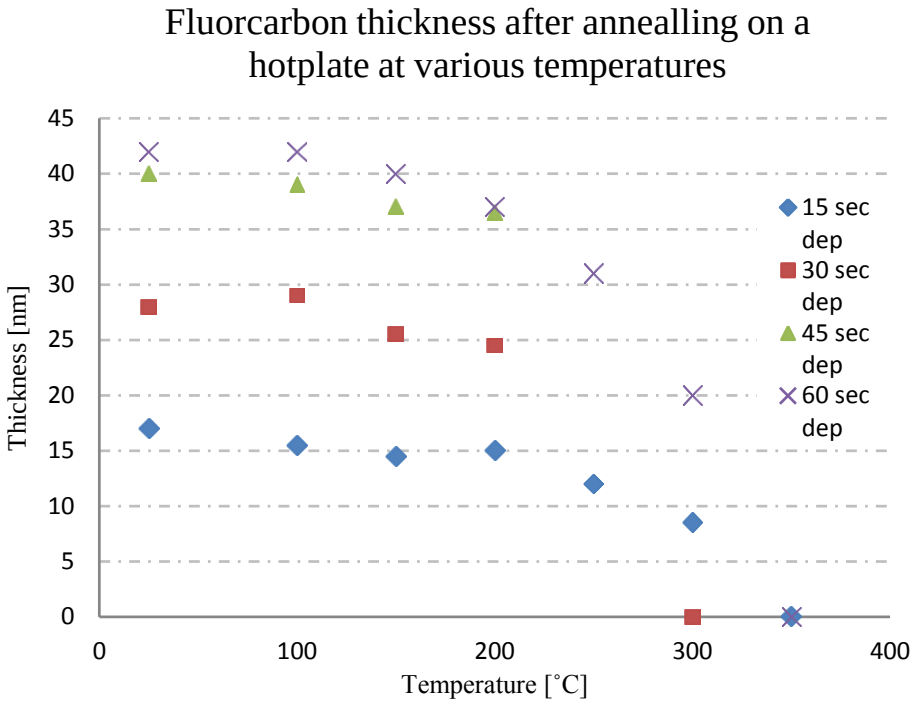

Figure 4.18 – The thermal stability of a fluorocarbon layer deposited with various thicknesses and heated to multiple temperatures.

In order to investigate the thermal stability of the fluorocarbon layers several samples were deposited at varying thickness. They were then heated on a hotplate in an air atmosphere to 350 °C. At 50 °C increments the sample was taken off and the thickness was measured with a contact profilometer (Alphastep). At each temperature, the total heating time was ~1 hour. At temperatures above 300 °C a rapid decomposition of the thickness was observed (Fig. 4.18), which is consistent with a more in depth study performed by Zhuang [25].

4.3.2 Patterning of Other Low Adhesion Layers

Determination of a suitable LAL was by no means a trivial process. Several different materials were patterned in order to discover if buckling was possible. Some of the other materials deposited and patterned were copper, gold, silver, aluminum, Cytop [31], and Parylene. Deposition and pattering of the metal layers was fairly straightforward, because they could be were sputtered using the same system as that used for the a-Si/SiO_2 Bragg mirrors. Metals were patterned with a lift-off procedure (similar to the fluorocarbon patterning), the only major difference being the amount of time spent sonicating the sample. Slight adjustments were made by inspecting with a microscope and profilometer to check pattern integrity and sidewall height respectively.

The Parylene was deposited by a PDS 2010 vacuum system which uses chemical vapour deposition to produce a clear polymer coating on the substrate. Due to the elasticity of the Parylene, it was not possible to use lift-off as the patterning technique. Instead, a contiguous layer of Parylene was deposited followed by a patterned photoresist. Subsequently RIE was used to remove all but the masked Parylene. The photoresist was removed with acetone, leaving a patterned Parylene layer. Parylene was also used as a protective layer on top of the waveguides. In some cases ~100 nm of Parylene was deposited after deposition of the upper cladding but before buckling of the waveguides, with the hope that this would reduce cracking and fractures in the buckled regions.

4.4 Buckling Experiments and Results

Once patterning of the LAL is complete, a second Bragg reflector (designated as the upper cladding of the hollow waveguides) is deposited onto the substrate. The same deposition method that was described earlier in Sec. 4.2.2 was used, since it allowed for a large degree of control over the compressive stress of the mirror. The level of stress is critical in this top mirror, which will eventually act as an upper cladding to the waveguides, is critical because these layers are designed to buckle. In fact the bottom mirror can be deposited by any method that produces a suitable bandgap and other optical properties.

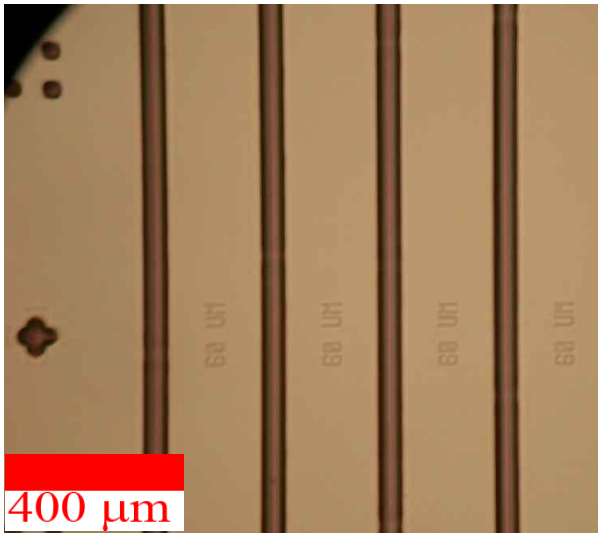

Figure 4.19 - Microscope image of 60 µm straight-sided waveguides. The waveguides were heated to induce buckling.

The last step in fabricating the waveguides is controlled thin film buckling to create an air core clad by a four-period upper and lower a-Si/SiO_2 Bragg reflector (see Fig. 4.19 the method) . While refining the buckling process is currently a major focus, high yields have already been achieved in buckling of the

patterned waveguides (Fig. 4.19). Basically, three methods have been used to induce buckling with varying degrees of success: a stressed overlayer (sputtered tungsten) was added to increase compressive stress, samples were dipped in liquid nitrogen to introduce a thermal shock, and the substrates were heated to reduce the adhesion of the LAL and also introduce a thermal shock. To date, the most promising technique is heating of the samples. The heating process was conducted in an air atmosphere on manually controlled hotplates. The influence of a nitrogen atmosphere was also experimented with but the results were not as promising and yielded a much lower percentage of usable waveguides. To maintain a constant heating rate, it was necessary to constantly change the temperature setting.

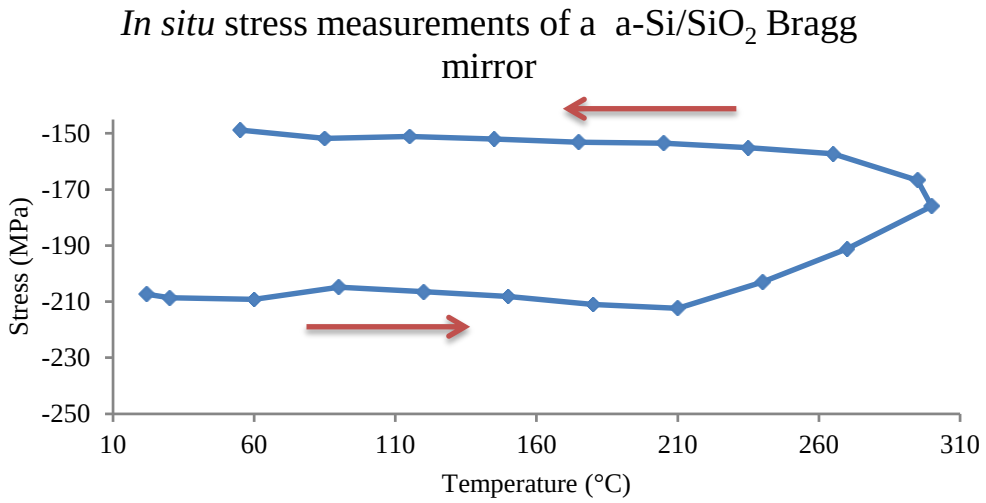

Figure 4.20 – Stress of a four period sputter deposited Bragg mirror that is heated up at a constant rate of 10°/min and let to cool. Arrows indicate the direction of heating.

Several factors must be considered when deciding on how to best heat the sample. Compressive stress from the sputtered layers is required to drive the formation of the straight sided buckles. If the rate of heating is too slow, the

compressive stress might be reduced prior to buckling, thereby reducing the height of the buckles, and the chance of buckle formation. This is supported by the measured stress behaviour of a 4 period Bragg mirror, made using the same sputter conditions, and which was heated on a Flexus 2320 stress measurement machine. The sample's stress was measured every thirty degrees as it was heated to 300 °C and then again at every thirty degrees as it cooled, (Fig. 4.20). A relaxation of the compressive stress is evident when the multilayer is heated past 210 °C, and tthe original stress level is not restored upon cooling. If the film is heated too fast, it was observed that the thermal shock can cause telephone cord buckles to form, whereas straight-sided Euler buckles are desired for the waveguide. The next sections detail several samples studied in the development of the waveguide fabrication process; these samples are representative of the different methods attempted. Table 4.3 is a summary of the samples showing important deposition and processing information.

Sample	**Bottom Cladding**	**Teflon Thickness**	**Target Wavelength**	**Parylene Overlayer**	**80 µm W.G.**	**60 µm W.G.**
110510A P4	1 Period	~10nm	1550 nm	Yes	2.6 µm	1.8 µm
010610A P2	4 Period E-beam	30 nm	1550 nm	Yes	2.8 µm	1.8 µm
300710D 2 P1	4 Period	8.5 nm	1550 nm	No	.96 µm	.55 µm
180610A P5	4 Period	16 nm	1550 nm	Yes	2.4 µm	1.8 µm
080710A 2 P3	5 Period	13 nm	1000 nm	No	3.1 µm	2.5 µm

Table 4.3 - Processing information for several significant wafers that used a fluorocarbon as a LAL. W.G. refers to waveguide height for the listed LAL width.

4.4.1 Sample 110510A P4

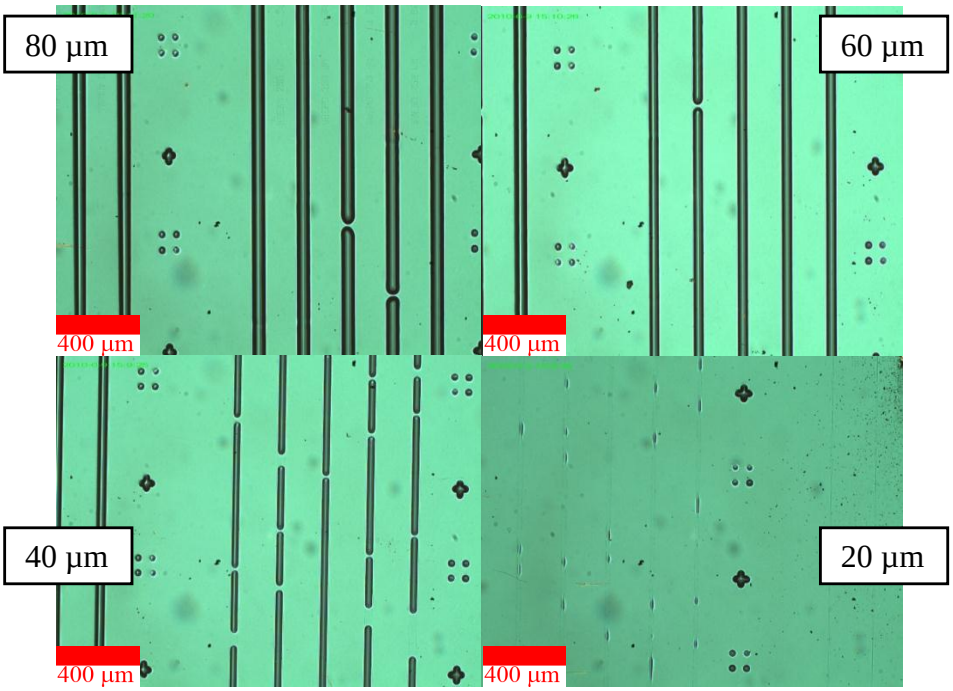

Figure 4.21 – Microscope images of four different size waveguides from sample 110510A - P2.

This sample was designed as a side-by-side comparison of promising LALs, and the first sample to use a fluorocarbon pattern as a LAL. For efficiency, and since the main purpose was to study alternate LALs, only 1 period was deposited for the bottom cladding layers (1 period of SiO_2 and on layer of a-Si). After this deposition the wafer was cleaved into quarters. A different LAL was deposited onto each quarter: copper, aluminum, gold and fluorocarbon. A 4 period top cladding, with the stop band centered at 1550 nm, was sputtered onto all 4 quarters of the sample. Initially, the most promising material was thought to be copper, because buckles were evident in the large patterned areas as soon as that sample was removed from the sputtering chamber. This was the first type of

material to delaminate without the use of heating or any other method to induce buckling. An SEM image of a buckle, displayed in Fig. 4.22, shows a promising shape and height (~2.2 μm) for waveguide application. The particular buckles shown formed after a deposition of a tungsten overlayer (200 nm) to increase the compressive stress. One issue observed with the copper LAL was that the buckles tended of to crack at the edges of the delamination. This was not ideal, although the effect on light propagation might minimal assuming the buckles could be protected from any further damage.

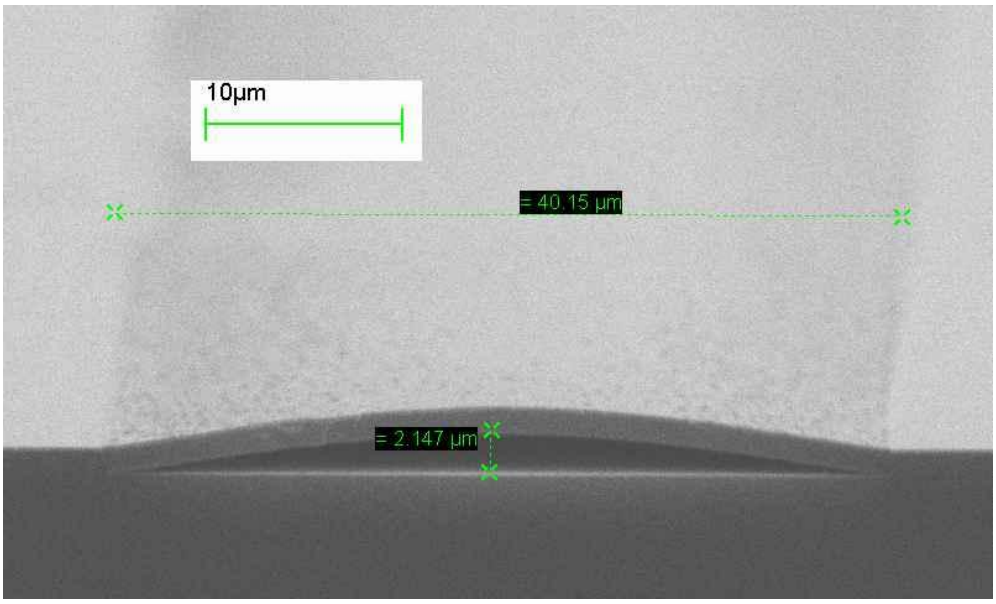

Figure 4.22 - SEM image of the cleaved facet of a buckle formed using a Cu LAL.

The Cu samples were heated alongside the fluorocarbon and the other LAL samples. The only samples observed to buckle were those with the Cu and fluorocarbon LAL. The fluorocarbon sample actually buckled at a much higher temperature (~ 400 °C) after it was moved to a different hotplate. The height of waveguides, on the sample with a fluorocarbon LAL, was 2.6 and 1.8 μm for the

80 and 60 μm waveguides respectively (see Fig 4.23). Microscope images of these waveguides are shown in Fig. 4.21.

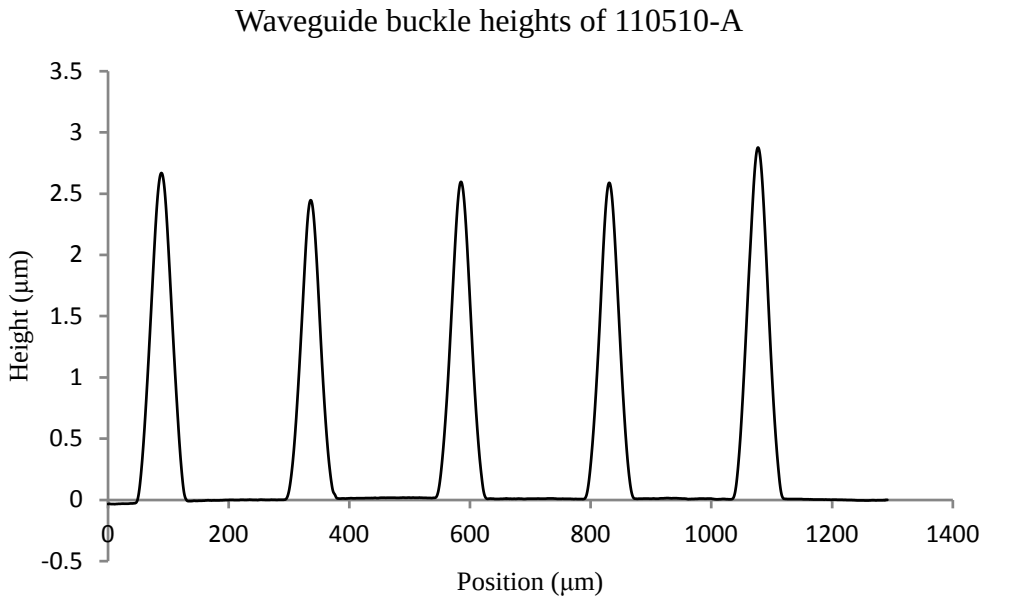

Figure 4.23 - Contact profilometer scan of sample 110510-A showing the height and shape of 80 μm waveguides.

Notice that although a large percentage of the 80 and 60 μm waveguides are buckled, few of the 20 μm waveguides delaminated. Even fewer of the 10 μm guides buckled, as expected (see Sec. 5.3.3). Although the waveguides with a Cu LAL formed waveguides with a larger air-core,, the decision was made to focus initially on using fluorocarbon as a LAL. This was primarily motivated by the concern over the interference a metal layer could have with the propagation of light through a Bragg waveguide.

In an attempt to reduce fractures and cracking on the buckled waveguides a layer (~ 100 nm) of Parylene was deposited before the buckling experiments.

The effectiveness of this coating is an area of ongoing research but currently the highest yield sample (see Sec. 4.4.6) did not have a Parylene coating on it. Nevertheless the stress of the coating layer was measured, on a blank wafer, and found to be negligible (~4.6 MPa tensile). This factor, along with its transparency in the near infrared, results in no significant disadvantages from depositing the Parylene coating layer.

4.4.2 Sample 010610A - P2

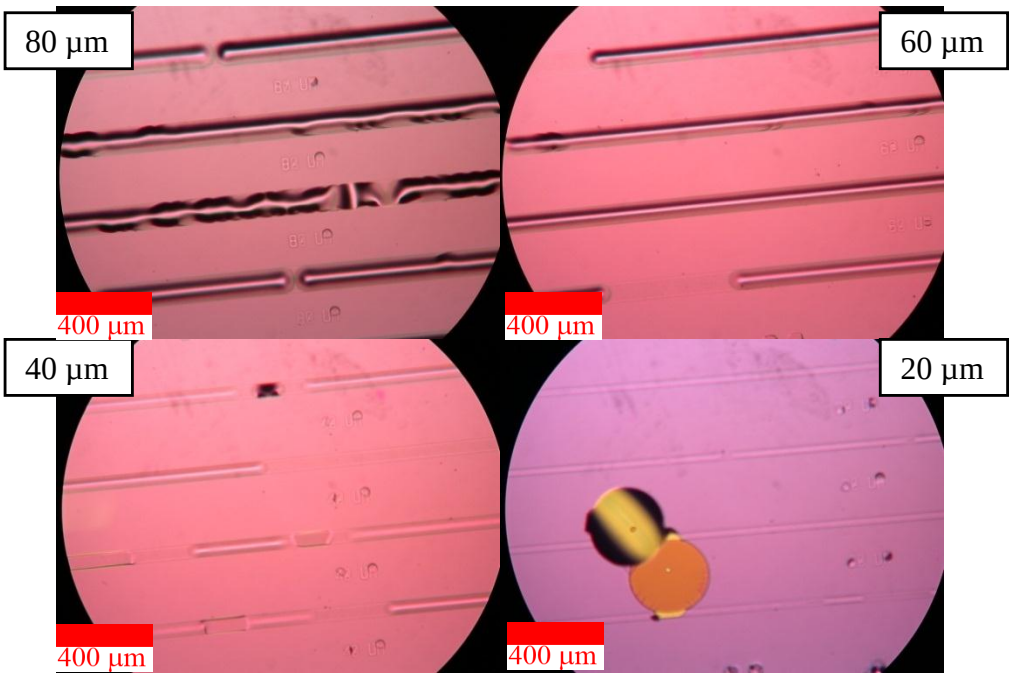

Figure 4.24 - Microscope images of four different size waveguides from sample 010610A-P2.

This sample was the first wafer patterned entirely with a fluorocarbon LAL. The bottom cladding of the waveguides was deposited using e-beam evaporation, resulting in a waveguide with different upper and lower cladding. Parylene was

deposited as an overlayer, for the same reasons given in Sec. 4.4.1. Several methods of heating were investigated to induce buckling, with the most successful results arising from a thermal shock to the wafer. Thermal shock was attempted because of observations from the previous wafer, where buckles were obtained when the sample was suddenly switched from a lower temperature hot plate to a higher temperature hot plate. In the present case, thermal shock was applied to the wafer by preheating the hotplate to a high temp (such as 250 °C) and then placing the sample on to the hotplate for 3-5 seconds. The waveguides were observed to form almost immediately, but the short time on the hot plate made repeatability an issue. The yield of the 60 μm waveguides was reasonably high (~25%) for the 250 °C thermal shock, but many of the larger (80 μm) waveguides showed telephone cord like and varicose buckles, indicating the stress in the layers was too high at the point of buckling. Fig. 4.25 shows an optical profilometer scan of a 60 μm guide; the shape is consistent with an Euler buckle and the height is height consistent with contact profilometer data (not shown). Compared to the results achieved using thermal shock heating, much lower yield was obtained for pieces of this sample heated at a constant ramp rate (~8°C/min)

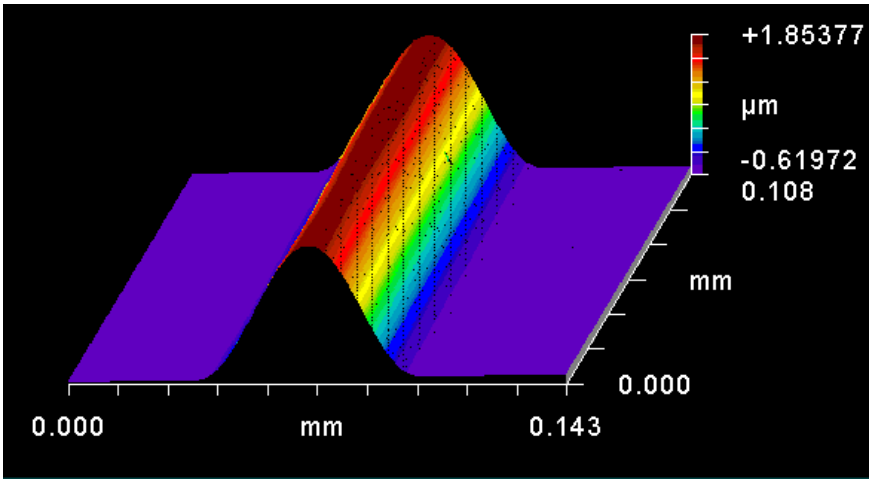

Figure 4.25 - Optical profilometer scan of 010610B sample showing the shape and height of the buckles that resulted from heating the sample.

4.4.3 Sample 300710D 2-P1

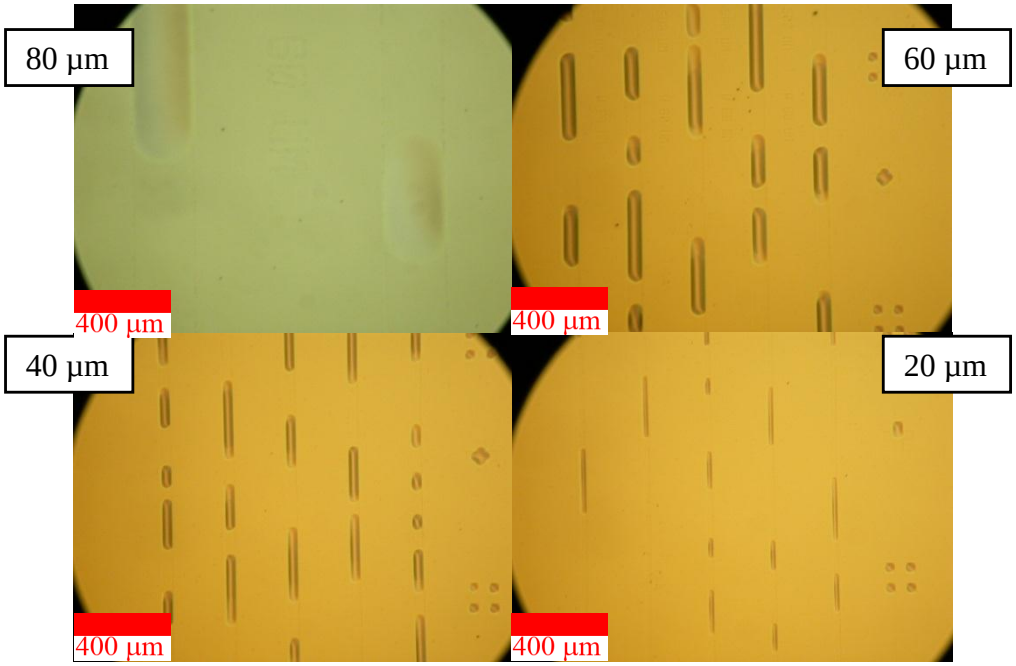

Figure 4.26 - Microscope images of four different size waveguides from sample 300710D 2-P1.

This sample was fabricated with the intent of determining an optimal thickness for the LAL. 4 period bottom cladding was sputtered onto the wafer before it was

cleaved in half. A different thickness of fluorocarbon (~8.5 and ~25 nm) was deposited on to each wafer and then a 4 period upper cladding was sputtered on to both halves at the same time. The microscope images in Fig. 4.26 correspond to the sample with an ~8.5 nm thick LAL. Uniformity was believed to be a concern for a layer this thin. Specifically pinholes and other defects might result in increased adhesion and an increase in the amount of compressive needed to induce buckling. Compared to the previous sample, the results indicated that the quality of the pattern might be lower, resulting in a lower yield of buckles. As discussed below the best results have been seen with a fluorocarbon layer that is 10 - 15 nm thick.

4.4.4 Sample 180610A P5

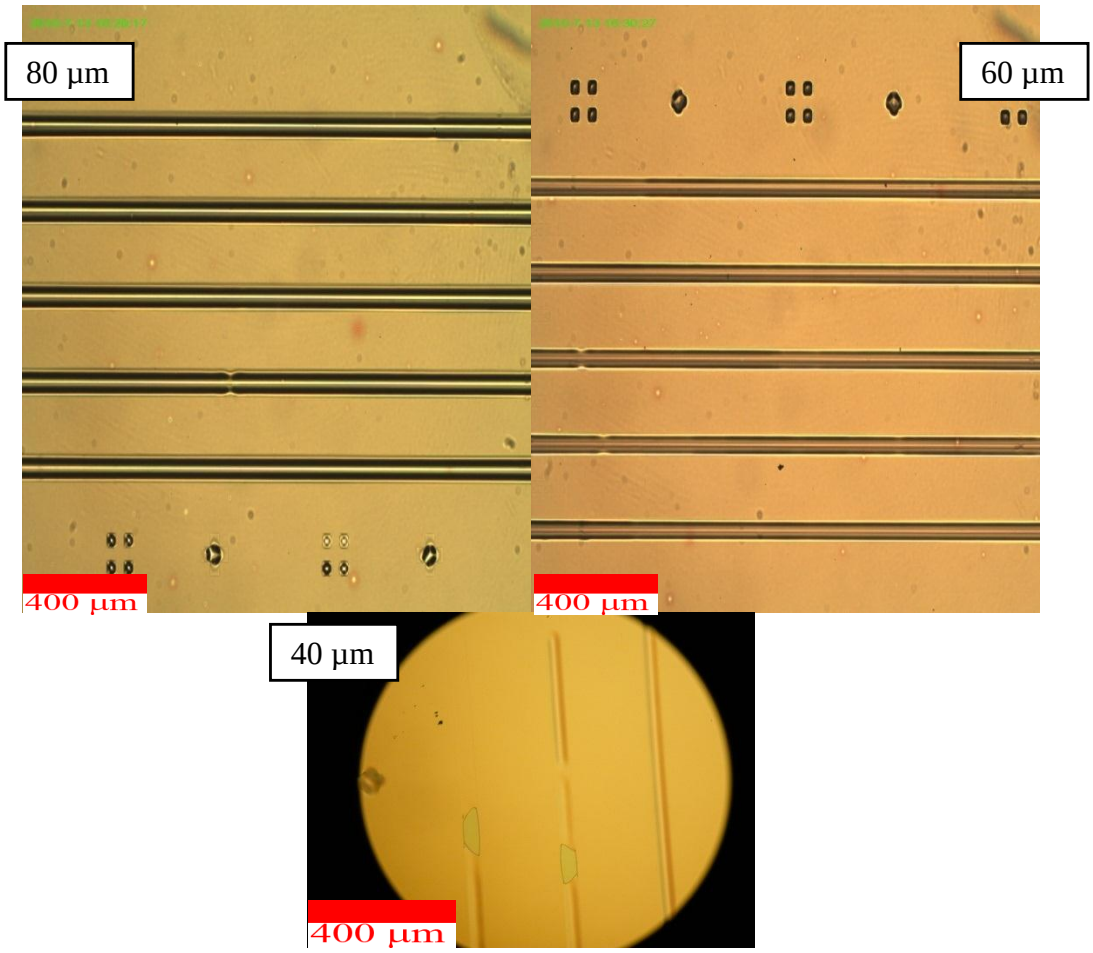

Figure 4.27 - Microscope images of three different size waveguides from sample 160610A-P5.

This sample was fabricated using the sputtering and fluorocarbon recipe described in Secs. 4.2.2 and 4.3.2. Fig. 4.27 shows images of successfully buckled waveguides and demonstrates the high yield from this sample; approximately 80% of the 80 and 60 µm formed straight sided Euler buckles. The sample provided longer waveguides that were suitable for optical characterization (see Sec. 5.4) were realized. These buckles were formed by heating the sample from room temp to 240 °C at a rate of 16 C°/min. Parts of the wafer were used to

experiment with heating in different atmospheres a nitrogen atmosphere. However, the results were not impressive and no buckling was observed until the temperature exceeded 400 °C.

4.4.5 Sample 080710A 2- P3

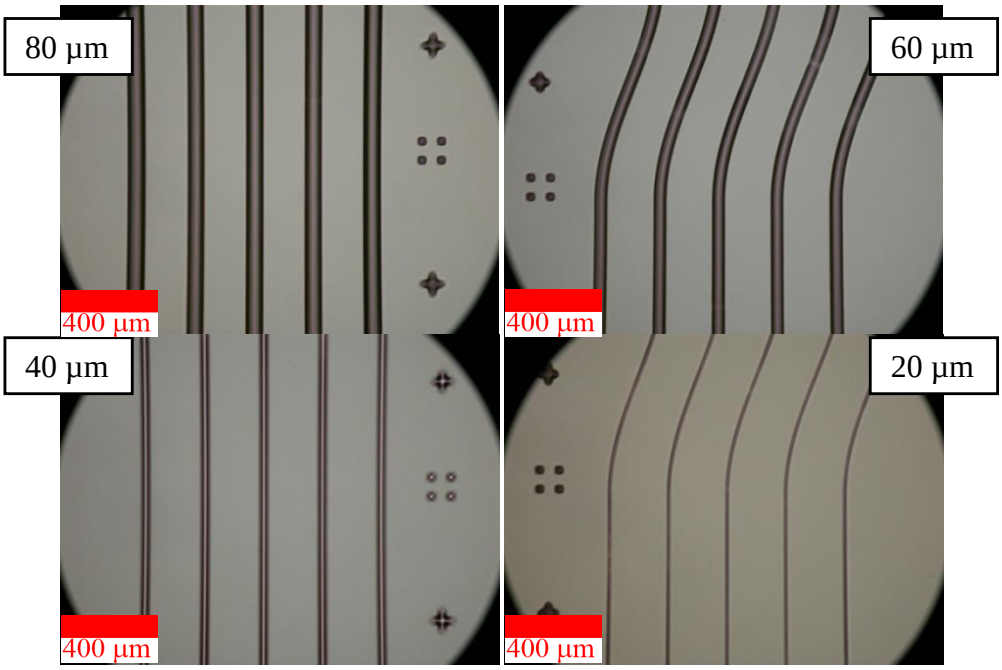

Figure 4.28 – Microscope images of four different size waveguides along from sample 080710A 2 - P3.

To date this sample has produced the highest quality waveguides. On this sample, sputtered layer thicknesses were adjusted to produce a stop band centered near a 1000 nm wavelength. The target layer thicknesses for a-Si and SiO_2 were 70 and 160 nm respectively. Another refinement was that before deposition of the upper mirror, the fluorocarbon pattern was annealed at 100 °C for one hour. This was done in an attempt to improve the hydrophobicity and uniformity of the LAL based on results reported by Zhuang *et al*. [25]. Evidence of the increase in

hydrophobicity was provided by water contact angle tests. Fig 4.29 demonstrates the increase in contact angle for an annealed sample compared to an unannealed sample. To form the buckles shown in Fig. 4.28, the samples were heated to 300 °C over an 18 minute period. Buckling initiated at ~220 ° and the yield of buckled areas increased as the temperature was increased. Cracking and complete delamination of buckles started at ~300 °C. For the 60 and 80 μm guides, yields as high as 85-90 % were observed. The optical waveguiding properties of this sample have not been tested at the time of writing.

Figure 4.29 - Water contact measurement on fluorocarbon films before and after annealing at 100 °C. (left) Contact angle after annealing. (Right) Contact angle before annealing.

4.5 Conclusions

The experimental development of the fabrication process used to create silicon based integrated hollow waveguides was detailed. Two types of deposition techniques, e-beam and sputtering, were used to successfully produce a-Si/SiO2 omnidirectional Bragg reflectors. The final process, described in Chapter 5, uses

sputtering because of the amount of compressive stress that can be incorporated into the silicon based multilayers. These multilayers eventually form the upper and lower cladding of the waveguides. A fluorocarbon layer deposited by CVD was chosen among other possible LALs because of its high buckling yield and optical properties in the wavelength range of interest. Formation of the hollow waveguides was accomplished by stress driven self-assembly due to a combination of compressive stress in the upper cladding and the correct rate of heating. After numerous tests, the highest yields have come from a constant but high (17 °C/min) heating rate. Some samples buckled in over 80% of the predefined low adhesion areas and provided waveguides that were able to successfully guide light.

4.6 Works Cited

[1] W.H. Southwell, "Omnidirectional Mirror Design With Quarter-Wave Dielectric Stacks," *Applied Optics*, vol. 38, 1999, pp. 5464-5467.

[2] K.M. Chen, A.W. Sparks, H. Luan, D.R. Lim, K. Wada, and L.C. Kimerling, "SiO[sub 2]/TiO[sub 2] omnidirectional reflector and microcavity resonator via the sol-gel method," *Applied Physics Letters*, vol. 75, 1999, p. 3805.

[3] H. Park, C. Park, B. Hwang, S.G. Lee, B. O, E. Lee, D. Choi, and S. Park, "Wavelength tunable thermo-optic filter using buckling effect of etalon composed poly-Si/SiO2 multi-layers," *Optical Materials*, vol. 27, Feb. 2005, pp. 787-791.

[4] G.R. Hadley, J.G. Fleming, and S. Lin, "Bragg fiber design for linear polarization," *Optics Letters*, vol. 29, Apr. 2004, pp. 809-811.

[5] S. Lo, M. Wang, and C. Chen, "Semiconductor hollow optical waveguides formed by omni-directional reflectors," *Optics Express*, vol. 12, Dec. 2004, pp. 6589-6593.

[6] D.W. Hoffman, "Perspective on stresses in magnetron-sputtered thin films," *The 40th National Symposium of the American Vacuum Society*, Orlando, Florida (USA): AVS, 1994, pp. 953-961.

[7] S. Schiller, K. Goedicke, J. Reschke, V. Kirchhoff, S. Schneider, and F. Milde, "Pulsed magnetron sputter technology," *Surface and Coatings Technology*, vol. 61, Dec. 1993, pp. 331-337.

[8] M. Ohring, *Materials Science of Thin Films [electronic Resource]: Deposition and Structure*, San Diego, CA: Academic Press, 2002.
[9] L.F. Donaghey and K.G. Geraghty, "Effect of target oxidation on reactive sputtering rates of titanium in argon-oxygen plasmas," *Thin Solid Films*, vol. 38, Nov. 1976, pp. 271-280.
[10] E.J. Prucha and E.D. Palik, *Handbook of optical constants of solids, volumes I, II, and III: subject index and contributor index*, Academic Press, 1998.
[11] B. Gallas, S. Fisson, E. Charron, A. Brunet-Bruneau, G. Vuye, and J. Rivory, "Making an Omnidirectional Reflector," *Applied Optics*, vol. 40, Oct. 2001, pp. 5056-5063.
[12] H. Lee, H. Makino, T. Yao, and A. Tanaka, "Si-based omnidirectional reflector and transmission filter optimized at a wavelength of 1.55 μm," *Applied Physics Letters*, vol. 81, 2002, p. 4502.
[13] M.T.K. Soh, J. Thurn, J.H. Thomas, and J.J. Talghader, "Thermally induced stress hysteresis and co-efficient of thermal expansion changes in nanoporous SiO2," *Journal of Physics D: Applied Physics*, vol. 40, 2007, pp. 2176-2182.
[14] L.I. Maissel, R. Glang, and P.P. Budenstein, "Handbook of Thin Film Technology," *Journal of The Electrochemical Society*, vol. 118, Apr. 1971, pp. 114C-115C.
[15] M.-. Moon, K.-. Lee, K.H. Oh, and J.W. Hutchinson, "Buckle delamination on patterned substrates," *Acta Materialia*, vol. 52, Jun. 2004, pp. 3151-3159.
[16] M. Cordill, D. Bahr, N. Moody, and W. Gerberich, "Recent developments in thin film adhesion measurement," *Device and Materials Reliability, IEEE Transactions on*, vol. 4, 2004, pp. 163-168.
[17] B. Bhushan, "Adhesion and stiction: Mechanisms, measurement techniques, and methods for reduction," *Journal of Vacuum Science & Technology B: Microelectronics and Nanometer Structures*, vol. 21, Nov. 2003, pp. 2262-2296.
[18] B. Bhushan, H. Liu, and S.M. Hsu, "Adhesion and Friction Studies of Silicon and Hydrophobic and Low Friction Films and Investigation of Scale Effects," *Journal of Tribology*, vol. 126, Jul. 2004, pp. 583-590.
[19] R. Maboudian, W.R. Ashurst, and C. Carraro, "Self-assembled monolayers as anti-stiction coatings for MEMS: characteristics and recent developments," *Sensors and Actuators A: Physical*, vol. 82, May. 2000, pp. 219-223.
[20] L. Magagnin, R. Maboudian, and C. Carraro, "Selective Deposition of Thin Copper Films onto Silicon with Improved Adhesion," *Electrochemical and Solid-State Letters*, vol. 4, Jan. 2001, pp. C5-C7.
[21] T. Fukuda, H. Nishino, A. Matsuura, and H. Matsunaga, "Force Driving Cu Diffusion into Interlayer Dielectrics," *Japanese Journal of Applied Physics*, vol. 41, 2002, pp. L537-L539.
[22] R.W. Jaszewski, H. Schift, B. Schnyder, A. Schneuwly, and P. Gröning, "The deposition of anti-adhesive ultra-thin teflon-like films and their

interaction with polymers during hot embossing," *Applied Surface Science*, vol. 143, Apr. 1999, pp. 301-308.
[23] J. Han, B. Flachsbart, R.I. Masel, and M.A. Shannon, "Micro-fabricated membrane gas valves with a non-stiction coating deposited by C4 F8/Ar plasma," *Journal of Micromechanics and Microengineering*, vol. 18, 2008, p. 095015.
[24] J. Han, J. Yeom, G. Mensing, D. Joe, R.I. Masel, and M.A. Shannon, "Surface energy approach and AFM verification of the (CF) treated surface effect and its correlation with adhesion reduction in microvalves," *Journal of Micromechanics and Microengineering*, vol. 19, 2009, p. 085017.
[25] Y.X. Zhuang and A. Menon, "Wettability and thermal stability of fluorocarbon films deposited by deep reactive ion etching," *Journal of Vacuum Science & Technology A: Vacuum, Surfaces, and Films*, vol. 23, May. 2005, pp. 434-439.
[26] J. Kim, C. Baek, J. Park, D. Shin, Y. Lee, and Y. Kim, "Continuous anti-stiction coatings using self-assembled monolayers for gold microstructures," *Journal of Micromechanics and Microengineering*, vol. 12, 2002, pp. 688-695.
[27] W.M.V. Spengen, R. Puers, and I.D. Wolf, "A physical model to predict stiction in MEMS," *Journal of Micromechanics and Microengineering*, vol. 12, 2002, pp. 702-713.
[28] A. El Ghzaoui, "Determination of surface energy of polymers by force microscopy," *Journal of Applied Physics*, vol. 85, 1999, p. 1231.
[29] E. Pisanova, S. Zhandarov, and E. Mäder, "How can adhesion be determined from micromechanical tests?," *Composites Part A: Applied Science and Manufacturing*, vol. 32, Mar. , pp. 425-434.
[30] A. Ayon, D. Chen, and R. Khanna, "A Novel Integrated MEMS Process Using Fluorocarbon Films Deposited With a Deep Reactive Ion Etching (DRIE) Tool," *Materials Research Society Symposia Proceedings*, vol. 605, 2000, pp. 141-147.
[31] Y. Matsumoto, K. Yoshida, and M. Ishida, "A novel deposition technique for fluorocarbon films and its applications for bulk- and surface-micromachined devices," *Sensors and Actuators A: Physical*, vol. 66, Apr. 1998, pp. 308-314.

Chapter 5 Hollow Bragg Waveguides Fabricated by Controlled Buckling of Si/SiO_2 Multilayers

5.1 Introduction

This chapter describes integrated air-core waveguides with Bragg reflector claddings, fabricated by controlled delamination and buckling of sputtered Si/SiO_2 multilayers. Thin film deposition parameters were tailored to produce a desired amount of compressive stress, and a patterned, embedded fluorocarbon layer was used to define regions of reduced adhesion. Self-assembled air channels formed either spontaneously or upon heating-induced decomposition of the patterned film. Preliminary optical experiments confirmed that light is confined to the air channels by a photonic band-gap guidance mechanism, with loss ~5 dB/cm in the 1550 nm wavelength region. The waveguides employ standard silicon processes and have potential applications in MEMS and lab-on-chip systems. The chapter is based on a paper submitted to optics express for review and is a description of a complete process that employs the methods described in Chapter 4. As this was originally designed to be a standalone journal paper there is some overlap between the Chapters 4 and 5. This was done to ensure completeness in both chapters.

5.2 Background

Integrated air-core waveguides are attracting interest for lab-on-chip [1] and optical interconnect [2],[3] applications. Amongst other attributes, they have potential for widely tunable operation using MEMS-based actuation techniques [4],[5]. Strategies for the fabrication of hollow waveguides include sacrificial etching [1] , wafer bonding [6], and chemical vapor deposition in a pre-defined trench [3] which were discussed in Chapter 2. We recently reported an alternative approach [7],[8] based on the controlled formation of straight-sided delamination buckles [9] within a multilayer thin film stack. The waveguides formed by this process are analogous to those discussed in Chapter 3, which were fabricated using a combination of a chalcogenide glass and a commercial polymer. The silicon-based processing should expand the scope for practical application of these self-assembled waveguides, because of their compatibility with MEMS devices.

5.3 Design and Fabrication

In principle, the buckling self-assembly technique [7],[8] can be adapted to any Bragg reflector material system given: (i) means to control the compressive stress of the layers, and (ii) means to create patterned regions of reduced adhesion at a desired interface. If the refractive index contrast between the materials is sufficient to produce an omnidirectional band gap, enhanced functionality such as low-loss bends [3] and wavelength-dependent, out-of-plane coupling from tapers [10],[11] is possible.

5.3.1 Development of compressively stressed a-Si/SiO2 Bragg mirrors

The index contrast between amorphous silicon (a-Si) and SiO_2 enables a large omnidirectional band gap [12], which has motivated their use for hollow waveguides operating in the 1550 nm wavelength region[3],[6]. The optical losses in a-Si are reasonably low for wavelengths above 800 nm ($\kappa < 0.1$, where κ is the extinction coefficient), and for hydrogenated a-Si (a-Si:H) they can be several orders of magnitude lower [13]. Moreover, a tradeoff between omnidirectional bandwidth and transparency is possible by deposition of SiO_x/SiO_2 multilayers with varying oxygen content, x [14]. In the literature, high quality a-Si/SiO_2 Bragg reflectors have been reported using e-beam evaporation [12] or sputtering [15] of Si and SiO_2 targets, and reactive sputtering of Si targets [14]. For the present work, the a-Si:H/SiO_2 Bragg reflectors reported by Yoda *et al*. [16] had particularly desirable properties including low loss ($\kappa < 10^{-4}$), high index contrast, and high compressive stress for both the a-Si:H and SiO_2 layers. Those multilayers were deposited by reactive rf magnetron sputtering in the presence of O_2 and H_2. A similar system was employed for the waveguides.

Here, Bragg reflectors were deposited in a 3-source magnetron sputtering system, using silicon targets (n-type). Both a-Si and SiO_2 layers were deposited at a pressure of 3.5 mTorr, using a pulsed source (square wave at 150 kHz). For the a-Si layers, substrate bias was 535 V, source power was 200 W, and a Ti target (biased at 50 V and coupled to a 50 W DC source) was used as a getter to reduce oxygen contamination of the growing films. For SiO_2 deposition, substrate bias

was 370 V and source power was again 200 W. Furthermore, the SiO_2 layers were reactively sputtered, with argon and oxygen flow rates of 50 and 2.5 sccm, respectively. The deposition rates for a-Si and SiO_2 were ~10 nm/min and ~17 nm/min, respectively. Bragg reflectors were deposited on cleaned Si substrates held at 150 °C, by sequential deposition of SiO_2 and Si layers and without breaking vacuum. The Bragg reflectors exhibit good optical properties and moderately high compressive stress, as shown in Fig. 5.1.

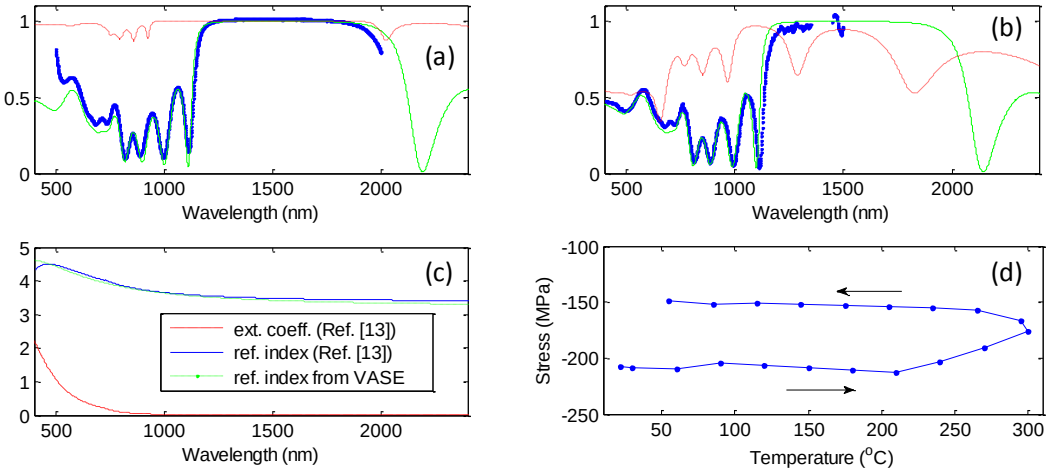

Figure 5.1 - Results for a 4-period Bragg reflector are shown. For the theoretical curves[iv], layer thicknesses of 102 nm and 260 nm were used for a-Si and SiO_2, respectively. (a) Reflectance at near normal incidence as measured with a spectrophotometer (blue symbols) and as modeled (green line). Modeled reflectance for TE polarized light at 88 degrees incidence angle is also shown (red dotted line). (b) Reflectance at 20 degrees incidence for TM polarization, as measured by a VASE instrument (blue symbols) and as modeled (green line). Modeled reflectance for TM polarized light at 88 degrees incidence angle is also shown (red dotted line). (c) Optical constants from Ref. [13] for a-Si, used in the modeling. Also shown is the index extracted from fitting to experimental data. (d) Net stress (MPa) of the multilayer measured at a series of increasing and then decreasing temperatures, after several days of storage in air. The stress measured soon after deposition was -235 MPa.

Reflectance was measured using both a spectrophotometer and a variable angle spectroscopic ellipsometry (VASE) instrument; typical results are shown in Figs. 5.1(a) and 5.1(b). In addition to 4-period Bragg multilayers, single-layer SiO_2 and

a-Si films were studied. SiO_2-like films with typical index ~1.47 in the near infrared were verified. For the a-Si films, optical constants were extracted from fitting experimental data. Both the refractive index (see Fig. 5.1(c)) and the extinction coefficient were in good agreement with the data for evaporated or sputtered a-Si layers reported in [13]. The theoretical curves shown in Figs. 5.1(a) and 5.1(b) were obtained using a standard transfer matrix model and the optical constants from [13]. The fit to experimental data is good, although the width of the experimental stop band is slightly less than predicted. This is likely due to a lower than expected index contrast (by ~0.1) in the multilayers, consistent with the lower index of the a-Si films grown here (n ~ 3.41 at 1550 nm, versus n ~ 3.5 reported in [13]). Inter-diffusion between Si and SiO_2 layers might also play a role in reducing the index contrast [12]. A more detailed study of the a-Si films (including the effects of hydrogenation) is ongoing.

Stress in both single films and multilayers was measured using a Flexus 2320 system, which has the capability of substrate heating. For multilayers, the effective-medium stress (~235 MPa compressive immediately after deposition) was well corroborated by measurements on single a-Si and SiO_2 layers, which revealed compressive stress ~420 MPa and ~160 MPa, respectively (note that the mirror is ~29% a-Si and ~71% SiO_2). Fig. 1(d) shows the stress variation versus temperature for a multilayer heated at a rate ~15 °C/min up to 300 °C, and then allowed to cool back to room temperature at a rate ~5 °C/min. The stress was fairly constant for moderate temperature increases, consistent with the similar thermal expansion coefficients expected for the a-Si and SiO_2 layers and the Si

substrate. However, heating above ~200 °C resulted in partial relaxation of the compressive stress. This implies that the morphology (peak height, etc.) of delamination buckles might depend to some extent on the temperature at which they form.

5.3.2 Development of Patterned Layer with Low Adhesion and Decomposability

The buckling self-assembly process relies on a patterned low-adhesion layer (LAL) to define the regions of delamination. As discussed in Chapter 4 the, LAL must have certain qualities: First, if the LAL is to remain on the inner surface of the hollow waveguide (i.e. as a surface layer on the upper or lower cladding mirror), it should be thin, have low roughness, and be optically transparent in the wavelength range of interest. Second, the LAL must be amenable to photolithographic patterning, either by etching or liftoff. Third, the patterned LAL must survive deposition of the upper Bragg mirror, subject to the deposition temperature that optimizes the stress, mechanical properties, and optical properties of the mirror. Because of their various properties, discussed in Sec 4.3, including low adhesion and binding energy, the thin fluorocarbon layers deposited using the passivation process in an inductively coupled plasma reactive ion etch (ICP-RIE) system (Surface Technologies Systems) [17] were employed here. Under suitable deposition conditions, these films exhibit low surface energy (water contact angle > 110 ° [18]), low coefficient of friction, low pinhole density [17], and good thermal stability [19].

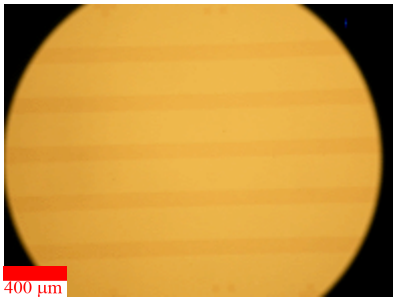

Figure 5.2 - A microscope image of a patterned fluorocarbon layer (~15 nm thick) is shown. Five strips, each 80 µm wide, are faintly visible. Alignment mark features (crosses and squares) are also visible, near the top and bottom of the image.

Films were deposited at a base pressure of 1 mTorr, RF power of 300 W, and using C_4F_8 as a source gas with flow rate of 60 sccm. The hydrophobic nature of the films was confirmed by observation of water contact angle. Films with thicknesses ~10 to 40 nm showed little variation in hydrophobic properties or amenability to patterning by liftoff.

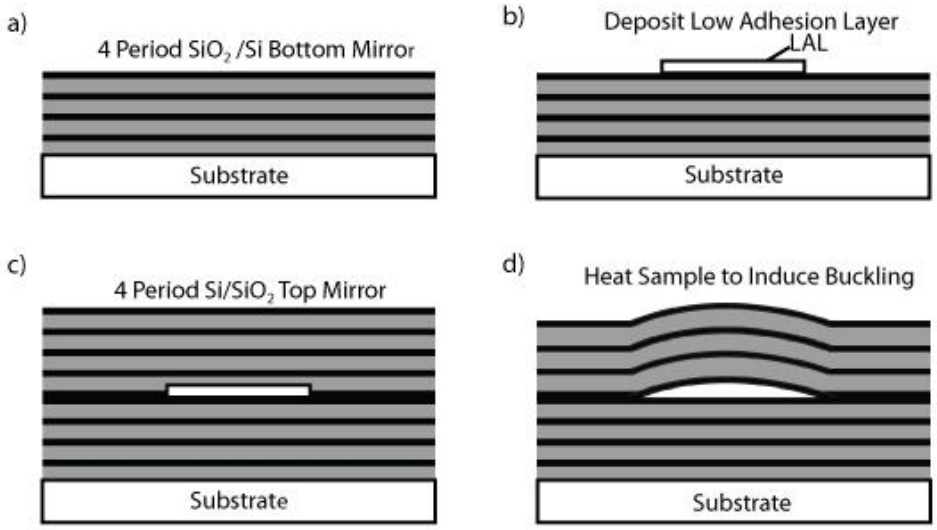

Figure 5.3 - Schematic showing the process steps used to fabricate hollow waveguides: (a) a 4-period Bragg reflector was deposited, (b) a fluorocarbon LAL layer was deposited and patterned by liftoff, (c) a second 4-period Bragg mirror (with net compressive stress) was deposited, and (d) the sample was heated to promote loss of adhesion in the regions of the LAL.

5.3.3 Review of the Buckling Self-Assembly Process

In the process described, controlled thin film buckling is exploited for the self-assembly of a three dimensional air core waveguide using otherwise planar (two-dimensional) processing steps. The process starts with a piranha cleaned silicon wafer, and follows the sequence of steps shown in Fig. 5.3.

First, a four-period Bragg reflector was deposited as the bottom cladding of the hollow waveguides. After photoresist patterning, a fluorocarbon LAL (typically 10 to 30 nm thick) was deposited as described in Section 2.2. The LAL was patterned by liftoff, thereby defining regions for subsequent delamination of the upper Bragg mirror. Next, the same sputtering system was used to deposit another four period Bragg reflector, which eventually acts as the upper cladding of the hollow waveguides.

Over large areas (2 cm x 1 cm) of patterned LAL, some spontaneous buckling of the upper mirror was observed immediately upon removal from the sputtering chamber (or within a few days). To induce buckling over the small LAL features, wafers were heated on a hotplate in an air or nitrogen atmosphere to ~200 °C. Heating in this range does not significantly affect the compressive stress of the films, as discussed in section 2.1. However, we speculate that the heating results in a partial decomposition of the fluorocarbon layer [19], further reducing the adhesion between the upper and lower mirror. It is also possible that the out-gassing of volatile C-F compounds exerts force on the upper mirror, providing additional driving energy for buckle formation. The precise mechanisms involved

are the subject of ongoing study; in any case, a high yield of straight-sided delamination buckles was realized. Microscope images of typical waveguides with 80 μm base width are shown in Figs. 5.4(a) and 5.4(b). An SEM image of the cleaved facet of a guide with 40 μm base width is shown in Fig. 5.4(c). The peak height of the delamination buckles (and thus the air cores) is dependent on the buckle base width [7],[8] and in the present case varied between ~1 and ~4 μm. Yield varied between samples, but was as high as ~80 % in some cases. Small defects were observed in most guides, as highlighted in Fig. 5.4(a), possibly associated with points where the Euler buckle joined after nucleating and propagating from opposite sides of the defect.

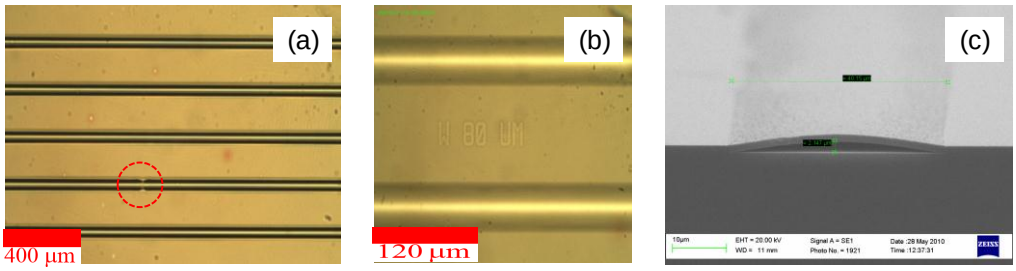

Figure 5.4 - Images of buckled waveguides are shown. (a) Microscope image of an array of five waveguides with 80 μm base width. The red circle indicates a typical defect in one of the guides. (b) Higher magnification image of two of the guides from part a. (c) SEM image of the cleaved facet of a waveguide with 40 μm base width.

The process might be viewed as a hybrid between two previously reported approaches for fabricating enclosed microchannels: the compressive stress of the upper mirror drives the formation of Euler buckles [7], and the fluorocarbon acts in part as a sacrificial decomposition layer [20]. However, the fluorocarbon layer is extremely thin in the present case, and we postulate that the morphology of the air-channel is determined primarily by the stress-driven buckling of the upper

mirror. To assess this, we used elastic buckling theory [8] and approximated the upper mirror as an effective-medium equivalent layer. For a-Si thin films, the Young's modulus has been reported to be ~100 GPa [21]. SiO_2 films have Young's modulus in the range ~40 to 70 GPa [22], with lower values typical for films grown at low temperature (as is the case here). Moreover, the modulus of a thin film is known to depend greatly on deposition parameters (including growth temperature), and can be lower than the corresponding bulk modulus by as much as 80% [21]. Using 70 GPa for SiO_2 results in an effective medium modulus Y ~80 GPa (as mentioned, the mirror is ~29% a-Si and ~71% SiO_2), which can be considered an upper bound for the multilayers described.

Fig. 5.5(a) shows an optical profilometer scan on a typical buckled waveguide. Line scans along the axis of the buckles produced estimates for RMS roughness as low as ~0.5 nm. Fig. 5.5(b) shows the peak buckle height versus base width as predicted by the elastic buckling theory using Y = 80 GPa or Y = 40 GPa, and an effective medium compressive stress of 235 MPa (see Sec. 2.1). Also shown are average measured buckle heights, revealing good agreement with the theoretical predictions obtained using the lower effective modulus. The experimental average was based on ~10 waveguides of each width on a particular sample, and the variation in peak height was ~0.1 μm in each case. Also consistent with the predictions of the elastic buckling theory, 10 and 20 μm wide LAL patterns on the same wafer did not buckle. Independent verification of the thin film elastic properties by other measurements would be desirable, but is left for future work.

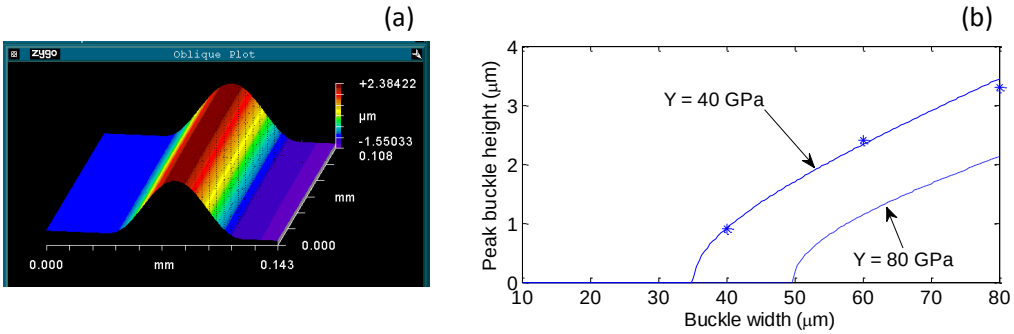

Figure 5.5 - (a) Topographical scan is shown for a waveguide with 80 µm base width and ~3.6 µm peak height, as obtained using an optical profilometer. (b) Predicted buckle height according to elastic theory given net compressive stress of 235 MPa and effective medium Young's modulus of Y = 40 GPa (solid line) or Y = 80 GPa (dashed line). The symbols show the mean values measured experimentally.

5.4 Optical Characterization

Samples were cleaved to facilitate light guiding experiments, and light from either a tunable laser (Santec) or a supercontinuum source (Koheras SuperK Red) was coupled via fiber-based polarization control optics and a tapered fiber (Oz Optics) with a nominal focal spot size of 6.5 µm. An objective lens was used to collect light from the output facet, for delivery to a photodetector, an optical spectrum analyzer (Anritsu), or an infrared camera. In some cases, the infrared camera was mounted on a microscope in order to capture images of light scattered from the top surface of the waveguides. Further details on the experimental setup can be found in [7],[8],[10],[11]. Waveguides with both 60 and 80 µm base width were studied, but the results presented below pertain to 60 µm guides with ~2.5 µm peak core height. The small peak core height for the 40 µm guides implies propagation near cutoff [10], and in that case very high propagation loss was verified experimentally.

Owing to the low reflectance of the cladding mirrors for TM polarized light at high incidence angles (see Fig. 5.1), all of the waveguides exhibit high loss for TM polarized light. On the other hand, due to their low height-to-width aspect ratio, the waveguides support multiple TE (in-plane) polarized modes [7],[10]. Fig. 5.6(a) shows the four lowest-order TE modes at a wavelength of 1560 nm, selectively excited by adjusting the position of the tapered fiber relative to the input facet of a waveguide.

Fig. 5.6(b) shows a top view of a waveguide, ~0.6 cm in length, excited by the supercontinuum source. The input and output facets are visible as the bright scattering points at the left and right, respectively. Similar images captured using the tunable laser source produced only faintly-visible light streaks, apparently due to low radiation and scattering of light from the top surface of the waveguides. Nevertheless, images were sufficiently bright to enable a loss estimation from the decay of the scattered light streak. Fig. 5.6(c) shows the result of one such measurement, for a waveguide with base width of 60 μm and peak height ~2.5 μm, producing a loss estimate of 5.1 dB/cm. This is slightly higher than the loss reported for a-Si/SiO_2-based hollow waveguides in [6], although those devices employed 6-period cladding mirrors. Overall insertion loss was as low as ~10 to 12 dB, with a significant portion attributable to input coupling loss between the tapered fiber and the hollow waveguide.

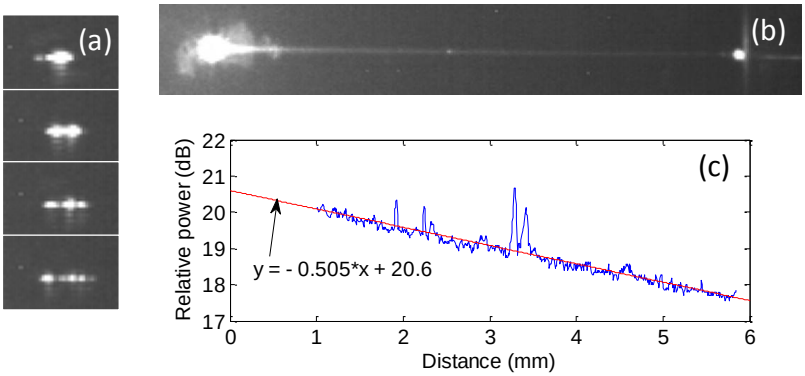

Figure 5.6 - TE light guiding results are shown for a waveguide with 60 μm base width and peak height ~2.5 μm. (a) Waveguide end facet images captured by an infrared camera via a 60x objective lens, for varying input coupling conditions of a 1560 nm laser source. (b) Scattered light image captured by an infrared camera for a waveguide ~6 mm in length, with supercontinuum light coupled at left. The bright spot at right is the output facet. (c) Relative power captured by the infrared camera versus distance along the waveguide axis, for an input wavelength of 1560 nm. The red line is a linear fit to the data.

A key signature of a photonic band bap guidance mechanism is the wavelength dependence of the optical transmission. To predict the low-loss guidance band of the waveguides, we used a transfer-matrix-based slab waveguide model described in detail elsewhere [10],[11],[23]. Propagation loss versus wavelength was calculated for the fundamental TE mode of a symmetric, air-core slab waveguide, clad by mirrors with the parameters specified in Fig. 1. The slab model is reasonably valid for the buckled waveguides, due to their small height-to-width aspect ratio and tapered lateral profile [7]. Moreover, the low-loss modes all exhibit a single lobe in the vertical direction (see Fig.5. 6(a)) and are well-approximated by the fundamental mode from the slab model.

In the model, the a-Si layers were assigned the refractive index data shown in Fig. 5.1(c), and were treated either as lossless or as having the extinction coefficient data taken from [13] and shown in Fig. 5.1(c). The results of the simulations are shown in Fig. 5.7(a). For lossless layers, a transmission band in the 1000-1600

nm range with loss ~1 dB/cm is predicted. With the silicon loss included, minimum propagation loss ~7 dB/cm is predicted and the transmission band is narrowed. Given the experimental loss estimate from Fig. 5.6(c), it is possible that the extinction coefficient of our a-Si layers is somewhat lower than that reported in [13]. This might indicate the presence of oxygen in the layers, consistent with their lower refractive index discussed in Sec. 2. As mentioned, a more detailed study of the optical constants of these films is the subject of ongoing work.

Experimentally, the wavelength-dependent transmission was measured using the supercontinuum source and the OSA. Fig. 5.7(b) shows raw transmission spectra for two waveguides with peak core height ~2.5 μm, but from two different samples with slightly different mirror parameters. A broad transmission band between ~1100 nm ~1700 nm was observed, in reasonable agreement with the theoretical prediction. As discussed elsewhere [8], waveguide measurements with a supercontinuum source are complicated by spectral variation in coupling efficiency, especially if the waveguide supports multiple low-loss modes. Most of the random variations and dips in the transmission band can be attributed to these factors. However, each waveguide tested exhibited a deep and relatively sharp dip in transmission near ~1350 nm. The exact spectral location of this dip varied between samples (with slightly different cladding mirrors) and between waveguides (with different air-core size) on a given sample. This implies that the dip is due to a geometrically-dependent resonant effect, as opposed to a material absorption resonance. We postulate that it arises from the interaction of in-plane

polarized light with the 'sidewalls' of the upper, buckled cladding mirror. As shown in Fig. 5.1(b), the mirrors exhibit a notch in reflectance at a similar wavelength, for TM-polarized light at high incidence angles. This effect has been discussed previously [7], and can be mitigated by tailoring the thickness of the first a-Si layer in the upper mirror [1],[3],[4] or by metal termination of the upper mirror [8]. We hope to explore such improvements in future work.

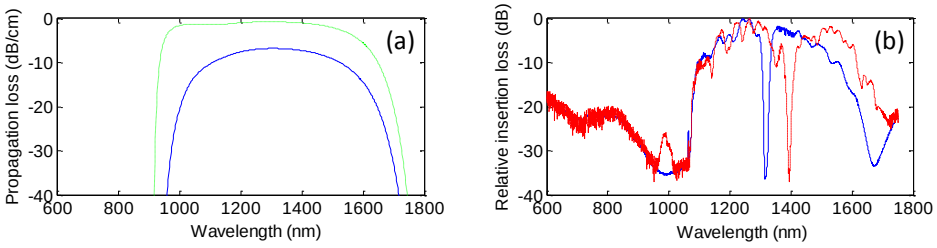

Figure 5.7 - (a) Predicted propagation loss for the fundamental TE mode of a slab Bragg waveguide with 4-period mirrors and air-core height 2.5 μm, assuming lossless Si layers (green dotted curve) or with Si loss included (blue solid curve). (b) Experimentally measured transmission spectrum for two waveguide samples, each with peak core height ~2.5 μm. The apparent transmission below ~900 nm is an artifact arising from aliasing in the diffraction-grating based OSA.

Finally, it is worth mentioning that polarization control of the input light had little effect on the shape of the transmission spectrum. This is consistent with the extremely high polarization dependent loss of the waveguides; we verified that only TE-polarized light is present at the output facet.

5.5 Conclusions

A MEMS-compatible process for fabricating silicon-based, air-core waveguides was described. To date, the yield of the process (in terms of percentage of LAL strip areas that buckle without defects) has typically been in the 50 to 80 % range. We believe that the main factor limiting the yield is the uniformity of the

fluorocarbon LAL. Efforts to improve this uniformity, by varying the deposition and annealing conditions, are under study. Nevertheless, arrays of low-defect waveguides with length ~1 cm have already been realized. The waveguides exhibited loss as low as ~5 dB/cm (in the 1550 nm wavelength region), partly attributable to absorption by a-Si layers in the cladding mirrors. The loss is comparable to that of other air-core integrated waveguides reported in the literature, and might be reduced further by the use of hydrogenated a-Si.

We believe the waveguides described are a promising alternative to conventional air-core waveguides fabricated by wafer bonding or sacrificial etching techniques. The self-assembled nature of the waveguides results in smooth sidewall interfaces, which is beneficial for guiding light and might also benefit the efficient flow of fluids through the air channel. Moreover, complex geometries including bends and tapers [7] can be fabricated in parallel. Because of these attributes, and given their silicon-based processing, the waveguides might find application in optofluidic and lab-on-chip analysis systems [1].

5.6 Works Cited

[1] H. Schmidt, Dongliang Yin, J. Barber, and A. Hawkins, "Hollow-core waveguides and 2-D waveguide arrays for integrated optics of gases and liquids," *Selected Topics in Quantum Electronics, IEEE Journal of*, vol. 11, 2005, pp. 519-527.

[2] Y. Zhou, V. Karagodsky, B. Pesala, F.G. Sedgwick, and C.J. Chang-Hasnain, "A novel ultra-low loss hollow-core waveguide using subwavelength high-contrast gratings," *Optics Express*, vol. 17, Feb. 2009, pp. 1508-1517.

[3] T.C. Shen, Y.S. Kim, J.A. Bur, and S. Lin, "Optical Characterization of Bending Efficiency in On-Chip Hollow-Core Bragg Waveguides at 1500 nm," *Journal of Lightwave Technology*, vol. 28, Jun. 2010, pp. 1714-1719.

[4] M. Kumar, T. Sakaguchi, and F. Koyama, "Wide tunability and ultralarge

birefringence with 3D hollow waveguide Bragg reflector," *Optics Letters*, vol. 34, Apr. 2009, pp. 1252-1254.
[5] E. Epp, N. Ponnampalam, J.N. McMullin, and R.G. DeCorby, "Thermal tuning of hollow waveguides fabricated by controlled thin-film buckling," *Optics Express*, vol. 17, 2009, pp. 17369-17375.
[6] S. Lo, M. Wang, and C. Chen, "Semiconductor hollow optical waveguides formed by omni-directional reflectors," *Optics Express*, vol. 12, Dec. 2004, pp. 6589-6593.
[7] R.G. DeCorby, N. Ponnampalam, H.T. Nguyen, M.M. Pai, and T.J. Clement, "Guided self-assembly of integrated hollow Bragg waveguides," *Optics Express*, vol. 15, Apr. 2007, pp. 3902-3915.
[8] N. Ponnampalam and R.G. Decorby, "Self-assembled hollow waveguides with hybrid metal-dielectric Bragg claddings," *Optics Express*, vol. 15, 2007, p. 12595.
[9] M.-. Moon, K.-. Lee, K.H. Oh, and J.W. Hutchinson, "Buckle delamination on patterned substrates," *Acta Materialia*, vol. 52, Jun. 2004, pp. 3151-3159.
[10] N. Ponnampalam and R.G. DeCorby, "Out-of-plane coupling at mode cutoff in tapered hollow waveguides with omnidirectional reflector claddings," *Optics Express*, vol. 16, Mar. 2008, pp. 2894-2908.
[11] R. DeCorby, N. Ponnampalam, E. Epp, T. Allen, and J. McMullin, "Chip-scale spectrometry based on tapered hollow Bragg waveguides," *Optics Express*, vol. 17, 2009, pp. 16632-16645.
[12] B. Gallas, S. Fisson, E. Charron, A. Brunet-Bruneau, G. Vuye, and J. Rivory, "Making an Omnidirectional Reflector," *Applied Optics*, vol. 40, Oct. 2001, pp. 5056-5063.
[13] E.J. Prucha and E.D. Palik, *Handbook of optical constants of solids, volumes I, II, and III: subject index and contributor index*, Academic Press, 1998.
[14] Q. Song, F. Huang, M. Li, B. Xie, H. Wang, Y. Jiang, and Y. Song, "Graded refractive-index SiO[sub x] infrared filters prepared by reactive magnetron sputtering," *Journal of Vacuum Science & Technology A: Vacuum, Surfaces, and Films*, vol. 26, 2008, p. 265.
[15] H. Lee, H. Makino, T. Yao, and A. Tanaka, "Si-based omnidirectional reflector and transmission filter optimized at a wavelength of 1.55 μm," *Applied Physics Letters*, vol. 81, 2002, p. 4502.
[16] H. Yoda, K. Shiraishi, Y. Hiratani, and O. Hanaizumi, "a-Si:H/SiO2 Multilayer Films Fabricated by Radio-Frequency Magnetron Sputtering for Optical Filters," *Applied Optics*, vol. 43, Jun. 2004, pp. 3548-3554.
[17] A. Ayon, D. Chen, and R. Khanna, "A Novel Integrated MEMS Process Using Fluorocarbon Films Deposited With a Deep Reactive Ion Etching (DRIE) Tool," *Materials Research Society Symposia Proceedings*, vol. 605, 2000, pp. 141-147.
[18] J. Han, J. Yeom, G. Mensing, D. Joe, R.I. Masel, and M.A. Shannon, "Surface energy approach and AFM verification of the (CF) treated surface effect and its correlation with adhesion reduction in microvalves," *Journal of Micromechanics and Microengineering*, vol. 19,

2009, p. 085017.
[19] Y.X. Zhuang and A. Menon, "Wettability and thermal stability of fluorocarbon films deposited by deep reactive ion etching," *Journal of Vacuum Science & Technology A: Vacuum, Surfaces, and Films*, vol. 23, May. 2005, pp. 434-439.
[20] P.J. Joseph, H.A. Kelleher, S.A.B. Allen, and P.A. Kohl, "Improved fabrication of micro air-channels by incorporation of a structural barrier," *Journal of Micromechanics and Microengineering*, vol. 15, 2005, pp. 35-42.
[21] M.M. de Lima, R.G. Lacerda, J. Vilcarromero, and F.C. Marques, "Coefficient of thermal expansion and elastic modulus of thin films," *Journal of Applied Physics*, vol. 86, 1999, p. 4936.
[22] W.D. Nix, "Mechanical properties of thin films," *Metallurgical and Materials Transactions A*, vol. 20, Nov. 1989.
[23] P.K. Dasgupta, Z. Genfa, J. Li, C.B. Boring, S. Jambunathan, and R. Al-Horr, "Luminescence Detection with a Liquid Core Waveguide," *Analytical Chemistry*, vol. 71, Apr. 1999, pp. 1400-1407.

Chapter 6 Conclusion

6.1 Summary of Results

The goal of this M.Sc. project was to develop new photonics devices based on hollow waveguides fabricated using a self-assembly process. Traditional total-internal-reflection-based waveguides are restricted to a limited subset of mainly solid materials, since the core must have a higher index then the cladding. Obviously, this requirement precludes air as a core material because of its near unity index, and the same restriction applies to most gases and many liquids. Hollow-core Bragg waveguides do not have these restrictions, and are well-suited for incorporation into MEMS and MOEMS type devices. The relatively new field of optofluidics provides numerous potential applications for hollow Bragg waveguides, because of their potential to support propagation in a liquid core.

6.1.1 Thermal Tuning of First-Generation Hollow Waveguides

Initial results were achieved with waveguides based on a previously developed fabrication method involving silver dissolution into chalcogenide glass (see Sec. 3.1). This process produced hollow Bragg waveguides with multilayer claddings of polymer and glass. In earlier work, vertical outcoupling of light at mode cutoff in tapers had been demonstrated [1]. Here, it was shown that the air-core dimensions of these waveguides could be thermally tuned. Such variation in air

core dimensions provides a repeatable method to alter the loss and propagation constants of the guided modes. It was shown that the out-coupling locations of specific modes along a tapered waveguide could be controlled by varying the temperature. Significant results obtained from the experiments on tapered waveguides in Chapter 3 include:

- Proof of concept for a new type of tunable, waveguide coupled Fabry-Perot filter;
- Verification of predictable changes in waveguide core height with temperature;

6.1.2 Development of Silicon-based Hollow Waveguides by Buckling Self-assembly

The bulk of the work for this thesis was aimed at developing a fabrication method for silicon-based self-assembled hollow waveguides. This was an extension of the previous work mentioned above, and the goal was the formation of waveguides using a similar buckling principle. Early in the project, it was decided that the claddings of the waveguides would be an a-Si/SiO_2 Bragg reflector. However, this introduced unique challenges related to controlling stress and adhesion of silicon and SiO_2 layers. The layers were sputtered to ensure the largest degree of control over stress, and a patterned fluorocarbon layer was ultimately decided upon as the most suitable LAL. Amongst other attributes, the fluorocarbon LAL is optically transparent in the wavelength range of interest. The waveguides were heated to

promote loss of adhesion on the fluorocarbon patterns and thus to induce buckling.

Empirical studies were conducted to partially optimize this heating process. Key results from the development of the silicon-based waveguides include:

- Successful development of novel process for fabricating hollow waveguides by controlled buckling of a-Si/SiO_2 multilayers;
- Optimization of the aforementioned process, such that air core waveguides were produced with a reasonably high yield;
- Verification of optical transmission in the 1550 nm wavelength region, with loss as low as ~ 5 dB/cm;

6.2 Future Work

The optimization of the waveguide fabrication process will be a significant focus of future research in the DeCorby lab. Increasing the waveguide yield would reduce the amount of required processing per waveguide and increase the chances of developing a commercial device. Several approaches are being used to reduce defects in the buckling process. Different materials are being studied as an overlayer to reduce cracking during buckle formation and handling. Ideally the coating would not affect the compressive stress and would be transparent in the wavelength region of interest. The polymer Parylene, which was also studied as a possible LAL, has shown some early promise as a protective overlayer, but more study is needed to verify its effectiveness. Optimization of the properties of the

fluorocarbon LAL, including its uniformity, adhesion, and hydrophobicity, is another area of continued research. Defects in this layer are thought to significantly reduce the chance of forming a higher yield of defect free waveguides.

6.2.1 Increasing Operating Range

Although silicon has excellent optical properties in the near-IR range, its absorption for wavelengths near the visible range is a disadvantage. The incorporation of hydrogen into the silicon layers has been shown to significantly reduce their loss in the ~800 to 1000 nm range [2]. Typically, the a-Si films are hydrogenated during deposition. In the case of sputtering, H_2 gas can be added during the a-Si deposition producing a film with a significantly lower extinction coefficient [2]. Another option currently under investigation involves a post-deposition annealing at elevated temperatures in a hydrogen rich atmosphere. Each of these options has the potential to create waveguides with much lower loss in the 800 - 1000 nm range, extending their applicability to Lab-on-Chip systems.

6.2.2 Microspectrometer Design using Silicon-based Waveguides

Optical spectrometers are commonly utilized in the selective measurements of the composition of liquids and gases. For example, an IR absorption spectrum can be used to determine the composition of a gas [3] or fluid sample [4]; in the latter case this is referred to as chemical chromatography. Fluorescence techniques are used in chemistry to detect the presence of dissolved ions or molecules in a

system [5]. Conventional spectrometers are mostly bench-top instruments for the laboratory and can be prohibitively expensive.

The DeCorby research group has shown that tapered hollow waveguides with omnidirectional Bragg claddings can form the basis of a microspectrometer. As light propagates down such a vertically tapered waveguide, it reaches a mode cutoff point at which it couples vertically out of the waveguide. The location of this outcoupling spot is wavelength dependent and therefore, measuring the position allows wavelength to be extrapolated. This principle was experimentally verified using a self-assembled tapered Bragg waveguide, based on chalcogenide glass and polymer [6]. In future work, it would be interesting to implement these spectrometers using the silicon-based waveguides developed here. This would result in more options for practical implementation of the spectrometer since many microfluidic and lab-on-chip systems employ silicon based processes.

6.3 Works Cited

[1] N. Ponnampalam and R.G. DeCorby, "Out-of-plane coupling at mode cutoff in tapered hollow waveguides with omnidirectional reflector claddings," *Optics Express*, vol. 16, Mar. 2008, pp. 2894-2908.

[2] H. Yoda, K. Shiraishi, Y. Hiratani, and O. Hanaizumi, "a-Si:H/SiO2 Multilayer Films Fabricated by Radio-Frequency Magnetron Sputtering for Optical Filters," *Applied Optics*, vol. 43, Jun. 2004, pp. 3548-3554.

[3] Stuart, B, *Modern IR spectroscopy*, New York: Wiley, .

[4] V.P. Iordanov, G.W. Lubking, R. Ishihara, R.F. Wolffenbuttel, P.M. Sarro, and M.J. Vellekoop, "Silicon thin-film UV filter for NADH fluorescence analysis," *Sensors and Actuators A: Physical*, vol. 97-98, Apr. 2002, pp. 161-166.

[5] D. Rossberg, "Silicon micromachined infrared sensor with tunable wavelength selectivity for application in infrared spectroscopy," *Sensors and Actuators A: Physical*, vol. 47, 1995, pp. 413-416.

[6] N. Ponnampalam and R.G. DeCorby, "Out-of-plane coupling at mode cutoff in tapered hollow waveguides with omnidirectional reflector claddings,"

Optics Express, vol. 16, Mar. 2008, pp. 2894-2908.

Endnotes

[i] This VASE modeling done by summer student Ward Newmann.

[ii] TEM images captured and prepared by Shalon McFarlane.

[iii] MatLab modeling done by Dr. Ray DeCorby.

[iv] Theoretical modeling done by Dr. Ray DeCorby.